Final Project Report 10/2017 - 9/2021 – Award No. DE-FE0031228

Final Project Report:

Fuel injection dynamics and composition effects on RDE performance

Principal Investigator:

Mirko Gamba and Venkat Raman

Department of Aerospace Engineering
University of Michigan

Contents

Chapter 1

Objectives and Motivation

The project involved collaboration between UM faculty (Gamba, Raman) and industry partners. The project focused on fundamental research that supports industry needs on understanding and quantifying the effects of detonation-induced injector dynamics of low-loss configurations and multi-component fuels (MCFs) on mixing, stratification, detonation structure and propagation. The worked identified and provided critical understanding of operability and performance of practical RDEs.

The specific objectives of the research were:

- **Objective 1:** Develop a comprehensive understanding of injector dynamics, coupling with diffuser back-reflections, and their impact on RDE mixing, operation and performance.
- **Objective 2:** Develop a comprehensive understanding of multi-component fuels (syngas and hydrocarbon blends) on RDE detonation structure and propagation, operation and performance.
- **Objective 3:** Develop advanced diagnostics and predictive computational models for studying detonation propagation in RDEs, with arbitrary fuel composition and flow configuration.

The work was organized in a combined experimental and computational effort to develop the program meeting the three objectives idenfitied here.

Chapter 2

Experimental activities

2.1 Overview

The work presented in this work is the result of several studies performed on two RDC geometries. Both of the geometries are the standard 6in diameter round configurations with axial air inlet and transverse fuel injection. The first of these designs was developed and tested for the previous grant. The difference between the two will be detailed later; however, one of the primary differences is the contouring of the axial air inlet and the ability to easily change the inlet area in the second, enhanced design. The operation and general characteristics of this new, second design will be reported.

2.2 Experimental RDC Facility

The basic experimental facility was devloped under a previous grant, and a detailed explanation of it can be found under the report for that grant. Reported here are the modifications and improvements that were made to the facility that enabled the various experiments performed under this grant.

2.2.1 Standard Axial Air Inlet (AAI)

The standard RDC is based around our modular design reported for the previous grant. Specifically here, we focus on the axial air inlet (AAI-1), the details of which are repeated here briefly for the sake of clarity. The flow field consists of air flowing axially over a smooth one-sided contoured surface. This protruding surface results in an annular air slot of 1.6mm (0.063in) width. With the standard 7.6mm (0.3in) channel gap, this creates a channel area to inlet area ratio of 4.6 (AR = $A_{3.2}/A_{3.1,a}$). Fuel is injected from an inner plenum into the detonation channel from the upper face of the contour from 120 evenly spaced individual jets with a diameter of 0.89mm (0.035in). This is schematically shown in Figure 2.1. The air plenum is nominally 50.8mm (2in) long with a channel length of about

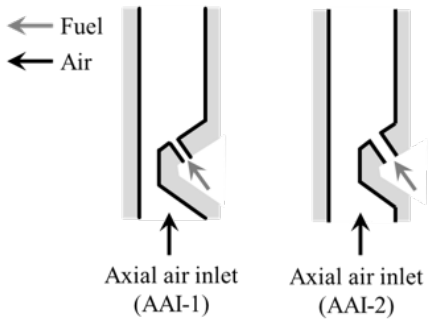

Figure 2.1: Diagram of axial air inlet with transverse fuel injection designs, AAI-1 and AAI-2.

106mm (4.17in) from the fuel injectors. This configuration has been studied extensively. [1, 2, 3, 4].

Additionally, for the purpose of studying inlet area effects, a second variation of this design has been studied [5]. We refer to this design as AAI-2, and this is also shown in Figure 2.1. The two configurations (AAI-1 and AAI-2) are geometrically similar and the channel and plenum geometries remain unchanged. The two configurations differ for the detonation channel to inlet throat area ratio (AR), but maintain a similar value of the inlet throat area to fuel injection area ratio, $(A_{3.1,a}/A_{3.1,f})$, in an attempt to maintain the fuel-to-air momentum flux ratio the same between the two configurations. This results in an AR of 2.5. The increased fuel throat area is achieved by having 120 evenly spaced individual jets with a diameter of 1.32mm (0.052in).

2.2.2 Enhanced Axial Air Inlet (EAAI)

We also consider a new RDC inlet design with a variable area axial air inlet that allows for the air inlet (throat) area to be changed while maintaining aerodynamic similarity across different inlet area ratio configurations and without modifying the downstream detonation channel configuration. This is schematically shown in Figure 2.2. The inlet area ratios (ARs) tested were 3, 4, and 5, which represent the ratio of channel area to air inlet area. This axial inlet also allows for a continuous and direct connection between the channel and plenum to permit analysis of their coupling during operation. The fuel is again injected from an inner plenum outwards radially into the detonation channel from the upper surface of the contour from 120 evenly spaced individual jets. However, unlike the standard AAI, the fuel injectors are larger in diameter, thereby increasing the fuel injection area. The air plenum is also lengthened compared to the standard AAI configuration, increasing to about 141mm (5.55in) which better allows for studying the upstream properties as influenced by the detonation wave. High-speed pressure (HSP) measurements are taken within the plenum and low-speed static pressures through the use of CTAPS are taken in the plenum and along the air inlet. The detonation channel length was increased slightly to 115mm (4.53in).

2.2.3 Pre-Detonator for Ignition

Previously the ignition of the combustor was initiated solely by flame flashback from the downstream afterburner attached to the exhaust system, since the afterburner was neccessary to ensure complete combustion occurs prior to the exhaust system. However, a pre-detonator was implemented into the system in conjunction with the afterburner to aid in ignition for geometric configurations that made flame flashback more difficult. The pre-detonator utilized a H_2/O_2 mixture that fired with a frequency of 7 Hz. The detonation from the pre-detonator was then injected radially into the channel 12.7 mm downstream from the injectors. The afterburner was still maintained throughout the course of the run for safety purposes, and at this time we cannot decisively say whether the pre-detonator or the afterburner was the primary source of ignition. Therefore, for now, being able to achieve detonative operation is determined solely by the fuel/oxidizer mixture independent of the ignition mechanism (either flame flashback or injecting a detonation).

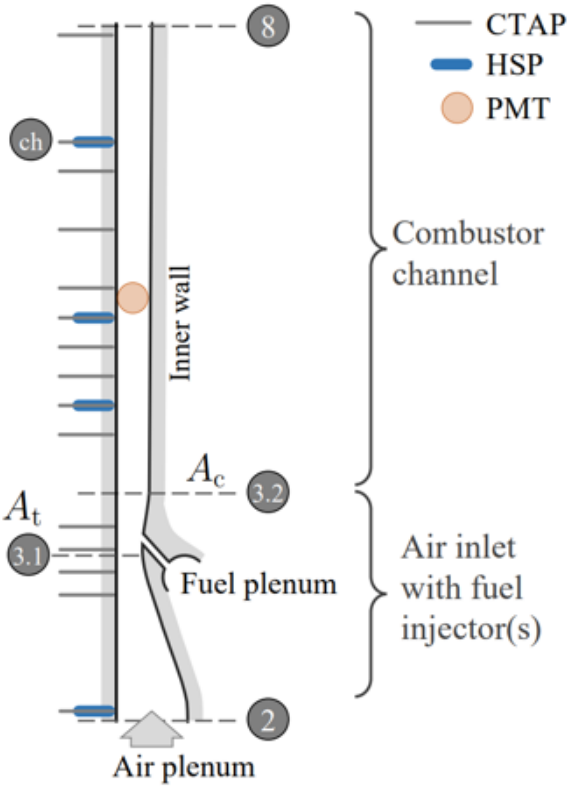

Figure 2.2: Diagram of enhanced axial air inlet configuration with transverse fuel injection.

2.2.4 Instrumentation

High-speed pressure measurements, aft high-speed chemiluminescent video, and low-speed static pressure measurements via continuous tube attenuated pressure (CTAPs) in the channel are applied to investigate the operation of the system similar to our previous work [6, 3]. The standard arrangement of sensors for the tests performed with the EAAI is shown in Figure 2.3 in which the dotted lines are the injection plane and exit plane of the combustor. The high-speed pressure measurements in the detonation

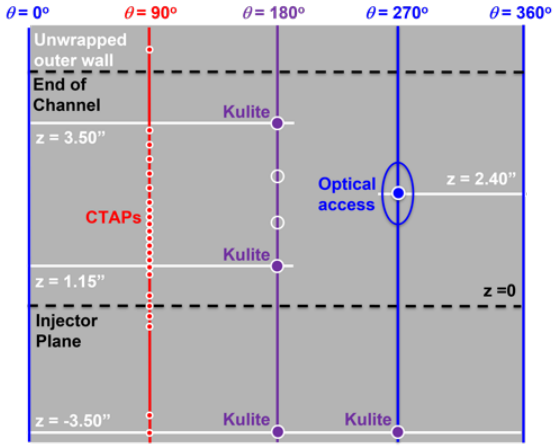

Figure 2.3: Unwrapped outer body showing different sensor positions relative to injector plane. High-speed pressure measurements (Kulites) are in purple, low-speed pressure measurements (CTAPs) are in red, and optical access is in blue.

channel (EWCTV-312 Kulites) are aligned azimuthally but are spaced apart axially by 60 mm (2.35"). To study the dynamics of the extended plenum, two high-speed pressure measurements (XTEL-190 Kulites) were added to the plenum. These were at the same axial location but clocked 90° apart to distinguish between rotating and pulsing waves. These measurements are taken about 89 mm (3.5") from the injectors. In addition to the high-speed measurements, CTAPs along the detonation channel, air inlet throat, and into the extended plenum were utilized. During some testing, a high-speed pressure measurement (XTEL-190 Kulites) was taken in the throat at the same axial position of one of the CTAPs; however, after a few runs, it was found that the sensor was destroyed, and was subsequently removed for the remaining tests. Overall, having this arrangement of sensors allows for determining rotations in the plenum as well as longitudinal pulsing in the entire system by looking at the relative time histories measured by the various sensors. Since all of the channel measurements are part of the outer body piece which is shared between the standard AAI and enhanced AAI, the 16 CTAPs, optical access, and 4 Kulites present in the channel are used when testing the standard AAI.

2.2.5 Thrust Measurement

We have previously demonstrated the ability to take thrust measurements from the RDC when in the AAI configuration [7]. This was accomplished through the development and use of a standalone thrust stand that allows axial translation of the RDC while coupled to the facility exhaust system. Net thrust values are found by accounting for all axial force components and applying corrections for the pressures observed on the bluff body exhaust and RDC to facility flange. The thrust stand was designed for the AAI injector configuration, and due to variations in plenum geometry and routing of reactant feed-lines was incapable of taking thrust measurements in the EAAI inlet configuration as originally configured. The single load-cell used for thrust takeout on the AAI configuration performed thrust takeout in tension upstream of the RDC. The extended plenum and center-line oxidizer feed-line of the EAAI configuration prevented use of this thrust takeout methodology.

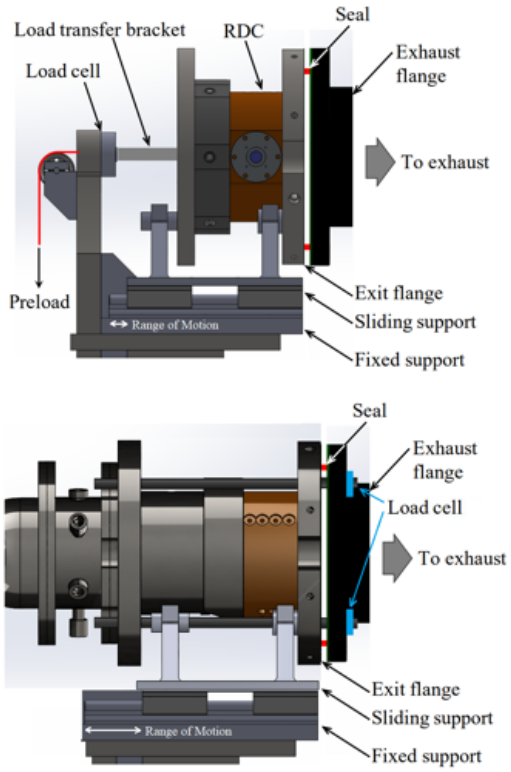

Figure 2.4: Diagram of the assembled thrust stand integrated with AAI RDC (top) and with improvements made to accommodate EAAI RDC (bottom). Air/fuel feed lines and accessories not shown for clarity.

Several improvements have been made to the thrust stand and associated hardware since the original test campaigns focused on capturing thrust measurements in the AAI configuration. Modifications to the existing thrust stand were made to accommodate testing with the EAAI RDC geometry by extending the range of motion of the trolley upon which the RDC is secured, and designing adapter pieces that allow for the incorporation of a dual load-cell system in a tension thrust takeout configuration that reacts against the secured facility exhaust system. Preliminary tests in this configuration have been conducted as a proof of concept, and additional tests utilizing this thrust takeout methodology will be conducted in the future.

Additional improvements were made in the methodologies used for correction from measured thrust to an effective net or stream thrust. The first test sequence conducted with the thrust stand (summarized in [7]) utilized a total of six pressure measurements on the bluff body exhaust cap on the RDC inner body, a single pressure measurement on the RDC exhaust flange to facility exhaust flange interface, and included axial fuel introduction to the RDC control volume which required an accounting for of the momentum introduced to the control volume. The exhaust cap has since been modified to include a total of seventeen pressure measurements. Additional improvements have been made on the RDC exhaust flange to facility exhaust flange interface, where the prior single pressure correction has been expanded to eight measurements at two azimuthal locations and four radial locations. These improvements can be seen in Figure 2.5, which illustrates the pressure measurement locations used in the calculation of net thrust in the original (top) and improved (bottom) configurations. The fuel feed-line routing has also been modified such that fuel is introduced orthogonal to the thrust vector, eliminating the axial momentum contribution correction that was previously required.

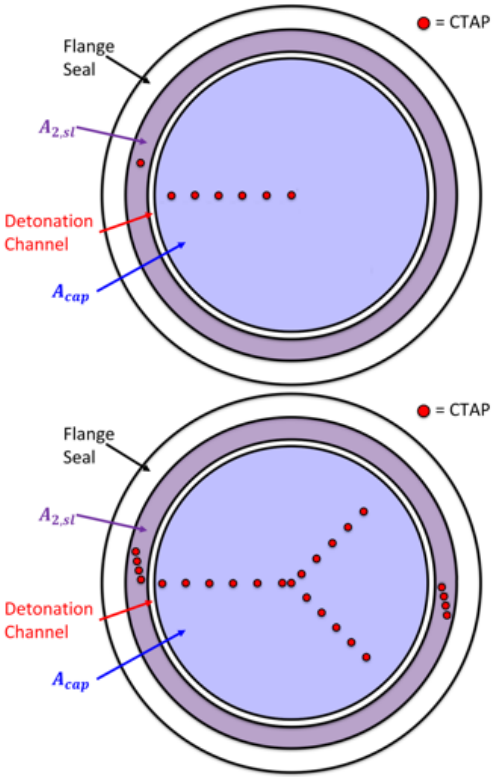

Figure 2.5: Measurement locations for pressure corrections used during initial testing (top) and subsequent improvement (bottom).

2.2.6 Pebble Bed Preheater

An electrically heated in-line pebble-bed system has been developed and integrated into the RDC system to provide heated air to the RDC. Simplified schematics showing the flowpaths during the heating and operation are shown in Figure 2.6(a). The pebble-bed heater is composed of a pressure vessel that contains five thousand 1.25 cm diameter steel balls that are used as a large heat reservoir. The size of the

balls was chosen to balance the pressure drop across the pebble-bed and the amount of heat scavenged by the air. A secondary inlet and exit with a high-temperature valving system allows for heated air from a 4.5 kW air electrical heater to heat the balls before the test. These additional ports are closed prior to airflow to seal off the pebble-bed heater. The temperature profile within the pebble-bed was continually monitored and logged with three type K thermocouples inserted radially at different axial locations.

The system was designed to heat the incoming air up to 800 K and sized to support a 15 second test for air mass flows of up to 1 kg/s. The pebble bed has thus far been tested up to a mean temperature of 600 K, although the achieved maximum T_2 entering the RDC is 500 K for a non-reacting condition and 480 K for a reacting condition. Lower RDC inlet temperatures than those measured in the bed are likely due to heat losses in the air transmission line. These inlet air temperatures are representative of the post-compressor temperature in a low overall pressure ratio engine (such as a T63 engine [8]). Additional improvements on the heater, airlines, and heating sequence to be made in the future are expected to minimize thermal losses, raise the effective inlet temperature closer to design conditions, and extend the range of available temperatures. It was also observed that T_2 would increase for the first several seconds of air flow. To reach a quasi-steady state temperature across the 2 second test fire, the air flow was allowed to flow through the system 10 seconds prior to ignition to better reach a nearly steady inlet air temperature.

A sample temperature trace across the entire test is shown in Figure 2.6(b), where is the time is relative to the fuel injection. The vertical, dashed red-lines mark the region when the fuel is on in the system. The thermocouple was not amplified or filtered during the measurement, and exhibited significant noise in the raw voltages measured by the DAC. For the particular case shown in Figure 2.6(b), previous testing/heating caused the elevated starting temperature of about 340 K. Typically after the first heated run, subsequent runs have slightly higher starting temperatures due to lower heat loss to the heated walls. As air flow is established, the temperature ramps up as additional heat is scavenged from the pebble-bed. Despite the noise, it can be seen that by the dashed red lines, the signal levels off and varies around a nearly constant value. This “constant” value is taken as the steady state temperature for the duration of the fuel-on sequence.

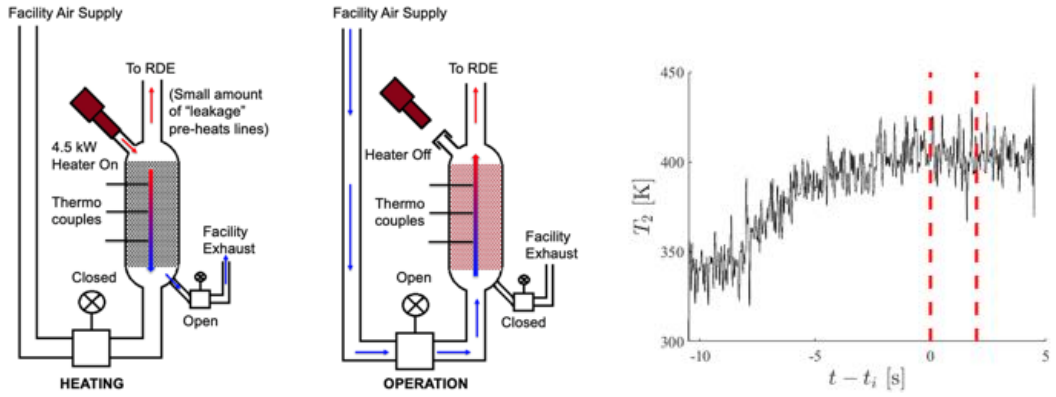

(a) (b)

Figure 2.6: a) Schematic diagram of in-line pebble-bed heater. (Left) Heating of the pebble-bed is provided by an electrical heater. (Right) During operation air is heated flowing through the steel balls bed.
b) Inlet temperature profile of a test. Vertical, dashed, red lines denote when fuel is on. Quasi-steady is achieved despite noise.

2.2.7 Injecting CO_2 into RDC

One of the experiments conducted was to introduce CO_2 into the RDC during H_2/air operation to examine the impact of a diluent on the detonation as well as to enable an Up-Conversion Imaging (UCI) measurement technique. Since in our system, the fuel and air are independently injected into the system allowing for control over the global equivalence ratio entering into the system, CO_2 will be added to both air and fuel stream to achieve a constant volume fraction of CO_2 everywhere in the flow. The CO_2 is controlled and metered through choked orifices in a similar fashion to the fuel. Throughout this work, when discussing the amount of CO_2 in the system, we will be using the mole fraction of CO_2 with respect to all the gases (air, diluent, and fuel) introduced into the system. This was done to mitigate spatial variations in the concentration of CO_2. The addition of CO_2 occurred far upstream from the combustor plenums, in both fuel and air lines to allow proper time for complete mixing prior to be injected into the RDC.

2.2.8 Oxygen Enrichment of Oxidizer

Another facility improvement is a pure, gaseous oxygen handling system that allows for air enrichment prior to introduction into the RDC. This system is also capable of being used for oxygen replacement if an in-line vitiator is incorporated in the future. This system is sized to be capable of providing up to approximately 150 g/s of gaseous O_2. An in-line, swirl mixer is included along the air delivery system far upstream from the RDC plenum such that the O_2 and air are introduced orthogonal to one another, with the air introduced offset from the centerline to induce swirl. A rendering of the mixer is displayed in Figure 2.7 with the paths that the air and O_2 take being highlighted. Air enters radially in the mixing element through four offset ports while O_2 flow enters axially to avoid direct impingement on surfaces outside of the O_2 clean portions of the supply system. The mixer was designed to accomplish complete mixing upstream prior to arriving in the RDC plenum while minimizing the pressure drop across the mixing element despite turning the flow of air. The enriched air is then flowed towards the RDC like normal. The flow of O_2 is controlled by metering across a choked orifice prior to the mixing element, similar to the air/fuel controllers. The O_2 system is not intended to be used as the sole provider of the oxidizer to the RDC over air at this time. The O_2 system is now a permanent part of the facility air supply sytem and is secured from contamination when not in use by the large check-valve into which the red O_2 arrow is pointing in Figure 2.7.

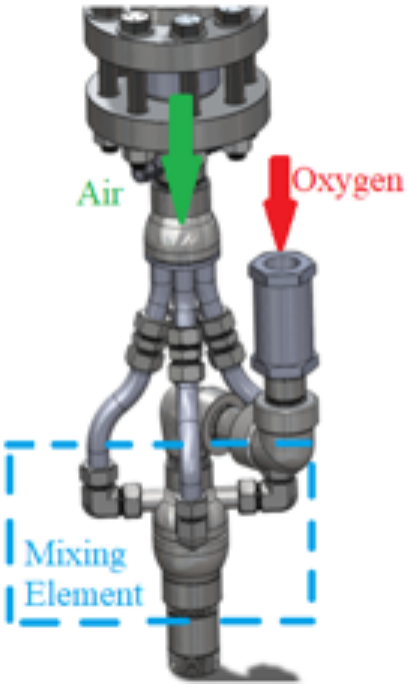

Figure 2.7: Rendering of O_2 supply/mixing system.

2.3 Development of Analysis Techniques and Diagnostics

2.3.1 Injector Blockage Model

In a previous work focused on the enhanced axial air inlet RDC design, we developed the effective blockage fraction metric defined per equation 2.1 below [9]. A standalone publication specifically focused on the development of and ongoing efforts to improve this methodology is in work. This metric was developed using data obtained during hot flow or reacting test cases as compared to that obtained during cold flow or non-reacting cases. This metric relates the inlet air mass flux during hot flow and during cold flow at the same plenum pressure to determine an equivalent "unblocked" region of the inlet, which allows us to deduce the fraction of the inlet that is "blocked." The blocked region is defined to be the fraction of the total inlet area in which net-zero flow occurs. Further work is ongoing to validate and expand this metric and analyze its implications on other measures of performance. The metric was originally presented as a mean measure of blockage for individual test cases, but has also been expanded to operate on a per-sample basis from both low (200 Hz sample rate) and high-speed (0.5-1 MHz sample rate) plenum pressure measurements. When operating with measurements obtained from the Kulite XTEL-190L-250A pressure transducers within the plenum, the high-speed plenum effective blockage fraction is referred to as B_{HSP} (Calculated using Equation 2.1 on a per-sample basis). An example of how this methodology is utilized in practice is highlighted in Figure 2.8. The markers represent measured plenum pressures during reacting cases (hot flow), with the solid back curve representing plenum pressures observed during non-reacting cases (cold flow). This selection of data is from the enhanced axial air inlet design with no exhaust restriction.

$$B = 1 - \frac{\dot{m}''_{\mathrm{Hot}}}{\dot{m}''_{\mathrm{Cold}|P_{\mathrm{pl}}}} \tag{2.1}$$

Several other methods exist in the literature to calculate similar metrics that seek to quantify effective inlet blockage. Deng *et al.* [10] put forth several methods utilizing pressure changes within the plenum and/or channel. One of these methods uses a similar formulation to that of B, but instead of comparing the inlet air mass fluxes at a given plenum pressure, it compares the plenum pressure at given inlet air mass fluxes, and will be referred as B_{P}. The relevant quantities for an individual case are

shown in Figure 2.8. An additional method put forth uses high-speed channel pressure measurements to evaluate the mean fraction of time within an average cycle in which the channel pressure exceeds the mean pressure within the plenum. This method assumes that flow is locally arrested at the inlet when channel pressure exceeds that of the plenum. Further analysis of the validity of this method is ongoing.

$$B_{\mathrm{P}} = 1 - \frac{P_{\mathrm{pl}_{\mathrm{Cold}}|\dot{m}''}}{P_{\mathrm{pl}_{\mathrm{Hot}}}} \tag{2.2}$$

Due to the relative ease of access to the upstream side of the air inlet throat in the enhanced axial air inlet RDC configuration, a test sequence was devised to validate the developed effective blockage fraction metric (B). This test sequence was conducted solely with non-reacting flows. Sections of flexible gasket material were fabricated and installed on the upstream side of the air inlet throat to physically restrict the flowpath with a known artificial blockage. These pieces were sized to represent approximately 50%, 25%, and 12.5% blockages. In order to represent the azimuthally varying blockage region during hot-flow tests, these artificially blocked cold-flow tests were conducted both with the blocking pieces centered on the azimuthal position of the CTAPs and diametrically opposed. The mean of these two conditions for each target inlet air mass flux thus represents an analog to the RDC during operation. As can be seen in Figure 2.9, the B (and associated B_{HSP}) metrics both closely predict the actual known blockage fractions, while the B_{P} metric presented by Deng *et al.* significantly under-predicts blockage at low inlet air mass fluxes. The slight under-prediction of the effective blockage in the most restrictive AR = 5 inlet configuration is believed to be due to the gasket material of discrete thickness blocking the inlet slightly upstream of the minimum throat area.

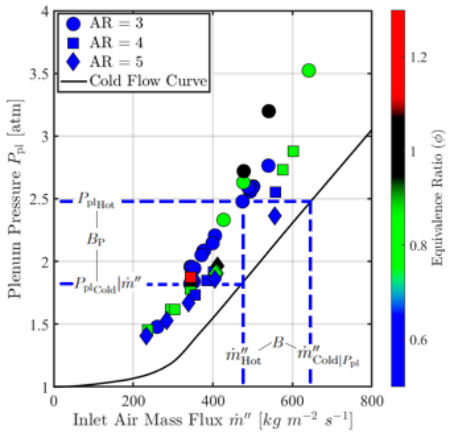

Figure 2.8: Methodology used to calculate effective inlet blockage fractions B and B_{P}.

The variation in effective blockage fraction for a range of inlet conditions and inlet/exhaust configurations indicates several apparent trends. This can be seen in Figure 2.10. The data presented here represent a range of test cases conducted with

hydrogen-air mixtures at ambient inlet temperatures in the AAI inlet configuration (a) and the enhanced AAI configuration (b). Data is presented for cases that had a 50% converging nozzle (cyan outline) and no exhaust restriction (black outline). For a given configuration and constant ϕ, B is generally found to decrease with increasing inlet $\dot{m}''$. An increase in ϕ generally results a corresponding increase in B. The addition of a 50% converging nozzle results in a consistent increase in B. A value of blockage for a given $\dot{m}''$ implies that a larger plenum pressure is required. Analysis is ongoing to relate the effect blockage has on overall pressure gain, as this metric is traditionally calculated based upon the total/plenum pressure that is directly impacted by any variation in B.

Although this methodology was developed to characterize the blockage at the air inlet, the same relationships can be used to characterize fuel inlet blockage. As the current formulation of B requires cold flow pressure/flowrate relationships and we have not historically performed cold flow characterization of the fuel plenum/injectors, historical data cannot directly utilize the methodology above. We have begun to incorporate He cold flows that will be used going forward to generate similar measures of blockage for the fuel injector(s). The cold flow curve can also be inferred using choked flow calculations, but at this time all blockages calculated on the air inlet utilize real pressure/flowrate data obtained under non-reacting conditions and makes no assumptions as to the flow characteristics of the inlet.

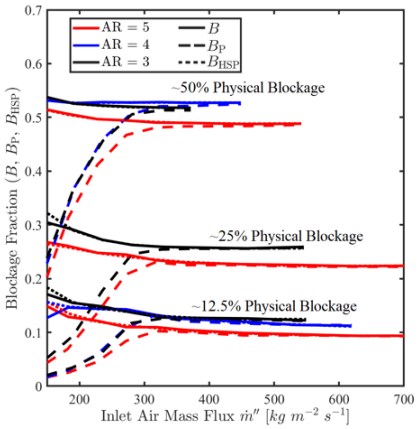

Figure 2.9: Evaluation of methods used to determine effective inlet blockage using known artificial blockage.

2.3.2 Statistical Analysis of High-Speed Pressure Measurements

The strength of any of the observed waves is defined as the pressure ratio across the wave as measured by the high-speed pressure sensors in the plenum. An algorithm has been constructed that examines all the individual detonation cycles in the high-speed pressure measurements over a sliding window. For each detonation cycle and for each pressure measurement, the points of the maximum and minimum pressure

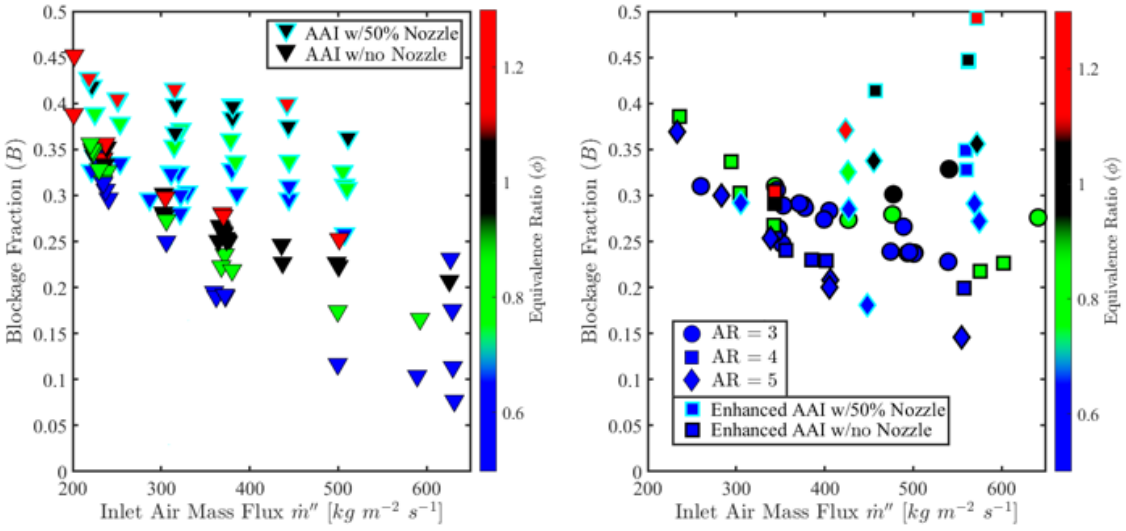

(a) (b)

Figure 2.10: Variation of B in a) AAI configuration and b) Enhanced AAI configuration.

across the cycle are found and stored. This allows for a statistical measure of the pressure variation (ratio p_r) caused by the waves observed at different measurement locations, denoted by a subscript number corresponding to that sensor location. Here we denote a superscript of "+" to be point after the passage of the wave, which corresponds to the peak pressure across the cycle. Similarly, we denote a superscript of "-" to be the point before the arrival of the wave, which is typically the minimum pressure in the cycle. The pressure ratio (p_r) is defined as the ratio. For example, the pressure ratio measured in the plenum is defined as:

$$p_{r,2} = \frac{p_2^+}{p_2^-} \tag{2.3}$$

In addition, the algorithm can be used to find the time difference (Δt) between the observed peaks in the pressure traces measured in the channel and plenum. This is done by storing the time that observed peaks occur and subtracting the time that the wave is observed in the channel from the time that the wave is observed in the plenum of the same cycle. When the high-speed pressure measurements are aligned circumstantially but spaced apart axially, this allows for the estimation of the time of that a wave would travel from the bottom of the detonation to the plenum location. This time difference is analogous to the time of flight in an unsteady 1D shock tube problem and can be also be used to measure the shock strength in the plenum.

2.3.3 Method of Circuit Wave Analysis

While our interest in the development of the CWA method was motivated by RDC research, its interpretation and application can be generalized to a class of problems where a time-dependent periodic phenomenon of interest evolves over a spatially periodic domain. In this case, some observable of the phenomenon can be reduced to a two-dimensional (2-D) field composed of one periodic spatial dimension and one linear temporal dimension. For representation purposes, a 2-D dimensional representation can be obtained by unwrapping the cyclical spatial dimension. Borrowing the terminology from 1-D unsteady compressible wave dynamics [11], this 2-D field can be referred to as a space-time, or simply $x-t$, diagram. For applications like RDCs, the spatial dimension x represents the azimuthal direction Θ along the annular gap of the RDC.

Adapting a Fourier series representation of any periodic quantity, the $x-t$ diagram can be represented as a superposition of an infinite number of harmonic waves

travelling through the spatial (X) dimension as a function of time t. Each wave component j can then be expressed in the form:

$$W_j(X,t) = A_j \cos\left(2\pi f_j t - 2\pi k_j X + \phi_j\right) \tag{2.4}$$

Here f_j is the temporal (linear) frequency that would be measured by an observer at a fixed position, while k_j is the spatial (linear) frequency of the wave at any moment in time. Lastly, A_j is the amplitude of the wave and ϕ_j is its phase. If the system of waves does not change in time (i.e. f_j, k_j, A_j, ϕ_j constant) and it is sampled over a sufficiently long sampling time relative to the temporal frequencies of interest, then a 2-D spatio-temporal Fourier transform of the $x-t$ diagram would be sufficient to describe the properties of any waves in the system [12]. However, if the properties of the system change over short time scales, then a 2-D Fourier transform may not be sufficiently sensitive over the time scales of interest to assess these quantities in an accurate manner. The circuit wave analysis method proposed here has been developed specifically to analyze this latter case.

The CWA method ultimately depends on analyzing the $x-t$ diagram in varying frames of reference, because of this we will first establish some properties of spatially and temporally periodic waves. First, we will demonstrate that an arbitrary spatially periodic function can be made to have some velocity in the periodic spatial domain through a simple coordinate transformation. The resulting wave can be represented in terms of a summation of moving cosine waves W_j. From the applied transformation we can define a relationship between temporal frequency, spatial frequency, and wave velocity. Secondly we will demonstrate that a wave component W_j when shifted into a moving frame of reference has a linear shift in temporal frequency.

First consider a spatially periodic function $P(x')$ of period L on a periodic spatial domain (e.g. a circle) of length L.

$$P(x'+L) = P(x') \tag{2.5}$$

and let us represent it in a Fourier series representation:

$$P(x') = \sum_{j=0}^{\infty} A_j \cos(2\pi k_j x' + \phi_j) \tag{2.6}$$

where A_j is the coefficient of the j-th component, ϕ_j its relative phase, $k_j = j/L$ the spatial frequency and j an integer number.

We can consider this function to represent the spatial distribution of a traveling wave moving at a constant speed v_w. This representation is then equivalent to applying a Galilean transformation of the type $x' = X - v_w t$ to $P(x')$. Then, the transformed function representing the traveling wave can then be written as:

$$P(X,t) = \sum_{j=0}^{\infty} A_j \cos(2\pi k_j X - 2\pi k_j v_w t + \phi_j) \tag{2.7}$$

from here a temporal frequency f_j can be defined as

$$f_j = k_j v_w \tag{2.8}$$

This frequency applies for all components of the series. Equation 2.7 can be taken to represent the Fourier series representation of a single wave, of arbitrary spatial distribution, traveling at a constant speed v_w. The form of Eq. 2.7 is that of a summation of wave components W_j. The derivation of Eq. 2.7 was for a single waveform moving at a constant velocity, however as it is written it can equally apply to any summation of waves travelling at any arbitrary speeds and directions if we use the simple f_j instead of $k_j v_w$ and relax k_j to also be arbitrary. This ultimately is a representation of a 2-D Fourier transform taken on a 2-D field with one spatial and one temporal dimension.

Now we will consider the impact on a wave system properties by observing the field in a moving frame of reference, starting with $P(X,t)$, which represents a spatially periodic wave travelling at constant velocity. Let us apply a Galilean transformation of the type $X = y + vt$ where v is an arbitrary constant velocity. This transformation simply corresponds to a Galilean frame of reference transformation. With this new transformation, the observable in the moving frame can then be represented as:

$$P'(y,t;v) = \sum_{j=0}^{\infty} A_j \cos(2\pi k_j y + 2\pi k_j (v - v_w) t + \phi_j) \tag{2.9}$$

From Eq. 2.9 we can recognize that the temporal frequency of the j-th mode observed in this moving frame is:

$$f_j^{(v)} = k_j \left| (v - v_w) \right| \tag{2.10}$$

$$= \frac{j}{L} \left| (v - v_w) \right| \tag{2.11}$$

which can be recognized to simply be an alteration of the observed frequency due to the Doppler effect. In practice, the transformation allows us to observe the wave and hence identify its frequency content, in a frame with a relative speed $v - v_{\mathrm{w}}$, which leads to an observed relative frequency $f_j^{(v)}$. The absolute sign in Eq. 2.11 is included to ensure that the observed frequency remains a positive value for all values of shift velocity v, i.e. for $v < v_{\mathrm{w}}$. Furthermore and more importantly for our purposes, this transformation shows that if we observe the system from a frame moving at a speed $v = v_{\mathrm{w}}$, the observable will appear temporally stationary. In practice, CWA is designed to seek this condition.

In this section we provide the mathematical description of the *Circuit Wave Analysis* technique. We will leave a more thorough accounting of properties and implementation to future work. The technique depends on a spatio-temporal measurement, such as for example high-speed video. For the work done here, high-speed chemiluminescence video is the spatio-temporal measurement. Given the spatio-temporal measurements of an observable in a spatially periodic process controlled by the propagation of a number of wave systems, the technique reduces the information contained into these measurements into a measure of the time-variation of the average value of the wave speed, direction, strength and multiplicity of any coherent wave present in the system. This information is derived by reducing the spatio-temporal measurements using the following steps:

1. Construct the $x - t$ diagram from the spatio-temporal measurements of an observable over the closed, cyclical domain.

2. Transform the $x - t$ diagram into a velocity-frequency plot, which is what we also refer to as the *Galilean-shifted Fourier spectrum* (GSFS), by applying what we term *Galilean-shifted Fourier transform* (GSFT).

3. Reduce the GSFS through a line integration step to produce what we refer to as *Radon curves*. This step is related to a particular implementation of the Radon transform (hence its name).

4. Evaluate the Radon curve to identify any waves present, and then extract a measure of their wave speed and multiplicity.

5. Using the results of the Radon curve, further evaluate the GSFS to extract a measure of wave strength.

Consider a single mode of the Fourier series representation of an arbitrary wave moving at a constant velocity through a periodic domain:

$$W_j(X,t) = A_j \cos(2\pi k_j X - 2\pi f_j t + \phi_j) \tag{2.12}$$

Consider now a 2-D field composed of an infinite number of cosine waves:

$$B(X,t) = \sum_{j=1}^{\infty} W_j(x,t) \tag{2.13}$$

This is what will be referred to as the $x-t$ diagram. Again apply a Galilean transformation $X = y + vt$:

$$B'(y,t;v) = B(y+vt,t) \tag{2.14}$$

Consider again the representation of a wave system described by $P'(y,t;v)$. We can now apply the 1-D Fourier transform to $P'(y,t;v)$ in time, for each spatial position y:

$$\hat{P}'(y,f;v) = F_t\{P'(y,t;v)\} \tag{2.15}$$

where $\mathfrak{F}_t\{\cdot\}$ is used to indicate the 1-D temporal Fourier transform operator and f is used to indicate temporal frequency in the Fourier domain. The operator indicated by Eq. 2.15 is what we referred to as the Galilean shifted Fourier transform (GSFT). A set of Galilean shifted Fourier transforms can be constructed over an arbitrary range of shift velocity v, for example by considering a set of equally spaced discrete values within a sought range of shift velocities, $-v_r < v < v_r$, for all spatial points y. The range of shift velocity (i.e., v_r) to seek our solution is arbitrary, but results depend on the temporal sampling resolution and the duration of time sequence used to compute the GSFT. Then, from the set of Fourier transforms we define the Galilean shifted Fourier spectrum as:

$$G(f,v) = \max_y \left\{ \hat{P}'(y,f;v) \right\} \tag{2.16}$$

where we note that the maximum is taken over the y dimensions, i.e. $G(f,v)$ is the maximum Fourier coefficient from all locations y for a given frequency f at a given transformed velocity v. The maximum over the y dimension is taken to preserve the energy of the wave as the frame of reference moving with the wave is approached.

Given $G(f,v)$, the next step is to generate a set of Radon curves by integration of $G(f,v)$ along lines defined by Eq. 2.11. The set of Radon curves arises from

considering all spatial modes n, one curve for each harmonic n. In practice, the projection can be conducted as a line integration of $G(f, v)$ along lines defined by Eq. 2.11, which can be expressed as:

$$R^{(n)}(v) = \int_{v'=-\infty}^{\infty} \int_{f'=0}^{\infty} G(f', v') \delta \left(f' - \left| \frac{n}{L}(v - v') \right| \right) \mathrm{d}f' \mathrm{d}v' \tag{2.17}$$

with $n = 1, 2, 3....$ This operation is analogous to conducting a Radon transform of $G(f, v)$ for lines of the form defined by Eq. 2.11. It is also important to note that in practice the line integration defined by Eq. 2.17 will be conducted on a discretized domain of finite size. Thus, it is critical that the integration is conducted over a sufficiently large portion of the (f, v) plane. A typical GSFS will have lines emanating from the velocity axis (denoting waves), "large" here means sufficient to visualize the 'V' shape that results from the absolute value used to represent frequency. More about the exact nature and limits of this range will be discussed in a future work.

The Radon curves $R_n(v)$ ($\{n = 1, 2, 3, ...\}$) are then further analyzed to seek the values of shift velocity at which all local maxima occur. If a single wave exists, then the Radon curve for each of the n modes has exactly one maximum at a shift velocity v, and each mode will have the same shift velocity, i.e., $v = v_{\mathrm{w}}$ for all n. If multiple independent waves exists, then multiple maxima exist, each at its own wave propagation velocity. This condition corresponds to seeking the condition where the observable is observed to be stationary relative to a frame of reference moving with the wave being identified. In practice, the maxima of the Radon curves and their corresponding abscissa (i.e., v_{w}) can be extracted using a local curve fitting of the peaks of the Radon curves to get sub-resolution accuracy of the shift velocity of a given wave.

As a result of analyzing the Radon curves, the characteristics of the wave system can finally be extracted. First, the shift velocity at which the Radon curve for mode n has a local maximum represents the velocity of a wave: $v = v_w$. Hence, the sign represents the direction of propagation relative to a reference positive direction, while the magnitude is simply the speed of the wave.

The value of the maximas is related with the energy associated with that mode. In practice, because the energy associated with the harmonics rapidly decreases, only the first few modes can be detected. However, the most relevant mode is the first mode that results in a non-zero local maxima in the Radon curve because it represents the multiplicity ω of the wave system.

In the context of RDC studies, the multiplicity is simply the number of waves

(e.g., detonation waves) present in the system; hence $\omega = 1$ for a single wave, $\omega = 2$ for two waves, and so forth.

From knowing the velocity of the wave system, a measure of the wave strength or intensity can then be defined based on a measure of the energy associated with the wave system. Because in general multiple wave systems can be present simultaneously, a measure of the energy for each wave system S is defined from the Galilean shifted Fourier spectrum by performing a local integration of $G(f, v)$ in a neighborhood of the wave velocity identified by the method:

$$S = \int_{f=0}^{\delta f} G(f, v_{\mathrm{w}}) \mathrm{d}f \tag{2.18}$$

where $\delta f > 0$ represent an arbitrary small region near the velocity shift axis at the identified wave velocity v_{w}. This form is introduced to capture all of the energy that is distributed over all of the harmonics of the wave system, all of which converge to $(f = 0, v = v_{\mathrm{w}})$ on the (f, v) plane of the GSFS.

Although the method described here is constructed for a continuous-time and -space observable, in practice it is implemented from a discretized observable, where discretization is both in time and space. Nevertheless, we use the continuous-time formulation to identify some of the properties of the method. In addition, the method is constructed under the following main underlying assumptions:

1. The wave velocity is constant, $|v_{\mathrm{w}}|$ = constant and the wave does not change direction;

2. If multiple wave systems exist, they linearly superimpose.

The first assumption should be viewed in the sense that the wave speed should not vary significantly over the observation time duration over which it is estimated. Similarly, the wave should not change its direction as to introduce complexities in the GSFS and its interpretation. The result of this is that the inferred wave speed is an average measure over the observation time, where averaging is introduced by the Fourier transform operation. However as will be demonstrated in a future work currently under development, the ability to use the GSFS and line integration method allow for significantly improved temporal sensitivity over a standard 2-D Fourier transform allowing for use in determining wave properties in situations where a 2-D Fourier transform is no longer appropriate.

2.3.4 Model of Injector Response Time

One of the key parameters that is thought to be important in RDC physics is the response time of the injectors, i.e. how long it takes for the injector to begin issuing a quasi-steady stream of fuel or air after their flow has been disrupted by the passage of a detonation wave. The response time of an injector is ideally based on the velocity at the exit of the injector. We have developed a model for the estimation of the response time of injectors using a combination of the unsteady, one-dimensional (1-D) method of characteristics applied to wave propagation, measured quantities, and estimated detonation properties to construct an estimated velocity and density profile from which a response time can be computed.

A schematic of the general flowfield used to solve for the response time is shown in Fig. 2.11. When the detonation passes over an injector an instantaneous pressure boundary condition is applied to the exit plane of the injector, which is followed by an expansion wave. A hypothetical flowfield was constructed with the initial behavior being that of a shock tube followed by an expansion wave. Around $(x = 0, t = 0)$ we can see the traditional shock tube problem with the driver being state ④ and the driven being state ①. The normal shock generated by the detonation wave is represented as a yellow line labeled NS. Left running expansion waves originating from the original shock tube problem and from reflections off the contact surface CS (dashed black line) between the fluid that remains inside the injector and that in the detonation channel at the time of arrival of the incident detonation wave are shown in red, while the right running expansion wave modeling the expansion wave traveling with the detonation wave is shown in blue. The wave system is solved numerically to include reflections from the distorted contact surface shown as a dashed line labelled CS. The properties of the six states used to define the field, are summarized in Table 2.1. The base and peak pressures (p_{base} and p_{peak}, respectively) denoted in the table are defined from high-speed pressure measurements in the detonation channel from experiment, and they are defined as the average minimum and maximum pressure observed at each cycle. The steady velocity u_{s} is found as part of the solution. Solving for this overall flowfield allows for the computation of both velocity and density along the line $x = 0$. To find a unique flowfields of a given injector and operation condition the following constraints are imposed: (1) the cycle-average mass flow rate through the injectors match the mass flow rate of the experiment; (2) the velocity of the stream at the end of the detonation cycle be the same as the velocity in the stream just prior to the arrival of the detonation wave. We also treat the post detonation

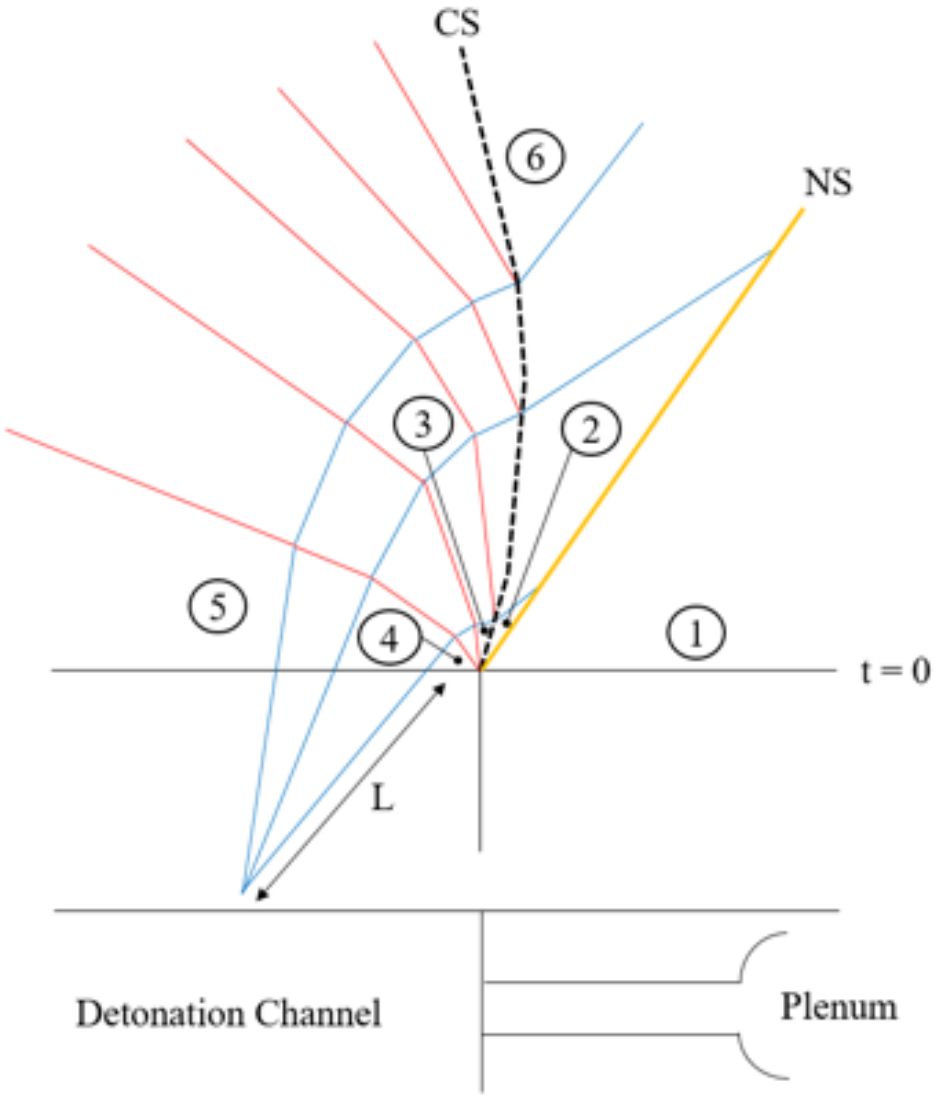

Figure 2.11: Schematic of the 1-D method of characteristics flowfield constructed to estimate the response time of the injector.

State	Velocity	Pressure	Composition
①	u_s	p_{base}	Air/hydrogen
②	Solved for	p_{peak}	Air/hydrogen
③	Solved for	p_{peak}	Detonation products
④	u_s	Solved for	Detonation products
⑤	Solved for	Solved for	Detonation products
⑥	u_s	Solved for	Air/hydrogen

Table 2.1: Summary of quantities used to estimate the response time of injectors according to the schematic of Fig. 2.11.

expansion as a centered wave within the field which has its origin at a time $t < 0$. The flowfield prior to $t < 0$ is a non-physical space constructed only so that when the right running expansion wave begins to interact with the waves associated with the shock tube problem, the overall flowfield approximately mimics the dynamics expected in the RDC.

The right running expansion wave has its origin at a time before $t = 0$ at an x location such that the head of the expansion wave intersects the origin of the field. The location can be parameterized by a single variable L as the trajectory of the head of the expansion wave is fixed for a given state ④. Here L can be modified to satisfy Eq. **??** under the assumption that the expansion wave ends at $x = 0$ and $t = \tau$. This assumption results in a worst case scenario estimate of the response time, but we believe that the general trends will remain unaffected by this assumption.

After computing the resulting flowfield based on this wave model, we can compute a velocity and density along the $x = 0$ line. In addition, from the computed quantities we can also compute the temporal variation of the equivalence ratio (as if the air and fuel would instantaneously mix right at the exit of the corresponding injectors) and fuel-to-air momentum flux ratio. Examples of the temporal evolution over the cycle of the computed relevant quantities are shown in Fig. 2.12. From the computed velocity and density it is possible to compute a mass flow rate for the cycle. We can then iterate on u_s in order to solve the system such that Eq. **??** is satisfied.

Once all constraints have been satisfied we can define a response time based on the temporal variation of velocity. In this study we consider the response time to be the time at which the stream velocity is within 10% of the acoustic speed (computed at the static temperature of the given stream) of the final stream velocity as shown

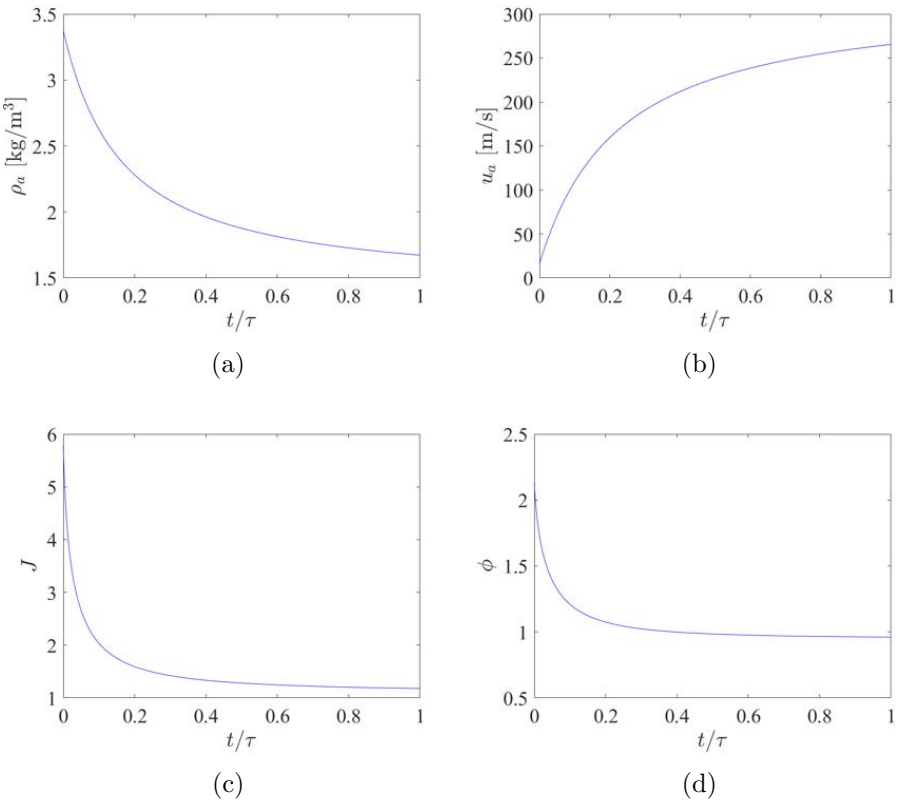

Figure 2.12: Example of the results of the unsteady 1-D method of characteristics applied to the calculation of the injector response for a representative operating condition of $\dot{m} = 0.3$ kg/s at $\phi = 1$. Temporal variation of: a) Density of air stream; b) Velocity of air stream; c) Fuel-to-air momentum flux ratio; and d) Equivalence ratio.

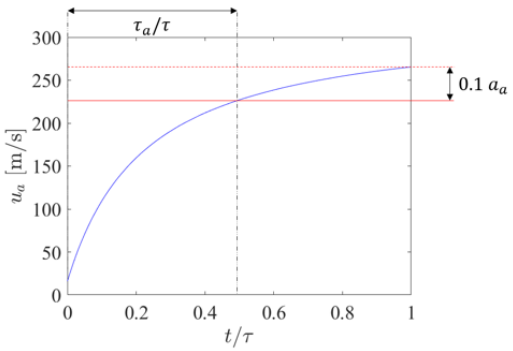

Figure 2.13: Definition of the response time used for the air and fuel streams.

in Fig. 2.13.

2.4 Analysis of Secondary Waves

2.4.1 Identification of Secondary Waves

Figures 2.17 and 2.16 give examples of the manifestation of secondary waves. These figures show time history of wall static pressure acquired at a fixed operating condition but with different strength secondary waves. The pressure time history trace shown in Fig. 2.16(a) appears qualitatively more regular than the trace shown in Fig. 2.17(a). However, if we consider their power spectra, which are shown in Figs. 2.16(b) and 2.17(b), we can note that both signals are characterized by well-defined spectral tones, suggesting that both pressure signatures are periodic and composed by a finite number of overlapping modes, but possibly characterized by different propagation speeds and coupled non-linearly. The more regular case of Fig. 2.16(b) only has a single tone and its corresponding harmonics, with the fundamental at approximately $0.8f_{\mathrm{CJ}}$, where f_{CJ} is the nominal rotational frequency of an ideal detonation wave at the global equivalence ratio estimated at the mean diameter of the RDC flow path ($f_{\mathrm{CJ}} = D_{\mathrm{CJ}}/\pi\overline{D}$). This frequency and its harmonics correspond directly to the detonation wave and its propagation. The case of Fig. 2.17(b) shows similar tones and harmonics starting at $0.8f_{\mathrm{CJ}}$, which correspond to the detonation wave, but it also includes another tone (fundamental and harmonics) appearing at approximately $1.1f_{\mathrm{CJ}}$. As it will be identified next, this tone is the signature of a pair of waves

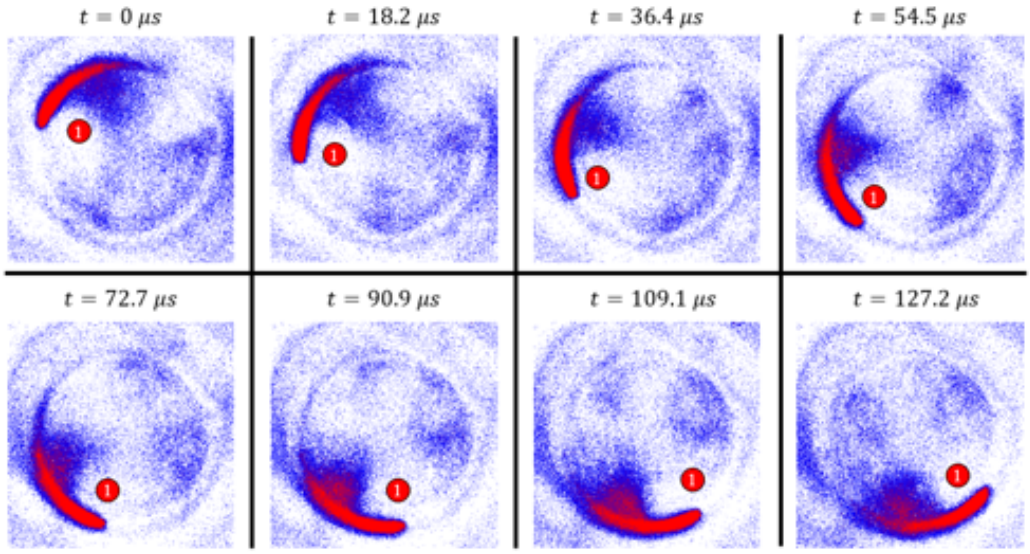

Figure 2.14: Series of aft-end OH* chemiluminescence images taken in RDC showing detonation channel with no secondary waves present.

travelling through the channel counter to the main detonation wave. The presence of a detonation wave and a secondary wave can also be observed by analysis of high-speed end-view video of chemiluminescence. Using a process similar to what described by Bennewitz et al. [12], high-speed imaging can be unfolded into a space-time $(x-t)$ diagram as is shown in Fig. 2.18. The $x-t$ diagram shows the luminosity of emission of the reacting flowfield throughout the annulus (vertical axis) as a function of time (horizontal axis). In Fig. 2.18 it is possible to recognize the main detonation wave (A) travelling up and to the right with time, while there is a fainter pair of waves (B) travelling down and to the right with time. It is this pair of waves that corresponds to the tone at $1.1 f_{\mathrm{CJ}}$ observed in Fig. 2.17(b). For a given run where the secondary wave tone is present in one high-speed measurement, it is likewise present in all other accompanying high-speed measurements of other observables (e.g. OH* chemiluminescence). The exact characteristics of this additional wave depend on the operating conditions and geometry. These aspects will be clarified in this section.

To extract information about secondary waves, we have developed a technique we term *circuit wave analysis* (CWA), which is briefly described in section 2.3.3. CWA reduces the information about wave systems contained in the $x-t$ diagram

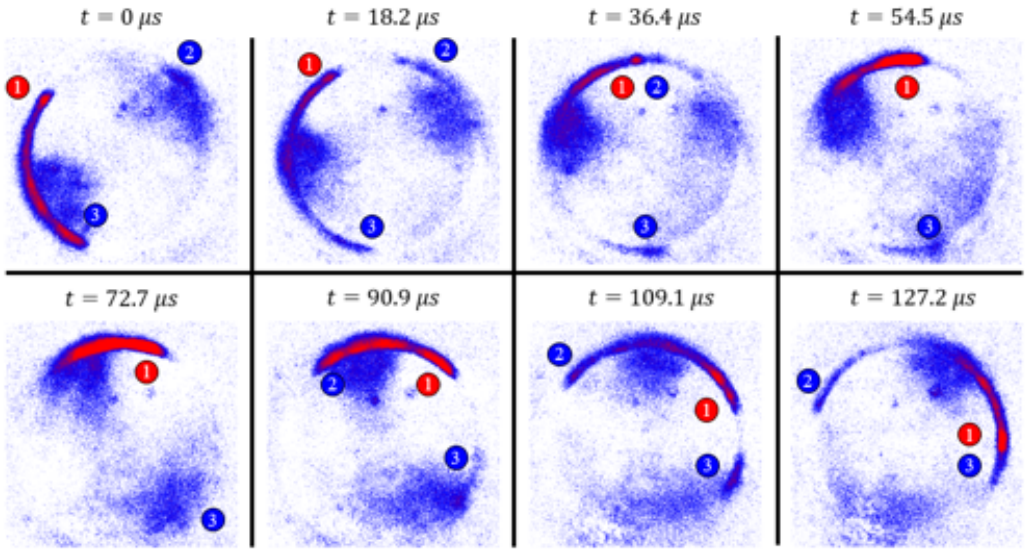

Figure 2.15: Series of aft-end OH* chemiluminescence images taken in RDC showing detonation channel with secondary waves present.

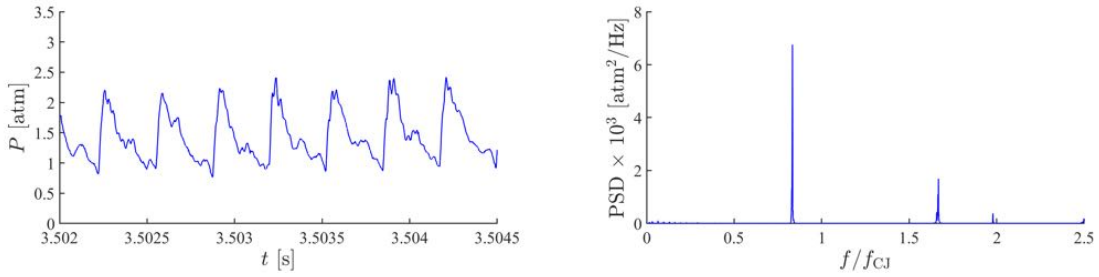

(a) (b)

Figure 2.16: Examples of time variation of pressure measured during an experimental condition which resulted in operation both with and without secondary waves, here information with no secondary waves is shown. a) Time variation of pressure b) Fourier spectra generated from high speed pressure trace.

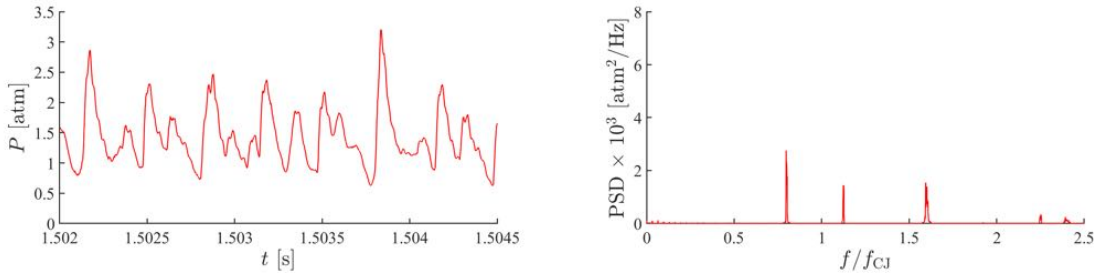

(a) (b)

Figure 2.17: Examples of time variation of pressure measured during an experimental condition which resulted in operation both with and without secondary waves, here information with secondary waves is shown, data comes from the same experimental run as Fig. 2.16. a) Time variation of pressure b) Fourier spectra generated from high speed pressure trace.

constructed from time-resolved end-view videos of flame chemiluminescence through the closed circuit of the annulus. The result is temporal information of each wave system present in the detonation channel, such as the speed of wave, its direction and its strength measured by the intensity of chemiluminescence associated with the wave. With this approach we implicitly assume that a wave system is associated with both a pressure and light emission perturbation in the periodic operation of the RDC; i.e., the pressure variation associated with the wave system is coupled to chemical reaction. We will show that this is indeed the case for conditions studied here, however this might not always be the case.

2.4.2 Classification of Secondary Wave Systems

CWA has been applied to a range of operating conditions and geometries to extract the information about the properties of the wave system as a function of condition. An example of the temporal information extracted from CWA is shown in Fig. 2.19 for a specific operating condition and geometry. In this particular case we can observe that the system is composed of three different wave systems, labelled A, B and C in Fig. 2.19. Specifically, these waves systems are classified and referred to as follow:

A. Detonation (main) wave;

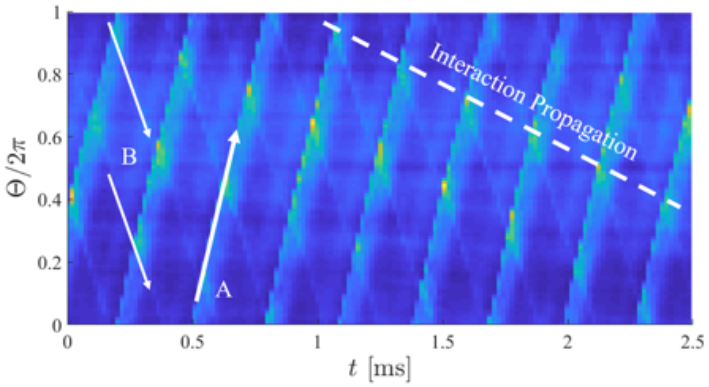

Figure 2.18: Example $x-t$ diagram showing propagation of waves within the annulus as a function of space and time.

B. Counter-rotating slow wave pair (CRWP);

C. Counter-rotating fast wave (CRFW).

Although what is shown in Fig. 2.19 is a specific case, we found that in general the operation of the RDC under the range of conditions and geometries (injection) considered in the study always produced operation with a combination of these three wave systems (for the detonating cases), although the relative strength of the three can vary from case to case. All three types of waves are azimuthal waves (i.e., they rotate across the detonation channel). In most cases the three wave systems are observed to travel and persist with stable properties (i.e., speed, direction and strength), in some cases they are also observed to change in strength, direction and speed during operation. Figure 2.19 shows the results of this temporal analysis, where the vertical axis is the velocity of a given wave system, the horizontal axis represents time, and the color bar represents the wave strength S as mathematically defined in appendix 2.3.3. Wave strength is an integral measure of the cumulative spectral energy of a given wave system based on light emission intensity. The case shown in Fig. 2.19 is an example of a condition of operation that, although being nominally constant, it is sensitive to some unknown parameter and exhibits changes in the operational behavior as captured by intermittent weakening of the secondary waves with an associated increase in detonation speed. For the majority of the conditions, the three wave

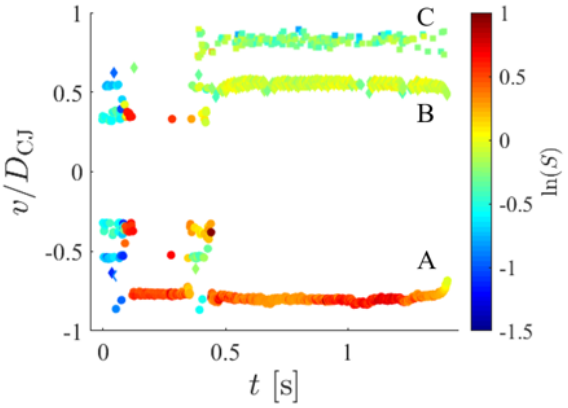

Figure 2.19: Time history of the speed, direction and strength of detonation wave and secondary waves extracted from temporal CWA. Shown is a case with all secondary waves present and with fluctuating CRWP strength.

systems operate at a nominally constant velocity and wave strength S. However for short windows of time occurring at approximately $t = 0.45, 0.7, 1.05, 1.25$, lasting approximately 50-100 ms, we observe that the CRWP reduces in wave strength while the detonation wave simultaneously accelerates. This kind of information would be difficult to ascertain from average Fourier spectra.

2.4.3 Speed of Secondary Wave Systems

Figure 2.20 shows a compilation of the mean speed for each of the three wave systems across all injector configurations (for all detonating cases) extracted from CWA. Each plot compares one of the three wave speeds against one of the other two, with all speeds having been normalized appropriately. The detonation wave and the CRFW are normalized by the ideal detonation velocity D_{CJ} (≈1900 m/s), while the CRWP by the speed of sound of the products of the ideal detonation a_{CJ} (≈1000 m/s), both evaluated at the nominal global equivalence ratio of that particular operating point. It is important to note that points in a given plot are only shown if that operation condition resulted in both waves being present. Values for the detonation speeds are called D, the CRFW U_F, and the CRWP U_S. Across all cases the detonation speed ranges from 0.6 to 0.9 of D_{CJ}, with the CRFW having a similar range of

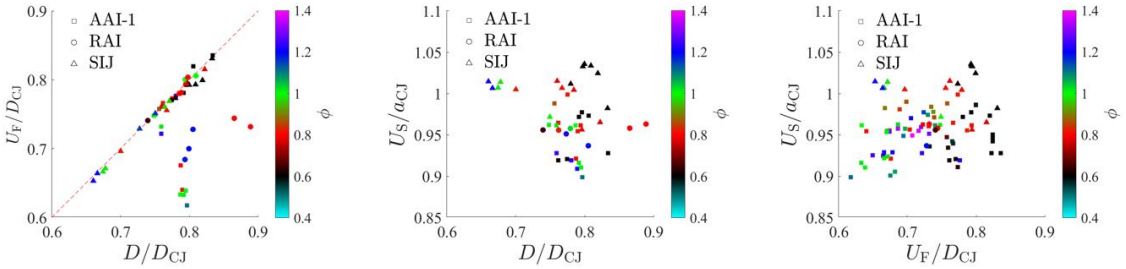

Figure 2.20: Summary of comparison of the speed of each of the wave system across all operating conditions.

values. The CRWP is slower, traveling in the range 0.9 to 1.1 of a_{CJ}. The CRWP speed is very near the sonic speed of detonation products in all cases, suggesting the wave is closely related to acoustic modes of the annular combustion chamber. The most immediate trend seen in the speed data is in Fig. 2.20(a). Here the majority of points lie on the 45° diagonal denoted by the dashed line. The strong relationship between the two speeds suggests that in most cases the propagation of the two waves is inherently coupled. The reason for a given operation condition resulting in one behavior versus the other is not currently known. It is possible that the detonation wave and CRFW moving at the same speed is a limiting case of the general interaction of the two waves. All injection configurations have exhibited both behaviors depending on operating condition. In Fig. 2.20(b) there is a possible equivalence ratio dependence on the relationship between the main detonation speed and its CRWP, with higher detonation speeds being associated with lower wave pair speeds. Higher equivalence ratios tend to move the curve closer to zero while lower equivalence ratios push the curve further out. Currently there is no readily discernible trend in Fig. 2.20(c). The general trends observed here are controlled by currently unknown mechanisms allowing for the possibility of confounding variables that have an impact on multiple properties.

2.4.4 Impact of Waves Interaction on Detonation Properties

Conditional dual phase-averaged analysis of time-resolved observables has been developed and deployed to understand the coupling between secondary and detonation

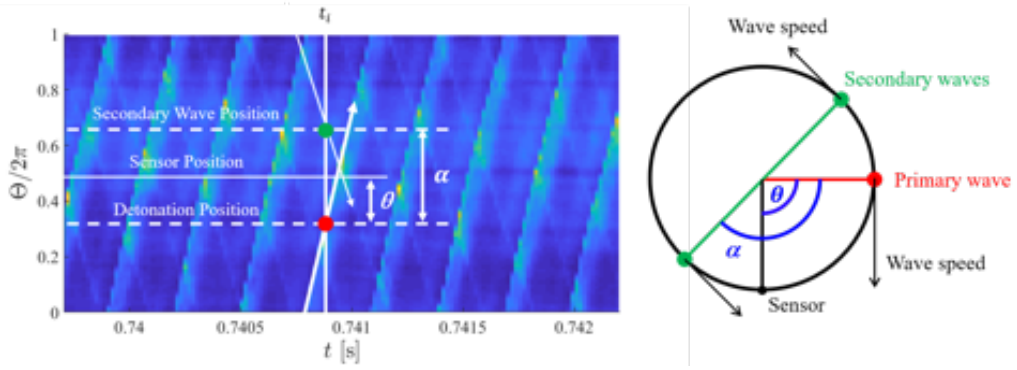

Figure 2.21: Graphical description of the formulation of conditional phase-average analysis and its construction from $x-t$ diagrams.

waves. In brief, given a time-resolved observable, such as time-histories of static pressure or OH* chemiluminescence emission, the analysis is based on tracking the position (i.e., relative phase) of a secondary wave relative to the main (detonation) wave to construct the phase-averaged state of the observable across a (detonation) cycle conditional to the relative phase between secondary and main (detonation) waves. If applied to a time-history measurement of static pressure as an example, this will result in the conditional phase-averaged pressure distribution across a cycle shown later in Fig. 2.22. For convenience, we simply refer to these plots as *conditional phase plots*.

Conditional phase plots are constructed by combining information about the propagation of a main detonation wave from $x-t$ diagrams (e.g., see Fig. 2.18) and a time-resolved measurement of an observable of interest (e.g., see Figs. 2.16(a) and 2.17(a)). Here the observable of interest is the static pressure measured at the outer wall of the detonation channel or the point-wise measurement of OH* emission at a fixed point in channel. Both quantities are used to extract different information, which will be discussed further below, about the interaction of the secondary wave with the detonation wave.

This process is first applied to the high-speed pressure measurements of the type shown in Fig. 2.17(a), and results in the color contour plot shown in Fig. 2.22. A horizontal slice of this contour gives the phase-averaged pressure distribution throughout the device in the detonation frame conditional to a relative phase angle α. By

construction the detonation wave is at a fixed location $\theta \approx 0$ but would appear to be travelling from left (negative θ) to the right (positive θ). By contrast, the secondary wave system appears to be traveling relative to the detonation wave in the negative θ direction with decreasing phase angle α to reflect the fact that the secondary wave moves counter to the detonation wave. In other words, regions with $\alpha > 0$ correspond to the two wave systems approaching each other at $\alpha = 0$, and $\alpha < 0$ correspond to the two waves moving apart in different directions. Because the CRWP system exists as a wave pair, the range of α is half that of θ. For the sake of clarity, the interaction between the detonation wave and a secondary wave is centered at $(\theta, \alpha) = (0, 0)$.

The effect of the interaction between the (main) detonation wave and the secondary wave on the pressure distribution across the detonation wave is shown in Fig. 2.22. The figure shows the conditional phase-averaged pressure distribution in the cycle, $\langle P(\theta|\alpha)\rangle$. From an initial assessment, it is clear that the phase-averaged distribution of pressure in the cycle, and particularly the peak pressure, has a strong dependence on α and therefor the motion of the secondary wave. The maximum value of the cycle peak pressure occurs near $\alpha = 0$, i.e. at the point of interaction between detonation and secondary wave. The presence of the secondary wave on the conditional phase pressure plot is identified by the set of 'streaks' at 45°. The secondary wave is associated with a relatively small, but not negligible, increase in pressure compared to the pressure rise provided by the detonation wave. Once the two waves begin to 'collide' near $(\theta, \alpha) = (0, 0)$, there is a larger than normal pressure spike compared to the time when the two waves are farthest apart ($\alpha/2\pi = 0.25$). The relative strength of the CRWP and the resulting interaction varies with operation condition; the case shown in Fig. 2.22 is representative of a case where the interaction is significant. Under conditions where the interaction is weak, the phase-average pressure is largely independent of α, and in the limiting case there is no secondary wave, there is no α dependence.

The effect of heat release distribution across the detonation wave during the overall interaction between the detonation wave and the CRWP is more complex than what is indicated by the pressure field. Because a direct heat release measurement is not possible, we use the OH* chemiluminescence emission at a fixed point in the detonation channel as an approximate marker of heat release. Using the same approach used to construct the conditional phase plots for pressure, conditional phase plots are constructed from the time-history measure of OH* chemiluminescence emission $\langle I(\theta|\alpha)\rangle$, where I indicates the relative intensity of OH* emission. An example of $\langle I(\theta|\alpha)\rangle$ for the same case with a significantly strong interaction as seen in Fig. 2.22,

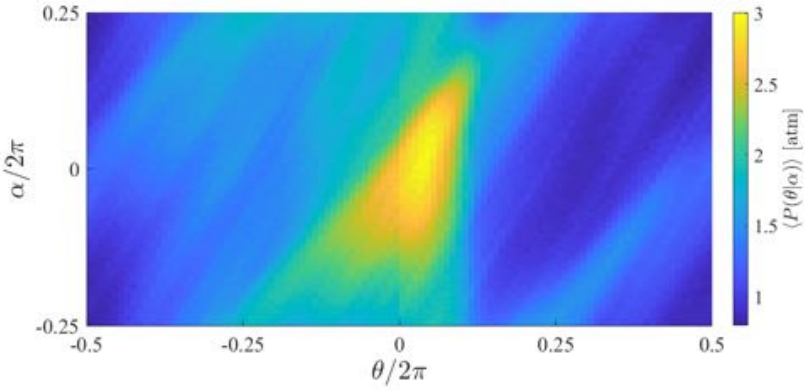

Figure 2.22: Example of conditional phase plot constructed from high-speed pressure measurements for $\dot{m}_a/A_{ch} = 82.6\,\mathrm{kg\,s^{-1}\,m^{-2}}$ and $\phi = 1.02$. This case has one of the stronger secondary wave systems observed with a pressure ratio $P_{p,+}/P_{p,-} = 1.5$.

is shown in Fig. 2.23. Here we have chosen to show $\langle I(\theta|\alpha)\rangle$ on a logarithmic color plot due to the high intensity associated with the OH* compared to the rest of the channel. In comparing $\langle I(\theta|\alpha)\rangle$ and $\langle P(\theta|\alpha)\rangle$ it is important to point out that the measurement of pressure and OH* chemiluminescence emission are not temporally or spatially correlated with one another. This is due to the finite response of the high-speed pressure sensor that introduces an attenuation of the measured pressure variation, as well as a time delay estimated to be around $10 - 15°$ with respect to the OH* chemiluminescence. Since the OH* chemiluminescence was acquired with a PMT with high temporal resolution, this limitation is not significant for the OH* measurements. As a result, events occurring at a specific value (θ, α) in one quantity do not necessary correlate with the same (θ, α) point in the other. Here we have shifted the OH* field such that the point at $(\theta, \alpha) = (0, 0)$ is associated with the minimum peak of $\langle I(\theta|\alpha)\rangle$ (defined later). In addition, the horizontal axis has been shifted to center most of the OH* intensity (heat release), i.e. the detonation wave, at $\theta/2\pi = 0$.

Figure 2.23 shows that the OH* field has a more complex behavior than the pressure field. Most of the OH* emission remains limited around the detonation front $(\theta/2\pi = 0)$, but low-intensity striations in the field are present and are associated with the secondary wave, in this case the CRWP, shown as dashed lines in Fig. 2.23.

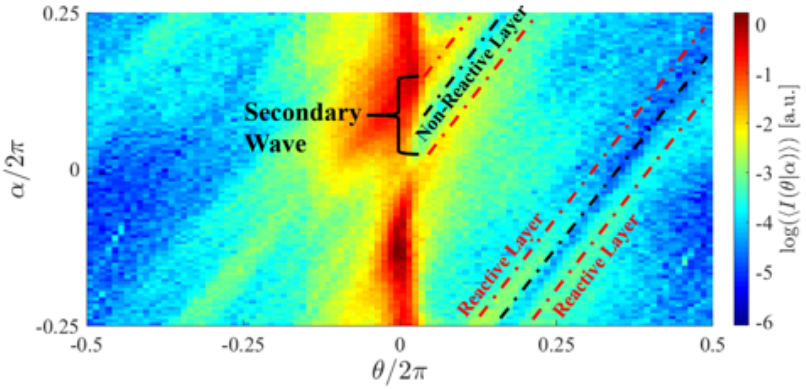

Figure 2.23: Conditional phase plot $\langle I(\theta|\alpha)\rangle$ constructed from OH* chemiluminescence measurements for the same case of Fig. 2.22.

In addition, $\langle I(\theta = 0|\alpha)\rangle$ shows that there is a structure to the emission as the phase difference between waves varies: far from the interaction between waves the intensity is high, but there is a significant dip followed by subsequent rise in the OH* emission as the two waves begin to interact around $\alpha/2\pi = 0$. At approximately $\alpha/2\pi \geq 0.13$ the detonation wave is propagating unaffected by the CRWP and is recovering from the previous interaction in the cycle. Once the two waves begin to interact, the OH* signal begins to decrease and broaden out, ultimately reducing to an amount approximately one fifth of its original value before the interaction began. As the interaction continues, there is a sudden and sharp rise in OH* resulting in a maximum value located at approximately $(\theta, \alpha) = (0, -0.15)$ which is greater than what was originally seen before the interaction began. This spike quickly subsides and the detonation begins to recover as the process repeats itself. When the CRWP is weak or the interaction is negligible, then the dependence on α is reduced. In the limiting case where the secondary wave is not present, there is no variation in α. In the field around the main detonation wave it is also possible to see the trajectory of the CRWP travelling in the negative (θ, α) direction. While in the $\langle P(\theta = 0|\alpha)\rangle$ field the CRWP can be identified as a singular cohesive streak, in the OH* they appear as a multi-layered structure composed of a less reactive dark band (black dashed line in Fig. 2.23) bounded by two reactive brighter bands (red dash lines in Fig. 2.23). The two bright band trajectories are approximately outlined by the outermost red

dashed lines, with the less reactive band centered between them. The entire structure travels through the contour plot in the negative (θ, α) direction. In the wake of the detonation wave, in the region of $\theta/2\pi < -0.1$, the secondary wave structure is not as easily identified and the wave does not readily reappear until it is sufficiently past the detonation wake in the region of $\theta/2\pi > 0.25$. The continuous streak seen in $\langle P(\theta|\alpha)\rangle$ and $x-t$ diagrams suggests that the CRWP travels continuously, rather than being recreated after each interaction.

The multi-layered structure of the CRWP is likely responsible for the more complex behavior seen in the OH* emission when compared to the pressure distribution. As shown in Fig. 2.23, the CRWP is composed of two reacting layers separated by a non-reacting one. As the first reactive layer begins to interact with the detonation wave, OH* emission across the detonation wave begins to broaden out. When the non-reactive layer interacts with the detonation, it is responsible for the drastic reduction in OH* emission seen at the origin of the conditional phase plot of Fig. 2.23. This corresponds to a suppression of heat released at the wave. After the drastic reduction associated with the non-reactive layer, the second reactive layer arrives at and interacts with the detonation wave, and the OH* emission intensifies up to the maximum value observed around $\alpha/2\pi = -0.125$. Thus, it appears the interaction with the second reacting band may be responsible for the re-emergence of high OH* emission and ultimately the large OH* emission spike. If we draw an analogy to colliding normal shocks, we can hypothesize that if the secondary wave propagation induces an azimuthal flow, which will be counter to the detonation wave, it will effectively raise the relative speed (Mach number) of the main detonation wave, and therefore its properties, such as its pressure rise, as observed in the data. In addition, the fact that OH* emission is reduced at the interaction, may suggest that upon interaction the heat release region behind the shock wave ceases, leaving only a shock wave that is stronger by the interaction (higher pressure rise), but that continues to propagate through the interaction. Subsequently, past the immediate interaction process, OH* emission increases again, suggesting that conditions for heat release to occur are established again, for example by reaching a detonatable mixture under likely high pressure and temperature conditions.

We speculate that the mutli-layered structure of the CRWP is a consequence of local changes of fill gas composition (i.e., equivalence ratio) induced by differences in the response of the air inlet and fuel injector from the passage of the secondary wave and the pressure rise associated with it. Thus, the propagation of the secondary wave would leave in its wake a region where gas composition is disturbed, and specifically

the equivalence ratio would be axially stratified according to the relative response of the air and fuel streams. To evaluate this possibility, we have developed a model to estimate the response time of the air and fuel streams. Details of the model are outlined in section 2.3.4. Based on our injector response model, we estimate that for the AAI configuration, when the equivalence ratio is above 0.8 the fuel stream responds first, while for less than 0.8 the air stream responds first. Because secondary waves observed in the AAI configuration are strongest for richer conditions, the results of the injector response model suggests that the disturbed fill region in the wake of the secondary wave is fuel rich axially stratified. This stratification would then result in a reduction of chemical reaction, as suggested by the drop in OH* emission. It is worth noting that OH* emission is not eliminated completely, but it is severely weakened relative to the emission at the detonation throughout the rest of the cycle.

2.5 RDC Operation with Variable Inlet Area

2.5.1 Standard AAI Configuration

The mode and characteristics of operation of the system under both AAI-1 and AAI-2 configurations have been determined over a range of operating conditions. The operating mode, described as a function of global equivalence ratio and air mass flux (defined with respect to the detonation channel area), for each of the two cases are summarized in Figure 2.24. The AAI-1 configuration is able to achieve operation in detonation mode for a wide range of conditions – see Figure 2.24(a). On the contrary, as shown in Figure 2.24(b), the operational regime of AAI-2 is greatly reduced when compared to AAI-1 and tends to operate at lower equivalence ratio and higher mass flow rate conditions. This reduced range of operability is thought to be related to the response time of the air and fuel injectors.

The operation map of Figure 2.24 is recast in terms of $\dot{m}_a/A_{3.1,a}$ for both inlet configuration in Figure 2.25. In this form we observe that the two geometric configurations operate over approximately the same range of mass flux. The overlap in the two regions where detonation is observed suggests that there might be a minimum value of mass flux, defined relative to the injection throat, that is necessary for operation, rather than a minimum amount of mass flowing through the detonation channel. For this reason, and for the scaling of pressure which will be discussed next, operational maps will be shown with reference to $\dot{m}_a/A_{3.1,a}$ from now on, instead of purely mass flow rate $\dot{m}_a$.

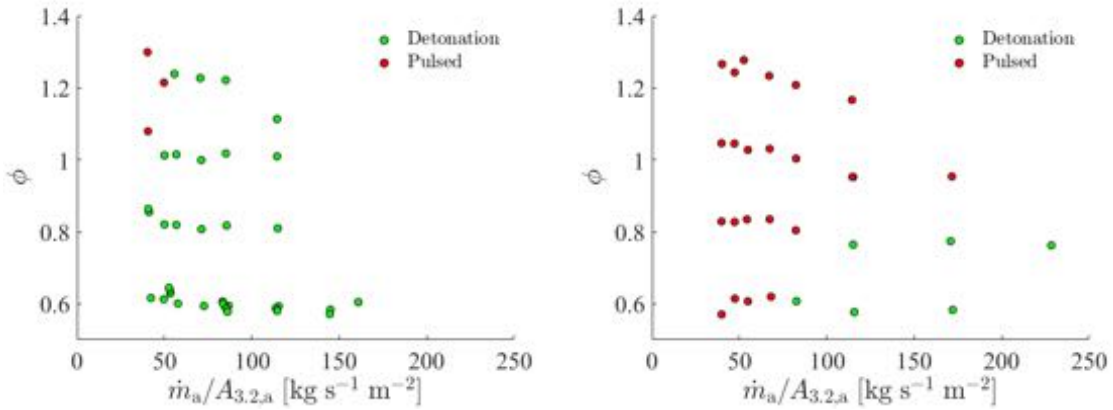

Figure 2.24: Operational maps for a) AAI-1 and b) AAI-2. Air mass flux is defined with respect to the detonation channel area $A_{3.2}$

The use of the mass flux evaluated at the throat of the air and fuel injectors is also able to correlate other quantities of operation that define the axial air inlet configuration. In particular, the plenum pressure (P_2) of the air and fuel streams, during engine operation, can be shown to follow similar trends when using the aforementioned mass flux scaling, as seen in Figure 2.26. Here the static plenum pressure that is measured is taken to be a stagnation pressure for the respective fuel and air streams, due to the low flow speeds in the plenum. The plenum pressures for the two injection schemes are approximately linear for their detonation operation regimes with respect to the mass fluxes at the throat, with the air stream showing some equivalence ratio dependence. The equivalence ratio dependence seen in the reacting portion of

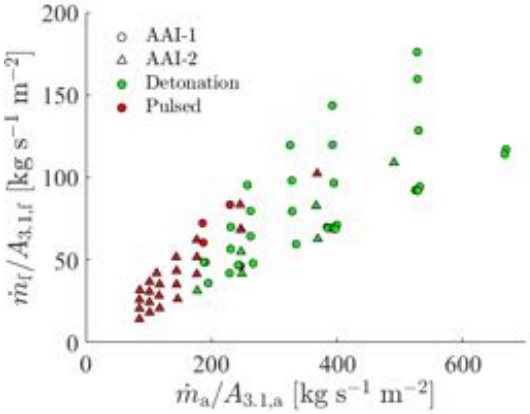

Figure 2.25: Mass flux for both air and fuel plotted against each other for both AAI-1 and AAI-2. Mass flux is defined with respect to air and fuel injection areas.

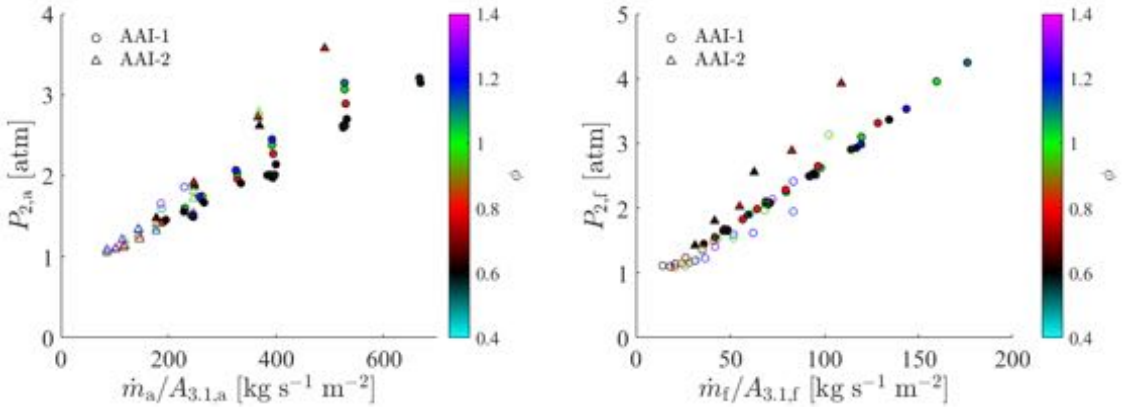

(a) (b)

Figure 2.26: a) Air plenum as a function of air mass flux through throat b) Fuel plenum pressures as a function of fuel mass flux through throat. Detonation operation conditions are shown as solid symbols.

our experiments for AAI-1 and to a lesser extent AAI-2, is likely caused by the following mechanism. The injectors for the fuel in AAI-1 are situated close to the exit of the air injector and are angled toward it, as a result the introduction of fuel into the channel poses a fluidic obstacle to the flow of air. This would result in greater air plenum pressures with increasing fuel flow rates, consistent with what is seen in practice. Richer conditions are seen to have higher air plenum pressures for these injectors. Despite complex dynamics occurring at the inlets, it is currently believed that the cause for the linear behavior of the mean pressures of the plenums for both fuel and air streams is that the injectors are partially choked during operation (see Section 2.3.1).

The detonation wave speeds seen in the two injectors have more complicated behavior than the plenum pressures, and cannot be readily reduced with the same mass flux scaling. Figure 2.27 shows the detonation wave speeds of the two injectors normalized by the ideal CJ detonation wave velocity as a function of mass flux through the air throat. For both injectors the wave speed has a dependence on both mass flow rate and equivalence ratio, though these are likely not the controlling factors to the wave speed behavior. In general, we see that the AAI-1 exhibits faster detonations for a given operation condition when compared to AAI-2. The AAI-1 injector has

wave speeds generally in the range of 75% to 82% of the ideal detonation velocity while the AAI-2 injector falls more in the range of 65% to 70%. It is not currently known what the driving force may be for the general reduction in wave speed seen between the two injection schemes.

2.5.2 Nominal EAAI Configuration

We presented the first operation maps and a selection of relevant performance metrics of the enhanced axial air inlet design with ambient temperature hydrogen-air mixtures in 2021 [9]. Actual design details and characteristics were withheld but a basic schematic indicating the flowpath was shown previously in Figure 2.2. This work included a limited summary of the design and an initial presentation of conventional metrics used to characterize operation such as observed wavespeed, pressure rise, and pressure ratio. Testing was conducted at three inlet area ratios (ARs), corresponding to the ratios of channel to throat area. Additional testing of varying channel/exhaust geometries with this inlet configuration has since been conducted, but all data presented in this work was with a constant area channel and no exhaust restriction. This work also outlined the development of several new performance measures, including that of effective inlet blockage that was explored in detail previously in subsection 2.3.1.

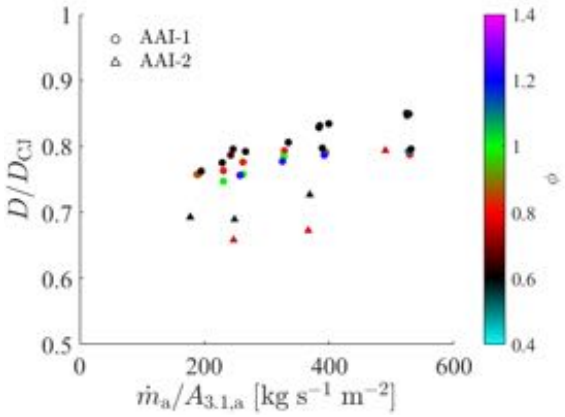

Figure 2.27: Detonation wave speed as normalized by the CJ wave speed is greater for AAI-1 for similar operating conditions when compared to AAI-2

In addition to the effective blockage metric, an additional performance measure that was developed and presented was that of static pressure drop from the plenum to channel exit under non-reacting (and subsequently, reacting) flow conditions. This metric was developed to indicate the aerodynamic similarity feature of the enhanced axial air inlet design, in that the static pressure ratio of the pressure near the channel exit to that of the plenum for a given inlet mass flux is invariant. This can be seen in the collapsing of the independent curves of Figure 2.28 when compared with air

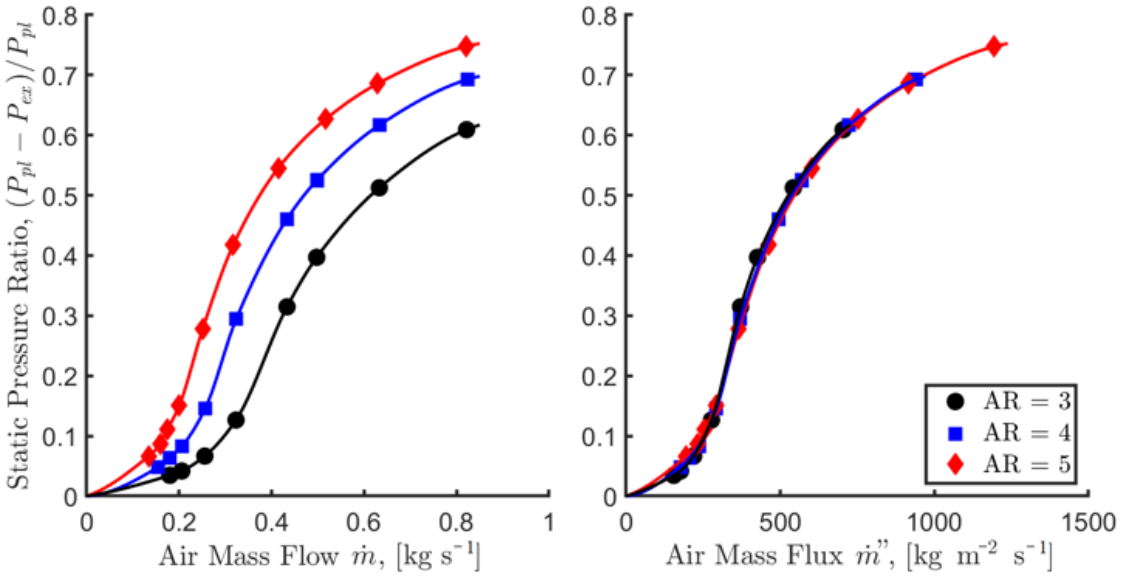

Figure 2.28: Static Pressure Ratio as function of a) $\dot{m}$ and b) $\dot{m}''$.

mass flow (a) to a singular relationship when compared with inlet air mass flux (b). This feature was also used to characterize the Mach number at the inlet as shown in Figure 2.30, demonstrating that all inlet configurations tested choke at an inlet air mass flux of approximately 290 kgm^-2s^-1.

The aerodynamic similarity feature of this configuration inspired the effort to develop the previously summarized effective blockage fraction (B) metric to characterize the inlet during operation and quantify the effect of the detonation wave(s) on the plenum and inlet flowfield. As the inlet was hypothesized to possess similar flow characteristics in the unblocked region as to that of the entire inlet when completely unblocked, this relationship thus results in an effective blockage fraction of the total area of the inlet that would result in a similar plenum pressurization. Based upon the calculated values of B found through the methods outlined above, an effective air mass flux in the unblocked portion of the inlet was found for all test cases. This metric showed that all successful test cases that indicated detonative operation were choked in the unblocked region of the inlet as shown in Figure 2.29. This was found to be a necessary but not sufficient condition for operation, as there were cases that indicated a choked inlet but did not result in successful operation.

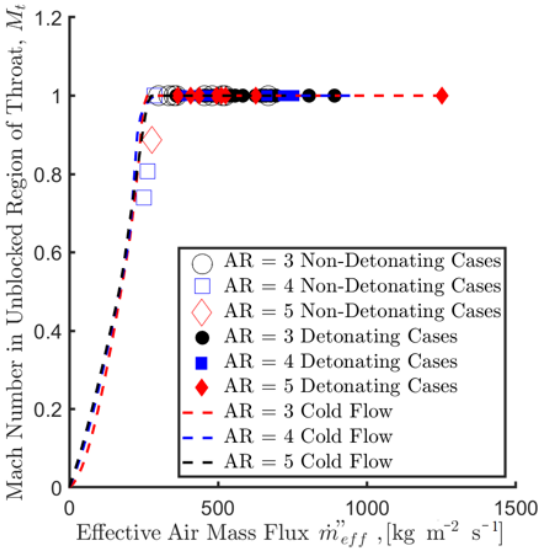

Figure 2.29: Mach Number at air inlet in the unblocked region (M_t).

2.5.3 Wide Channel EAAI Configuration

For all RDC configurations thus far tested in our facility the channel geometry has remained relatively invariant, in that the channel width has always remained 7.6 mm with an outer channel diameter of 153.9 mm and an inner channel diameter of 138.7 mm. Initial testing of the EAAI with a "wide" channel configuration with hydrogen-air mixtures was recently conducted. All reactants were introduced at am-

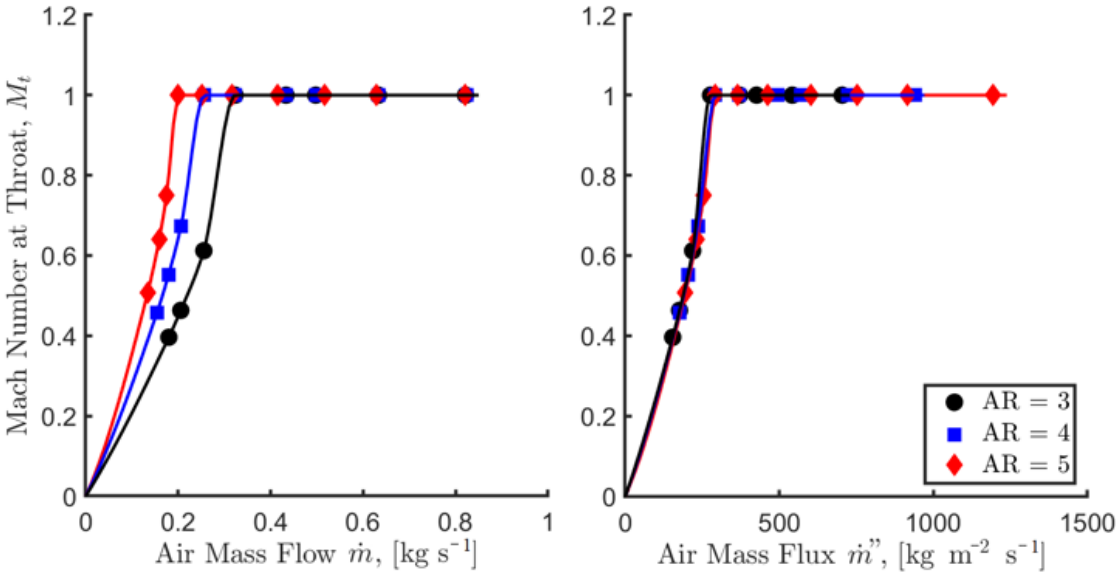

Figure 2.30: Mach Number at air inlet (M_t) as function of a) $\dot{m}$ and b) $\dot{m}''$.

bient temperatures of approximately 290 K. This configuration maintains the inlet and exhaust areas of the previously tested "narrow" configuration. The constant channel width in the nominal configuration is 7.6 mm, while the wide channel configuration possesses a smooth contour on the inner channel wall from the air inlet to a maximum channel width of 15.2 mm. The exhaust area was held constant between the two configurations with the incorporation of a converging exhaust restriction to the nominal channel width of 7.6 mm, which results in an effective 47% area reduction of the exhaust relative to the widest portion of the channel at the exhaust plane. Schematic views of the nominal configuration was previously shown in Figure 2.2, with a similar profile for the wide channel configuration shown in Figure 2.31. Only the inner wall contour from Station 3.2 to 8 was varied in this study, the inlet (Station 2 to 3.2) configuration was unmodified.

We previously demonstrated aerodynamic similarity of the EAAI inlet design by comparing the static pressure loss from the plenum (P_{pl}) to the furthest downstream Capillary Tube Averaged Pressure (CTAP) measurement within the channel (P_{ch}) during non-reacting flows. This similarity was found to remain when comparing the nominal and wide channel configurations as can be seen in Figure 2.32. The static pressure ratio was found be solely dependent upon air mass flux at the inlet despite the change in downstream channel geometry. Testing was conducted at the same three inlet setpoints (ARs) as with the nominal channel configuration, which in order to maintain similarity in nomenclature in the wide channel configuration correspond to the ratios of exhaust (equivalent to nominal channel area) to inlet throat area. This ensures that a given AR in either channel configuration represents the same inlet setpoint and inlet area.

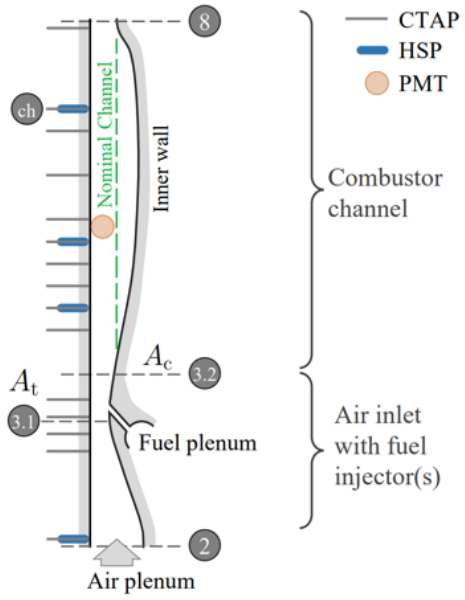

Figure 2.31: Diagram of enhanced axial air inlet configuration with wide channel.

The wide channel configuration was found to exhibit similar operating characteristics to that of the nominal channel. For similar inlet conditions the wider channel generally exhibited a slower wavespeed when compared to tests conducted with the nominal

channel width. However, the wider channel generally resulted in similar values of effective blockage fraction when compared to similar tests conducted in the nominal channel configuration. The trends in both of these parameters for a selection of comparable test cases can be observed in Figure 2.33, which includes successful tests conducted across a range of inlet air mass fluxes for equivalence ratios of 0.6±0.1.

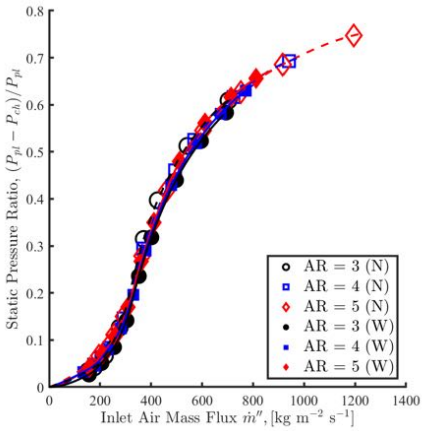

Figure 2.32: Static pressure ratio between channel/plenum under non-reacting flow conditions for wide (W) and nominal (N) channel configurations

Testing conducted in the wide channel configuration also included the first use of an extreme temperature Type-B thermocouple installed in a flush mount configuration on the outer wall of the channel at Station 8 of Figures 2.1 & 2.2. This bare-wire thermocouple was installed through a ceramic feedthrough with the bead flush with the outer wall. Initial results from this measurement are shown in Figure 2.34. Peak exhaust temperatures approaching 1500 K were found, with most test cases falling between 1000-1400 K. Additional thermocouples have been procured, similar sensor mounts have been fabricated, and testing is ongoing with four of these sensors installed at varying axial locations. Testing is also ongoing with the previously summarized thrust stand to determine if these measures of T_7 and/or T_8 can be leveraged as an analog for net thrust and overall pressure gain.

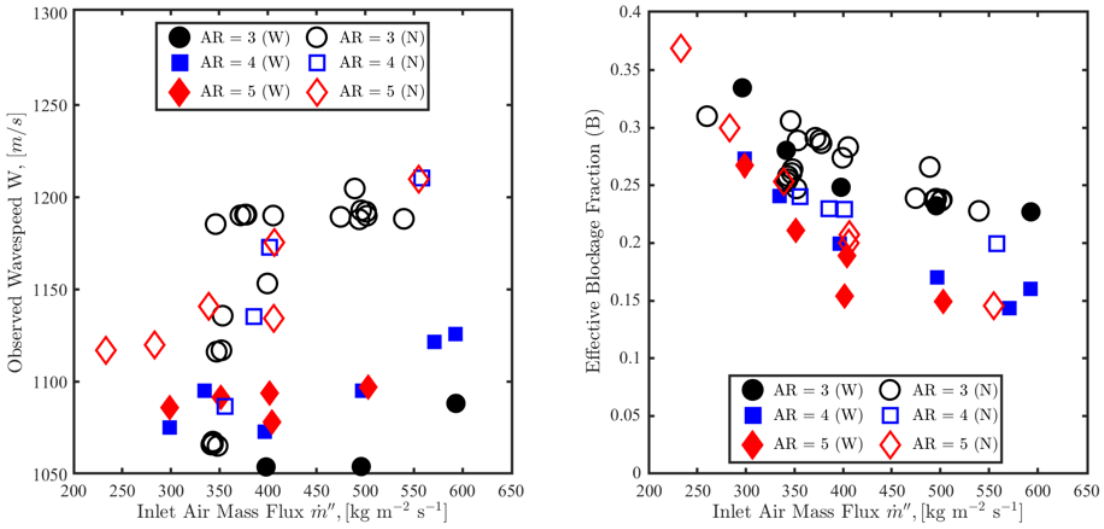

(a) (b)

Figure 2.33: Select performance metrics in wide (W) and nominal (N) channel configurations for $\phi = 0.6 \pm 0.1$ test cases, a) observed wavespeed and b) effective blockage, B.

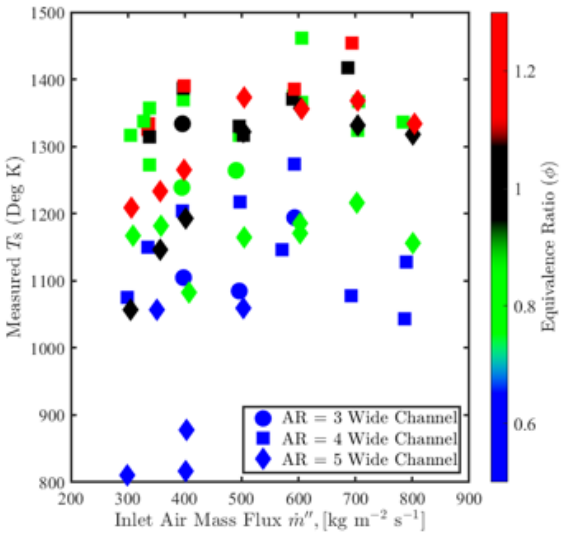

Figure 2.34: Exhaust temperature (T_8) measured by flush mount Type-B thermocouple in wide channel configuration

2.6 RDC with CO_2 Dilution

A diluent in a detonative mixture interferes with chemical kinetics thereby changing the detonative properties, structure, and induction length. This results in an increased detonation cell width. Specifically, CO_2 has been found to be an effective inhibitor by dramatically decreasing the number of detonable mixture conditions, though its effectiveness was found to decrease with temperature [13]. As a result of CO_2 addition to hydrogen/air detonations near stoichiometric conditions, the resulting cell size is found to increase by a factor of almost 3 with 10% CO_2 dilution [14]. While introducing an inert or diluent gas to the fuel/air mixture would not be done in a practical application of the combustor, it does allow for the studying of mixture vitiation effects on the operation and performance of RDEs, which is a process that likely occurs in RDCs [15]. Since CO_2 acts as an inhibitor, its use as diluent allows for studying the limits of operation by systematically increasing the detonation cell width. There are also fuel gas mixtures that contain inert gas or gases with low energy content that would act as diluents, such as CO_2 and CO in syngas, which necessitates understanding the impact these species have on RDCs.

χ_{CO_2}	$\dot{m}/A_{th}$ kg s^{-1}m^{-2}	ϕ
0.05	240	0.6-1.4
0.05-0.13	240	0.9
0.05	550	0.6

Table 2.2: Summary of the operating conditions with stable detonation that are analyzed in this work.

2.6.1 Operating Conditions with CO_2

This study focused on a small set of combinations of air mass flux and equivalence ratio while also varying the amount of CO_2 added. The amount of air and fuel introduced in the system were maintained the same as for cases without CO_2, and were determined solely on air mass flux and equivalence ratio. This was done to maintain the same amount of energy release when compared to previously studied cases. For a fixed air mass flux (here defined in terms of the air inlet throat area) of 240 kg s^{-1}m^{-2}, the equivalence ratio was fixed at about 0.9 and χ_{CO_2} was varied. Then, at the same air mass flux, the χ_{CO_2} was fixed at about 0.05 and the equivalence ratio was varied. Finally, a few combinations of equivalence ratio and higher air mass fluxes were tested with a fixed $\chi_{CO_2} \approx 0.05$. The conditions are shown in Figure 2.35, where all the conditions have been run multiple times to collect a sufficient number of single-shot CO_2 thermal emission images to analyze the overall detonation cycle. All of the fuel/air mixtures tested operate with a single, steady detonation wave without the presence of CO_2. However, it was observed that at the chosen air mass flux and equivalence ratio, once χ_{CO_2} exceeded 0.1, no form of detonation could be achieved and the engine would operate in deflagration instead. Even when the combustor was initially ignited at an operating condition with no CO_2 addition, allowed to stabilize, and then transitioned χ_{CO_2} was added to the streams with a mole fraction greater than 0.1, the detonation was not sustained. A pair of waves rotating counter to each other (referred to as slapping mode operation) appeared for most of the conditions with $\chi_{CO_2} \approx 0.05$ and air mass fluxes greater above 240 kg s^{-1}m^{-2} regardless of equivalence ratio. The exception is the case at 550 kg s^{-1}m^{-2} with an equivalence ratio of 0.6. This case was tested multiple times to ensure repeatability, with each test resulting in a stable detonation. In this work, we will focus on the stable detonation cases since these can be more readily compared to their non-diluted counterparts. These cases are summarized in Table 2.2 for conciseness.

2.6.2 Changes in Non-Ideal Behavior Caused by Diluent

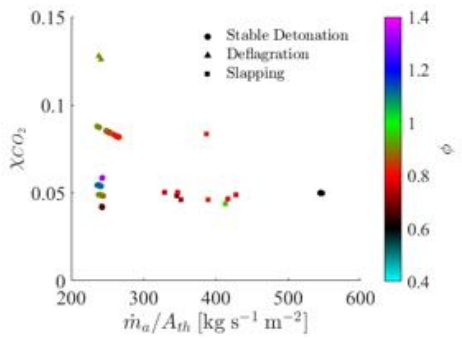

Figure 2.35: Operating conditions tested in this work. Stable detonation refers to steady, single wave operation and slapping refers to two counter-rotating detonation waves.

Using our previously developed diagnostics, we have evaluated the non-ideal behavior for all the conditions tested with CO_2. From this, we measured changes in both the secondary combustion in the detonation cycle and the secondary waves present within the system with the addition of CO_2. We employed CWA on the cases with added CO_2 and compared the results to non-diluted cases. Example of the temporal variation of the properties of the three different waves typically observed in this geometry are shown in Figure 2.36 for increasing amount of CO_2 addition. The cases shown are taken for operating conditions with air mass flux of 240 $\mathrm{kg\,s^{-1}m^{-2}}$ and equivalence ratio of 0.9. Attention should be drawn to the counter-rotating slow wave pair (diamond symbols) propagating at about 0.6 of the CJ speed for the nominal operating frequency in the nominal case in Figure 2.36(a). Considering the test case with the smallest amount of CO_2 added ($\chi_{CO_2} \approx 0.05$), it can be seen that the counter-rotating slow wave pair (diamonds) is practically eliminated. Interestingly, repeated testing at the same condition resulted in a small percentage of runs (less than 10% of runs) having a more observable counter-rotating wave pair, which is shown in Figure 2.36(c). Despite its existence, the secondary wave has an order of magnitude lower wave strength than the nominal (no CO_2 addition) condition. The comparison in secondary wave strengths with the inclusion of CO_2 is displayed in Figure 2.37. While for some instances, the strength of the secondary wave pair is comparable to that of the case without CO_2, on average there is a 1-3 order of magnitude drop with the addition of CO_2. Why the secondary waves manifested more prominently occasionally is currently unknown. Across all the conditions tested here, similar results are achieved where the secondary waves are diminished greatly, generally to the point of extinction. The presence of the inert CO_2 appears to either disrupt the mechanism for establishing the secondary wave system or the mechanism that supports the secondary waves that might be created. At this time, we cannot conclude which of these is the case and would require

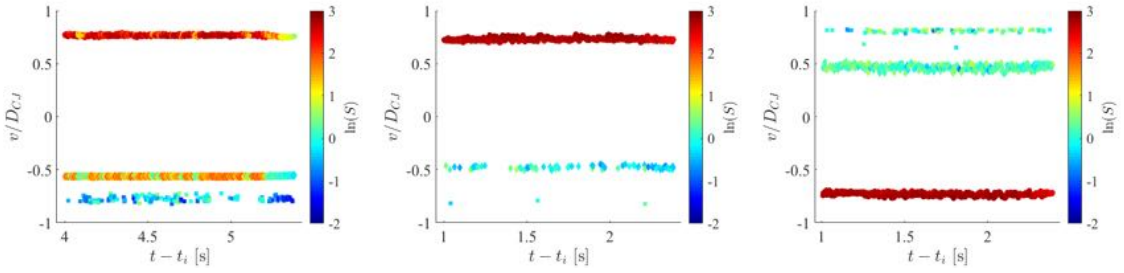

(a) (b) (c)

Figure 2.36: Time-history evolution of wave properties (speed, direction and strength) with a) no CO_2 addition; b) 5% CO_2; and c) 10% CO_2. Operating conditions: air mass flux 240 $\mathrm{kg\,s^{-1}m^{-2}}$ and equivalence ratio of 0.9. Symbols: • – primary detonation wave; ♦ – pair of counter rotating slow waves; and ■ – single counter rotating fast wave.

further investigation.

To evaluate the presence and strength of secondary combustion events within the channel, the OH* chemiluminescence PMT measurements are phase averaged following the procedure detailed in Feleo *et al.* [3]. This provides a phase-average representation of the combustion processes observed across the average cycle at the measurement point. We then directly compare the results for the same operating condition with varying amounts of CO_2, which are shown in Figure 2.39. Two cases are shown here, with Figure 2.39(a) having $\dot{m}/A_{th} = 240\,\mathrm{kg\,s^{-1}m^{-2}}$ and $\phi = 0.9$, while Figure 2.39(b) $\dot{m}/A_{th} = 540\,\mathrm{kg\,s^{-1}m^{-2}}$ and $\phi = 0.8$. The overall magnitude of the signal reported here for the nominal condition is lower than previous measurements [3] because in this study OH* chemiluminescence emission is collected from the window on the inner-body, which has a smaller collection volume because of the smaller window aperture (12.7 mm compared to 25.4 mm). However, this does not affect the trends in detonation properties observed in the previous study. There are significant variations in the heat release distribution due to the presence of CO_2. First, from both of the air mass flux cases, when $\chi_{CO_2} \approx 0.05$, there is an overall decrease in the observed OH* signal. This could be a result of a lower overall temperature from the added thermal mass or the detonation structure changing such that the height of the detonation does not fully reach the probe volume. However, the signal collected when $\chi_{CO_2} \approx 0.09$ is comparable to the signal collected without CO_2 despite lower

temperatures being expected. The amount of parasitic combustion observed at the lower air mass flux case is about the same regardless of the amount of CO_2, which is lower than the nominal condition. Examining the higher air mass flux case in Figure 2.39(b) shows a different result. Here, the parasitic combustion grows in magnitude compared to the nominal case. Furthermore, the shape changes such that commensal combustion cannot be readily identified (based on our prior definition [3]) and the onset of parasitic combustion starts earlier in the detonation cycle.

Additionally, the breakdown of regions of heat release associated with parasitic combustion, detonation wave, and commensal combustion was performed, where OH* chemiluminescence is used to qualitatively mark heat release distribution. Figure 2.38 shows the relative amount of parasitic heat release observed for all the conditions tested. In a previous study [3], we found that the relative amount of parasitic combustion was near constant at about 0.18 for the nominal conditions without CO_2, which is represented in Figure 2.38 with the dashed black line. Here it is observed that when there is $\chi_{CO_2} \approx 0.05$, the relative amount of parasitic combustion increases slightly at the lower air mass flux case and greatly increases at the higher air mass flux case. On the other hand, on average when $\chi_{CO_2} \approx 0.09$, the relative parasitic combustion is slightly lower than the nominal case. This can also be seen in the phase averaged profiles discussed previously. It should be noted that unlike the measurements taken without CO_2 which were highly repeatable, there was significant variability for the runs that included CO_2. This can be readily seen in the spread of data for similar operating conditions. The inert CO_2 clearly disrupts the combustion events within the channel, though the exact mechanism by which it disrupts the combustion cannot be determined as of yet.

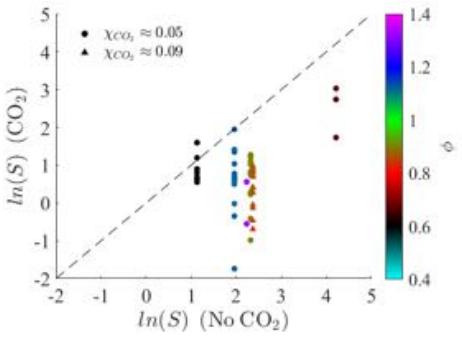

Figure 2.37: Diluting with CO_2 reduces wave strength of secondary waves by an order of magnitude or greater.

2.6.3 Changes in Detonation Properties Caused by Diluent

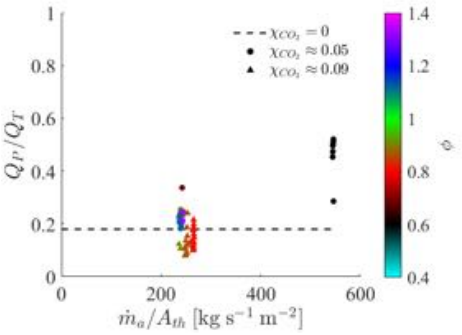

Figure 2.38: Diluting with CO_2 diminishes relative amount of parasitic combustion observed for $\chi_{CO_2} \approx 0.09$, though it seems to increase when $\chi_{CO_2} \approx 0.05$.

Changes in non-ideal combustion events have been previously observed to affect the overall detonation properties [3]; thus, it is expected that detonation speed and pressure ratio would change from the non-diluted cases based upon the observations from the previous section. To draw comparisons with previous testing, all cases presented in this works were compared to the run with the closest air mass flow rate and equivalence ratio combination. It was found that the detonation speed normalized by the corresponding CJ value decreased with an increasing amount of CO_2 in the system as seen in Figure 2.40(a) in which the $\chi_{CO_2} \approx 0.05$ runs (circles) are significantly higher than the runs where $\chi_{CO_2} \approx 0.09$ (triangles). This decrease in normalized speed is much more prominent at equivalence ratios that are at or below stoichiometric conditions. At fuel rich conditions the normalized velocities for $\chi_{CO_2} \approx 0.05$ cases become nearly equivalent to the speeds achieved without the presence of CO_2. It is probable that by increasing the χ_{CO_2} above 0.1 as was attempted in testing, the resulting wave speed would have been too slow to sustain a detonation, though this cannot be confirmed at this time. In general, the overall decrease in wave speeds can be attributed to some amount of the heat supporting the detonation wave being absorbed by the inert CO_2 as was seen in the phase averaged OH* profiles.

Similarly, the change in pressure ratio across the detonations can be evaluated. The pressure ratio here is measured as the peak to trough ratio in each individual cycle in the high-speed pressure measurement and then averaged across all the cycles. This cycle-to-cycle averaged pressure ratio was normalized by the corresponding CJ value, and it is shown in Figure 2.40(b). Despite the drop in normalized detonation speed previously discussed, a slight increase can be observed with the addition of CO_2 for nearly all the cases considered in this work when compared to similar cases without CO_2. While the pressure ratios are still far from being unity, on average, the pressure ratio increased by 5-10%. Again, fuel rich conditions (blue circles) more closely match their non-diluted counterpart and as equivalence ratio decreases, the greater the change in the measured pressure ratio. The disruption to the dynamics caused by the presence of the diluent is such that a net-positive in pressure ratio is gained

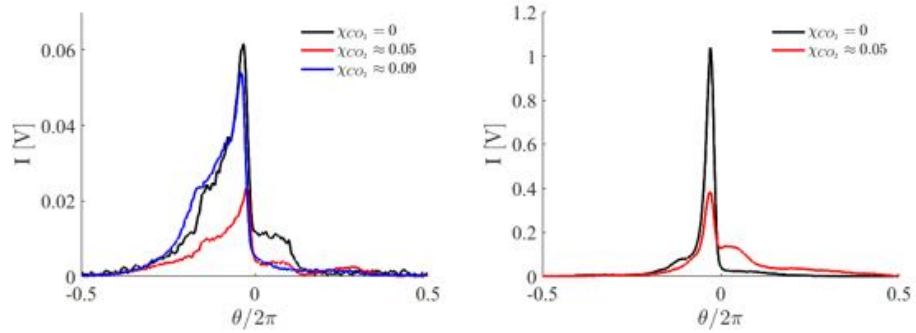

(a) (b)

Figure 2.39: Changes to heat release distribution caused by addition of CO_2 for a) $\dot{m}/A_{th} = 240\text{kg}\,\text{s}^{-1}\text{m}^{-2}$ and $\phi = 0.9$ b) $\dot{m}/A_{th} = 540\text{kg}\,\text{s}^{-1}\text{m}^{-2}$ and $\phi = 0.8$

despite the expected chemistry being detrimental as was observed in the modeling of the CJ conditions discussed previously. These cases show how the properties of the detonation wave cycle ultimately depend on a combination of the chemistry of the mixture, thermal effects, and properties of secondary phenomena such as deflagration and additional dynamics.

2.7 RDC Operation with Elevated Inlet Temperatures

2.7.1 Operating Conditions and Operating Mode

This study solely considered H_2/air operation. Two different air mass fluxes ($\dot{m}_a/A_{th}$) were considered, 452 and 552 $\text{kg}\,\text{s}^{-1}\,\text{m}^{-2}$. The lower flux condition was tested at an equivalence ratio of 0.5, while the greater mass flux condition was tested at 0.6 and 1. These conditions were chosen because the corresponding operating conditions at ambient inlet temperature (near 295 K) exhibited stable operation in previous tests. At each of these conditions, repeated testing with varying air inlet temperature T_2 values (up to about 480 K) was performed. The number of waves observed at operation at these conditions with increasing inlet temperature is shown in Figure 2.41. (A small offset from an integer number was applied to avoid overlapping symbols.)

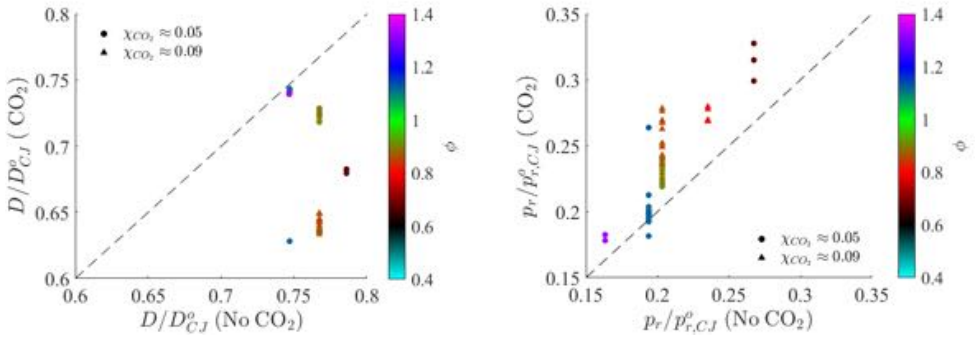

(a) (b)

Figure 2.40: a) Normalized detonation velocity decreases with CO_2 dilution; and b) Pressure ratio increases with CO_2 dilution. Values are compared to runs with the same air mass flow rate and equivalence without the added CO_2.

Here classification of one wave operation is used to indicate operation with a single, stable detonation wave; whereas classification of two wave operation refers to operation with two counter-propagating detonation waves, resulting in a slapping mode of operation. For the fuel lean conditions, operation with a single stable detonation wave transitioned to operation with two counter-rotating waves. This occurred at an inlet temperature of 320 K for the lower flux and about 360 K for the higher flux. This is of concern since slapping wave operation is typically seen as a less stable and more chaotic operation that could impact the integration of the RDC with turbomachinery in a practical system. The stoichiometric condition did not display this transition within the range of inlet temperature tested. This result may suggest that, for this configuration and air mass flux, there is an equivalence ratio dependence on the robustness of operating conditions to increasing inlet temperature.

2.7.2 Temperature Impact on Detonation Properties

In addition to the observed operational changes, metrics such as the detonation wave speed (D) and pressure ratio (p_r) can be used to study the changes in the flowfield induced by the higher inlet temperature. Figures 2.42 and 2.43 show the changes in detonation wave speed and pressure ratio across the wave both measured by a Kulite within the detonation channel. Quantities have been normalized by their ideal CJ

values evaluated for a perfectly mixed mixture at the global equivalence ratio and the measured temperature of the gaseous mixture entering the combustor (indicated with subscript 'CJ'). For the stoichiometric condition tested there was little variability in the normalized wave speed, with the 50 m/s decrease in wave-speed observed at 420 K being balanced by the decrease in the CJ wave speed with the higher T_2. Again, the stoichiometric condition seems resistant to change in the dynamics induced by the changes in T_2. However, for the fuel lean case, significant variations in both absolute and normalized wave speeds are observed. The drop in wave speed at $T_2 =$ 360 K can be attributed to the increase in the number of waves (i.e. from one wave to two counter-rotating waves). This is consistent with past observations [16]. For temperatures less than 335 K and greater than 360 K, an increase in temperature does not appear to cause a significant change in the detonation wave speed and normalized wave speed since the values are nearly constant similarly to what is seen for the stoichiometric case. Interestingly, for the fuel lean case, at about $T_2 = 340$ K, which is still a case with a single detonation wave operation, the observed wave speed has decreased by 100 m/s. This puts the speed about halfway between the speeds seen by a single wave and two waves operation. It is hypothesized that as the detonation slows down, thereby increasing the cycle time and fill height, a second detonation wave can be sustained with the increased availability of the incoming fresh reactants.

Unlike the wave speed, the pressure ratio exhibits a clear dependence on the inlet temperature, as shown in Figure 2.43. For both equivalence ratios, the non-normalized pressure ratio across the detonation wave decreased with the increasing temperature. There is an exception for the $\phi = 0.6$ case where the pressure ratio jumps at $T_2 =$ 360 K, but this may be explained by a switch to slapping waves operation. The interaction between the counter-propagating waves would likely result in a higher pressure rise than would occur for an individual wave – this is similar to what was observed with the interaction between the detonation wave and a secondary wave [2]. Even with the decrease in observed pressure ratio, the normalized pressure ratio increasing linearly with inlet temperature. Normalization was conducted using the pressure ratio of an ideal detonation wave at the nominal conditions of the mixture. The increase in normalized pressure ratio then occurs because the decrease with increasing temperature of the pressure ratio for an ideal CJ detonation wave is greater than the decrease in pressure ratio observed experimentally in the RDC. This increase in normalized pressure ratio is up to 25% of the pressure ratio at the nominal, room temperature conditions going from 0.26 to 0.34 the CJ pressure ratio for $\phi = 0.6$.

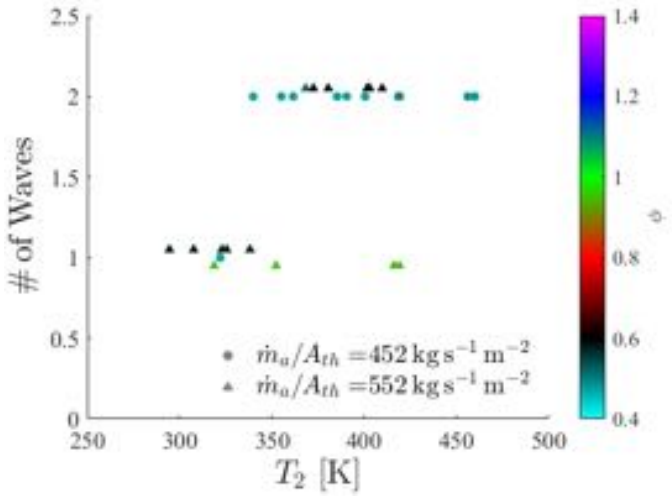

Figure 2.41: Number of waves as a function of inlet temperature for fixed $\dot{m}/A_{th} = 552\,\mathrm{kg\,s^{-1}\,m^{-2}}$ at $\phi = 0.6$ and $\phi = 1$. For the fuel lean case, operation transitions from single wave to two counter-rotating waves at $T_2 = 360$ K.

Therefore, in this regard, the detonation wave grows stronger (relatively) or more ideal in having a higher normalized pressure ratio for the same normalized wave speed, though this may come at the cost of having a less stable operating condition associated with the slapping waves mode.

2.7.3 Changes in Wave Dynamics

To track the change in wave dynamics as temperature varies, we examine the frequency content of high-speed, wall-flush pressure measurements in the channel. Select spectra of pressure measurements for operation at different T_2 values and $\dot{m}_a/A_{th} = 552\,\mathrm{kg\,s^{-1}\,m^{-2}}$ and $\phi = 0.6$ are shown in Figure 2.44. The selected inlet temperatures shown in Figure 2.44 were chosen to represent the frequency content at low (single, stable detonation wave) and elevated (slapping wave pair) inlet temperature. The detonation frequency is the tone at a frequency of $0.72 f_{CJ}$ for both $T_2 = 295$ K and $T_2 = 326$ K (red and blue spectra, respectively) cases, which both have a single stable detonation wave. The peak of the mode near $0.72 f_{CJ}$ appears to be splitting, though this could also be caused by noise. Although the wave speed decreases with increas-

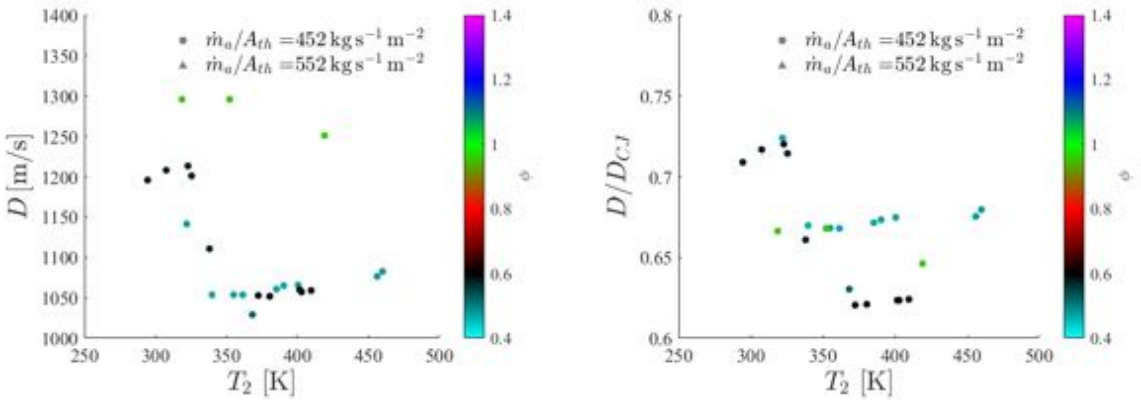

(a) (b)

Figure 2.42: Variation of a) dimensional and b) normalized detonation wave speed with inlet temperature. Both quantities show little to no dependence on inlet temperature except for when transitioning to a different operating mode for $\phi = 0.6$ (i.e. from one wave to two waves) at $T_2 = 340 - 360K$.

ing inlet temperature (discussed further below), when $T_2 = 338$ K (black spectrum) a single detonation wave is present with a frequency of $0.66 f_{CJ}$. For the condition shown in Figure 2.44, operation changes from a single wave to slapping waves in the range of 340 K $< T_2 \leq$ 370 K. Finally, the spectra for the $T_2 = 368$ K and $T_2 = 410$ K cases (pink and green spectra, respectively), have two waves centered at $0.62 f_{CJ}$. This spectrum has broader peaks than the other spectra, which is due to the two waves having slightly different velocities than one another. Before and after the transition, the observed dynamics do not vary much. This can be seen by comparing the $T_2 = 295$ K case to the $T_2 = 325$ K case for the pre-transition dynamics and the $T_2 = 368$ K case to the $T_2 = 410$ K case for the post-transition dynamics. The results of this condition are consistent with those observed in the other fuel case.

The cause of the transition to operation with two slapping detonation waves is still unknown. One possibility is that the second detonation wave arises from a re-enforcing of a pre-existing, weaker secondary wave that co-exists with the single wave at lower inlet temperature, while another possibility, is that the second detonation forms as a new wave system after a threshold temperature is exceeded for a given fuel/oxidizer mixture. To evaluate the former, we seek to determine if a secondary

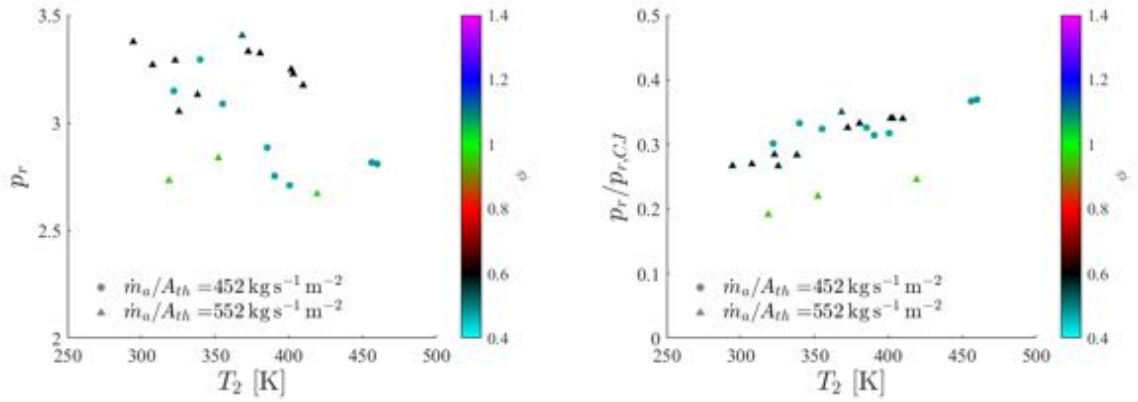

(a) (b)

Figure 2.43: a) Detonation pressure ratio decreases with increasing T_2, with the step-rise at the $\phi = 0.6$ case occurring due to switching to slapping operation. b) Normalized detonation pressure ratio increases nearly linearly with T_2 irrespective to different operating conditions or equivalence ratios.

wave system exists in addition to the single detonation wave at lower temperatures. Typically a secondary wave would have a distinct frequency from the detonation, allowing for the waves to be observable in the spectra. Examining the spectrum for the $T_2 = 326\,\mathrm{K}$ case in Figure 2.44, there are no distinct tones other than the detonation and its harmonics. This suggests that a secondary wave system cannot be supported at this condition. Similarly, despite the single detonation wave being slower (thereby weaker) at $T_2 = 338\,\mathrm{K}$, there is again a lack of distinct spectral content other than the detonation wave that would indicate additional waves in the system. It can be postulated that at these lower temperature conditions, that a secondary wave system attempts to establish during the ignition sequence, but is eventually consumed by the detonation if the detonation is sufficiently strong (fast). This could be an explanation (which cannot be evaluated at this time) for the lack of observable secondary waves at lower inlet temperatures. Additionally, this hypothesis could be extended that the by increasing temperature, the perturbations that would normally be consumed by the detonation have a change to grow strong and establish itself as another wave in the system. Regardless, these results point to the second detonation wave being an entirely new wave system created instead of an augmentation of observed pre-existing

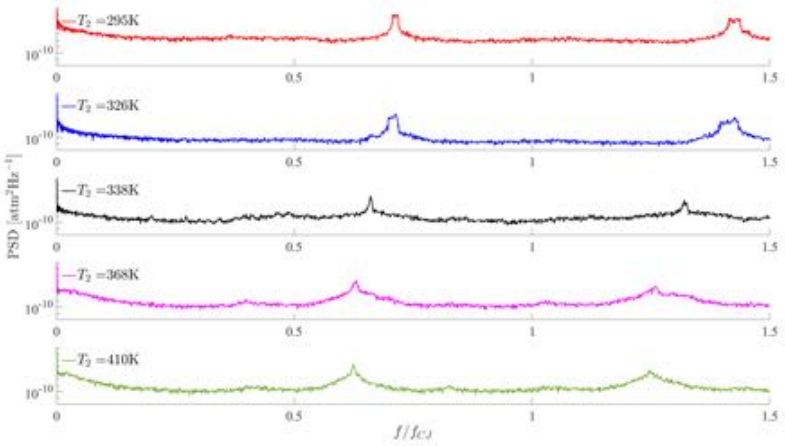

Figure 2.44: Spectrum of high-speed pressure for different T_2 at $\dot{m}_a/A_{th} = 552\,\mathrm{kg\,s^{-1}\,m^{-2}}$ and $\phi = 0.6$. Cases with $T_2 \leq 340$ K have a single detonation wave, while cases with $T_2 \geq 370$ K have two slapping waves.

secondary waves, with a currently unknown mechanism that leads to its creation.

The existence and strength of the second detonation wave can be further explored by applying the CWA method. Because of the classification currently implemented in CWA, slapping pair operation is treated as the combination of a primary detonation wave and a counter-rotating fast wave of similar strength and speed. We define the wave strength (S) from the spectral power of the tone of a wave system and its associated harmonics [2]. We evaluate the relative strength between the two detonation waves by taking the ratio between the strength of the secondary detonation wave (S^-_{Det}) and the strength of the primary detonation (S^+_{Det}). The label of "primary detonation" is given for the wave that is observed to travel at the slightly higher velocity and with larger wave strength. The ratio of wave strengths as a func-

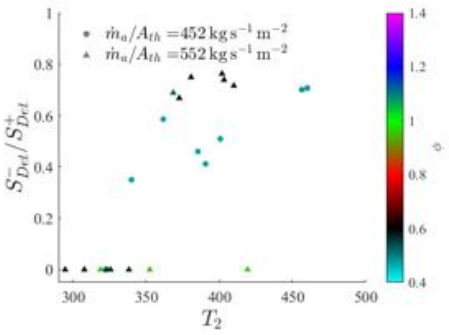

Figure 2.45: Ratio of second detonation wave strength to primary detonation wave. Second wave is not detected prior to the operation mode change.

tion of T_2 for the conditions tested is shown in Figure 2.45. A value of 0 here indicates that a second wave (detonation or some other form of secondary wave) is not observed at that condition. For the stoichiometric condition, a second wave of any form is not observed within the range of temperatures tested. For the fuel lean conditions, a non-zero S_{Det}^{-} is first observed once the operational mode changes above a threshold temperature. This, again demonstrates that the second wave arises as a completely new wave system instead of augmentation of a pre-existing, weaker secondary wave system, but rather a new wave system once certain (unknown) conditions are met. Once the second wave is observable, the ratio of wave strengths grows closer to unity with increasing T_2. This suggests that the second wave grows in strength until the two waves are nearly identical in speed and strength. We currently do not know if the condition of equal strength and speed waves is maintained as temperature is increased further.

2.8 Thrust Measurements

2.8.1 Standard AAI with No Exhaust Restriction

The first tests conducted with the thrust stand were of the standard AAI-1 inlet configuration with the constant area channel with no exhaust restriction. All tests during this sequence were conducted with hydrogen/air mixtures introduced at ambient temperature. Initial results and an outline of the methodology used to generate corrected net thrust values was summarized in a standalone work [**?**]. Due to the coupling of the RDC with the facility exhaust system, multiple corrections were utilized to arrive at an overall net thrust for each test case. This included accounting for momentum introduced to the control volume through the axial fuel feedlines, pressure variations acting on the bluff body exhaust cap, and pressure variations acting on the outer RDC exhaust flange between the detonation channel and the seal shown previously in Figures 2.4 & 2.5.

Results from this initial test sequence are shown in Figure 2.46. Consistent results were found in that net thrust was generally found to increase with increasing $\dot{m}''$ for a given ϕ and with increasing ϕ for a given inlent $\dot{m}''$.

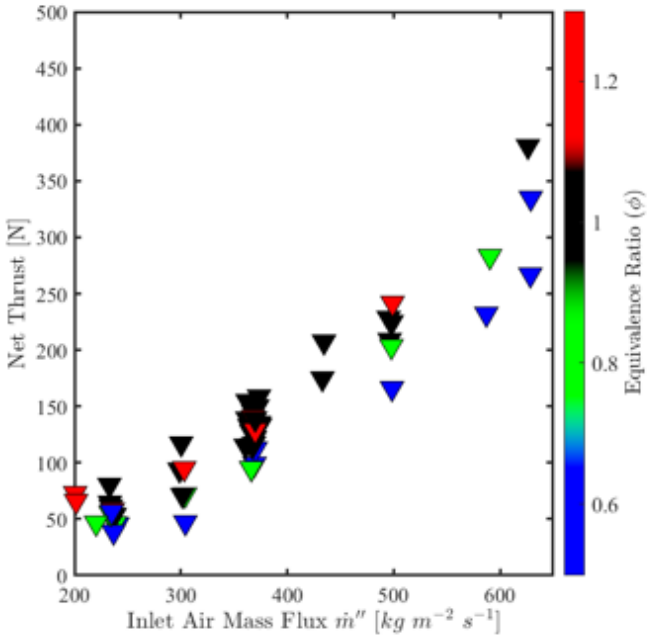

Figure 2.46: Net thrust, standard AAI with no exhaust restriction.

2.9 Operation with Gaseous Hydrocarbon Fuels

2.9.1 Standard AAI Attempts

2.9.2 Enhanced AAI Attempts

In line with the previously summarized testing in the EAAI configuration, multiple attempts have been made to demonstrate successful operation with hydrocarbon fuels. These attempts have included tests conducted with ethylene and methane fuels with ambient and elevated temperature air and with supplemental oxygen. This includes attempts taken with pure hydrocarbon and air mixtures and those taken with blended hydrogen/hydrocarbon and air mixtures. A total of approximately one hundred attempts in which a hydrocarbon fuel was introduced to the EAAI RDC have been made to date.

Successful operation in a rotating mode has yet to be demonstrated with the EAAI configuration with pure hydrocarbon fuels. Limited success has been found when operating with blended hydrogen/hydrocarbon mixtures, but rotational operation has only been demonstrated with fuel mixtures that were predominantly hydrogen. As such these cases are not considered to be indicative of successful operation with hydrocarbon fuels but are instead considered successful operation with a diluted hydrogen fuel.

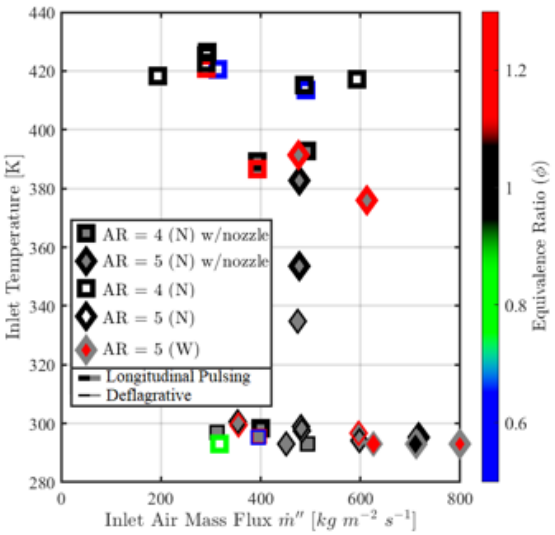

Figure 2.47: EAAI test conditions with pure ethylene/air mixtures.

A summary of the inlet conditions thus far tested with pure ethylene/air mixtures in the EAAI configuration is shown in Figure 2.47. Over forty individual tests have been conducted, including tests conducted with and without a 50% converging nozzle in the nominal channel configuration and a limited sequence conducted in the wide channel configuration. Recall that the wide channel configuration has an equivalent 47% converging nozzle with area matched to the no-nozzle nominal channel. The pebble bed was used to provide elevated inlet temperatures for a portion of the tests conducted in the nominal channel configuration, and will be used in the future for additional tests in the wide channel configuration. Two modes of operation have thus far been observed, that of a longitudinal pulsing mode and that of pure deflagrative combustion. The low-frequency (600-800 Hz) longitudinal mode has thus far been prevalent at elevated inlet temperatures in the nominal channel configuration. It was also found to be the predominant mode of operation in the few tests conducted with the wide channel. The non-periodic deflagrative mode of operation indicated no combustion confined to the RDC channel, all burning occurred in the expansion region near the continuously firing downstream afterburner following the RDC exhaust and facility exhaust system interface.

2.10 Upstream Propagating Oblique Shock Modeling

2.10.1 Theorized Flowfield Representation

To better understand some of the dynamics present in a practical RDC, we seek to develop simplified representations and models of the various waves that originate from the propagation of one or more detonation waves in the RDC. These models can be used to better understand the operation of RDCs, as well as inform future designs. The traditional, simplified and unwrapped flowfield of an RDC showing the most important features is shown in the schematic diagram of Figure 2.48(a). The detonation wave propagates into a layer of height h of detonable mixture generated by the fuel/oxidizer injection system which flows downstream. The problem is two-dimensional; i.e., The flowfield develops into a constant gap channel. In a RDC the layer forms a closed loop, hence propagation is periodic. The layer is bounded on the upstream side by a wall, which contains the point of entry (injection) of fuel and oxidizer, and on the downstream side by the post-detonation products generated by the detonation wave propagating into the layer in the previous cycle. In this figure, if something (fluid particle, wave, etc.) is propagating towards the top of the figure, we say it is propagating downstream. Likewise, upstream propagating would refer to moving towards the bottom of the figure. A contact surface (slip line) separates the fresh layer from the downstream reacted layer. Upon the passage of the detonation wave, the slip line is deflected by the combined effect of a downstream propagating oblique shock (OS) and expansion fan (EF) that aids in injector recovery [17]. This is identical to the semi-bounded detonation wave with an inert gas boundary studied first by Sommers and Morrison [18] and later by Sichel and Foster [19]. This problem has been recently revisited by Fievisohn and Houim [20] with application to RDCs. In an ideal system, it can be assumed that the oblique shock interacts solely with combustion products, which are treated as a high-temperature inert. Previous work has treated detonations in RDCs as being semi-bounded in that the inlet/downstream side has been treated as a solid wall fresh reactants enter through [17]. For rocket-style injectors, that have a solid wall at the end of the detonation chamber and small holes for jet injection, the semi-bounded description is adequate. However, in an air-breathing RDC design with a low-loss inlet, such as the contoured axial air inlet considered in this work, the openness of the inlet throat more freely allows for the propagation of waves upstream into the plenum. It is theorized that this would

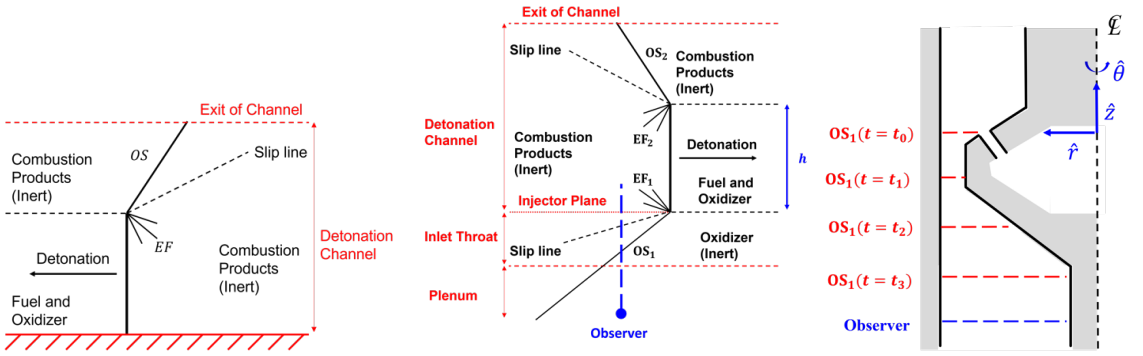

Figure 2.48: Ideal and simplified 2D steady flowfield in (a) rocket-style injector RDC and b) axial-air inlet (air-breathing) RDC. In case (b) the detonation wave is bounded on both ends by inert gases creating two free boundaries and two sets of oblique shocks (OS), slip lines, and expansion fans (EF). (c) Analogy to a quasi-1D, unsteady flow experienced by a fixed observer in plenum. Oblique shock is observed at different locations by the fixed observer at different times.

effectively create a second free boundary on the inlet side that has not been previously considered in detail.

A modified representation of the 2D steady flowfield in the RDC that removes the solid upstream (bottom) boundary is shown in Figure 2.48(b). The detonation wave is treated as being bounded on both sides by inert gases, with each free boundary also having an oblique shock (OS), slip-line, and expansion fan (EF) centered at the point of intersection of the detonation wave, the oblique shock, and expansion wave. Again, the inert gas downstream (top) is assumed to be post-combustion products with the added assumption that complete combustion occurs, infinitely fast reactions (i.e., infinitely thin detonation), and no downstream deflagration (either along the contact surface or other secondary combustion events) occurs due to complete combustion. These assumptions may not be representative of practical situations and may need to be rectified as the model is further developed to include non-ideal effects. The second inert gas upstream of the detonation wave is oxidizer (e.g., air) and originates from the axial inlet at the inlet conditions. Typically, the axial inlet is contoured; thus, the downstream free boundary develops through a variable-area (non-constant gap) channel. Red lines here denote important geometric locations along the axial distance,

while black lines differentiate different thermodynamic states. The oblique shocks and expansion fans are grouped together such that OS_1 and EF_1 are those generated by the downstream free boundary, while OS_2 and EF_2 are for the upstream free boundary. As drawn in Figure 2.48(b), the area change in the inlet portion and incoming air velocity change have both been neglected – these will be considered further below. One consequence of a non-zero incoming axial air velocity is that the detonation wave would be slanted in the frame of reference drawn in Figure 2.48(b). Additionally, the area change and corresponding variation in incoming oxidizer velocity would lead to OS_1 being curved. Other waves and/or slip lines would also have curvature if these details are fully considered. However, solving for the proper shape of these waves is beyond the scope of this work. Thus, for now, we shall treat the flowfield as being represented by Figure 2.48(b) in a constant gap channel, with no inlet velocity and no tilt to the detonation wave.

In this work, we will often take the point of view of a fixed observer in the plenum when analyzing the problem. This fixed observer looks down the combustor across an infinitely thin azimuthal slice; i.e., it observers only a one-dimensional (1D) axial view of the problem. In Figure 2.48(b) the blue dot represents the fixed observer while the dashed blue line indicates the axis of the corresponding 1D problem constructed around the fixed observer. By considering the point of view or reference frame of the fixed observer, we effectively reduce the steady 2D flowfield to the quasi-1D problem shown in Figure 2.48(c). We now consider the detonation wave system to be unsteady so the detonation wave, oblique shock, and expansion fan propagate from left to right as shown in Figure 2.48(b) at equal speed. Because the fixed observer is stationary in space and observes the problem in a 1D sense only (axial view only), it perceives the lateral (rotational) motion of the oblique shock OS_1 as corresponding to a shock wave moving axially upstream (i.e., toward it). In other words, the position of OS_1 relative to the fixed observer changes over time only in the axial direction (along the blue dash line of Figure 2.48(b)). This is also shown in Figure 2.48(c) as the different dashed red lines. Thus, to the fixed observer, the OS_1 has an apparent axial velocity as the 1D shock wave propagates from the detonation towards the fixed observer. This apparent axial velocity is a result of the rotation of the oblique shock and its angle relative to the viewpoint of the fixed observer. It is in this context that we can assign an axial speed to the OS_1 to study its strength as well as constructing a quasi-1D shock tube model for evaluating the change in its strength across the area change of the inlet. This will be further developed subsequently. Here we focus only on the oxidizer inlet and at this time have not extended the analysis to the fuel injector. However, the

methods presented in this work can also apply to the fuel injector, depending on the configuration, to analyze the disturbances that propagate into the fuel plenum.

2.10.2 Quantification of Oblique Shock Strength Penetrating The Inlet

By taking the average of pressure ratio distribution found using the method outline in Section 2.3.2 ($\langle p_{r,2} \rangle$), a measure of the strength of the wave in the plenum for a given operating condition can be better explored. The average pressure ratios are shown in Figure 2.49. Here it can be seen that while smaller than the pressure ratios observed in the detonation channel, a finite pressure ratio is observed far upstream of the air inlet into the plenum. There is no immediately apparent relationship between the pressure ratio and either mass flux or equivalence ratio. On average, for a given air mass flux, the more open throat cases (triangles) have a larger pressure ratio than the more constrictive throat cases (circles). This could either indicate a greater coupling between the plenum and the detonation channel and/or fewer losses in the inlet throat that affect the penetration of OS_1 across the inlet into the plenum. Regardless, we can conclude that OS_1 in this system has a non-negligible strength in the plenum – between 20% to 40% – which may impact the integration of an RDC with upstream components, such as a compressor or isolator.

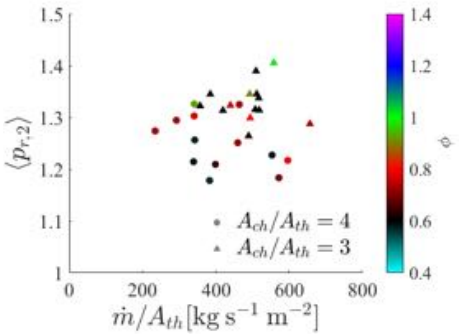

Figure 2.49: Average pressure ratio across wave observed in air plenum.

Utilizing the measured average pressure ratio in the plenum ($\langle p_{r,2} \rangle$) and following the procedures outlined in greater detail in [21], the axial velocity of OS_1 in the plenum at the sensor location can be numerically solved for. From the velocity, the Mach number in the fixed observer frame and fluid frame (which we denote with superscript f) can be defined relative to the speed of sound of the incoming air:

$$M_{z,2} = \frac{u_{z,2}}{a_2} \tag{2.19}$$

$$M_{z,2}^{f} = \frac{u_{z,2} + u_{a,2}}{a_2} \tag{2.20}$$

The Mach number of the OS_1 in the fixed observer frame from this analysis for all the conditions tested in this work are shown in Figure 2.50(a). From Figure 2.50(a), it is found that to a fixed observer the OS_1 is traveling near the speed of sound of the incoming air in the plenum with a Mach number of about 1.1. To the incoming fluid element, the wave is coming in at about Mach 1.2 since the fluid element is traveling at about Mach 0.1 in the plenum. This is shown in Figure 2.50(b). It is expected that as the wave continues to propagate if the plenum was infinitely long, the wave would decay under the action of viscous forces until it was acoustic in nature; however, due to the finite size of the plenum, the wave likely did not decay entirely prior to reaching the end of the plenum in the tests conducted. It is theorized that if there were surfaces within the plenum that the wave could then reflect off of, the flowfield would be further complicated by the interactions of the waves penetrating into the plenum and reflections from previous cycles. This possibility is neglected in the current discussion as we consider a purely axial combustor, though it may be worth studying in the future.

2.10.3 Time of Flight Measurement of Upstream Propagating Disturbances

The time difference (Δt) between the observed peaks in the pressure traces measured in the channel and plenum, is also computed and analyzed to study OS_1. Shown in Figure 2.51(a) are the average time differences ($\langle \Delta t \rangle$) for the various conditions tested. There is no discernible trend with air mass flux, equivalence ratio, or area ratio, with most of the data points falling within ± 10% of the average of 2.2E-4 s. We then normalize by the period of the detonation (τ_D) to provide a sense of scale, which is shown in Figure 2.51(b). The period of the detonation wave, shown in Figure 2.51(c), is calculated from the observed wave speed and the circumference of the midpoint in the detonation channel. Most of the normalized time of flight values ($\langle \Delta t \rangle / \tau_D$) are around 0.6. On average, the normalized time of flight increases linearly with increasing air mass flux, with no obvious difference between the two cases with different area ratios. This occurs despite the decrease in the detonation period with increasing air mass flux. This suggests that although the detonation wave sees an increase in speed with increasing mass flux, the OS_1 has less variation in its axial speed with air mass flux. Referring back to Figure 2.50(a), the estimated axial velocity of OS_1 varies by about 35 m/s across all conditions, which is an order of magnitude smaller than the change in the detonation wave speed, which is over 200

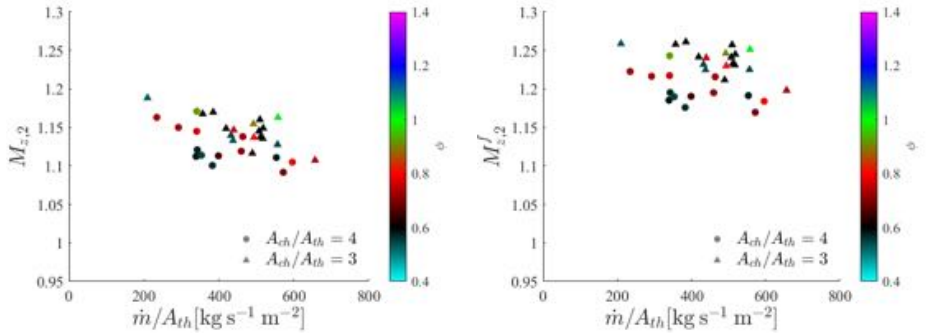

(a) (b)

Figure 2.50: Estimated Mach numbers of OS_1 in plenum for (a) laboratory and (b) fluid particle frame of reference. Wave travels near acoustic speed upstream in laboratory reference frame at the measurement point.

m/s between the lowest and highest air mass fluxes. Therefore, while the azimuthal speed of the OS_1 would vary with the detonation wave speed by being attached to the bottom of the wave, the axial velocity of OS_1 does not have a strong dependence on the strength of the detonation wave. This suggests that the wave angle α of OS_1 varies correspondingly to changes in wave speed.

2.10.4 Fluid Residence Time of Plenum

The assumption of the incoming flow in the plenum/inlet is undisturbed prior to the passage of OS_1 can be evaluated somewhat readily by taking the undisturbed velocity in the plenum computed previously ($u^-_{a,2}$) and applying area-velocity relations through the use of the sonic $\circledast$ state. The reference sonic area A^* can be computed from the high-speed pressure measurement according to:

$$A^* = A_2 \sqrt{\left(\frac{\langle u^-_{a,2}\rangle}{a_2}\right)^2 \frac{2}{\gamma+1}\left[1+\frac{\gamma-1}{2}\left(\frac{\langle u^-_{a,2}\rangle}{a_2}\right)^2\right]^{\frac{-\gamma-1}{\gamma-1}}} \tag{2.21}$$

We then apply the assumption that the undisturbed flow along the variable area plenum and inlet is isentropic and quasi-one-dimensional. This neglects any radial velocity component due to the curve of the variable area geometry of the plenum and

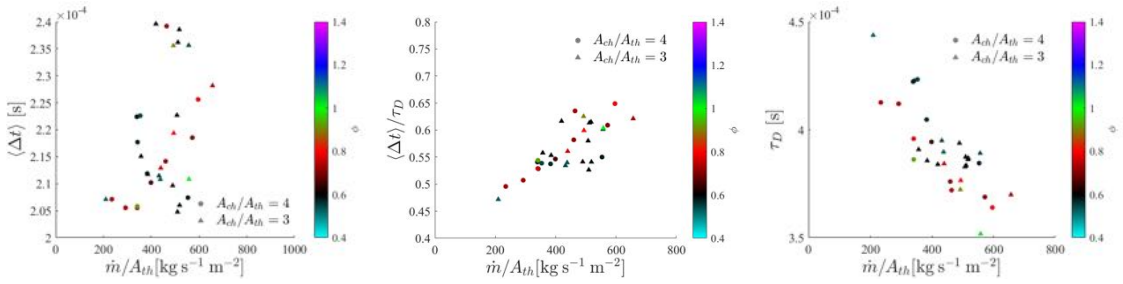

(a) (b) (c)

Figure 2.51: (a) Average time between pressure measurements taken in detonation channel and plenum ($\langle \Delta t \rangle$) does not vary much with mass flux; (b) ratio of $\langle \Delta t \rangle$ and the detonation period (τ_D) increases with mass flux; and (c) detonation period decreases with increasing mass flux.

inlet. Within a quasi-one-dimensional approximation, while accounting for any flow turning that may be imposed by the variable area geometry, the mid-line between the inner and outer walls is taken as the streamline ($\vec{S}$) along which the oxidizer fluid particles travel along. Therefore, instead of being purely a function of the axial location, z, we find the areas along this streamline and parametrize it by the curvilinear variable S, which itself is a function of axial and radial location.

In computing the stream-wise velocity of the undisturbed air, it was found that for all of the air mass fluxes that exhibited detonation, the undisturbed flow became choked in the inlet. This is not necessarily equivalent to having the entire inlet choked since computationally it has been observed that the inlet is momentarily un-choked [15]. It is likely that OS_1 is the mechanism by which the inlet becomes un-unchoked. This is consistent with numerical simulations of RDC operation [22] and our own work.

Integrating the velocity with respect to the distance along the streamline, the time it takes a fluid particle entering the base of the plenum to reach the fuel injector plane (S_{inj}) can be estimated. This quantity is referred to here as the residence time of the fluid particle τ_P:

$$\tau_P = \int_0^{S_{inj}} \frac{\mathrm{d}S'}{u_a(S)} \tag{2.22}$$

The comparisons of this residence time to the detonation period and the experimental time of flight of the upstream propagating disturbance are shown in Figure

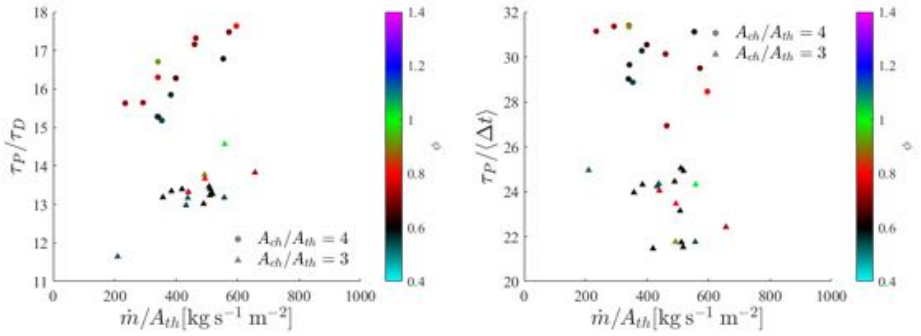

(a) (b)

Figure 2.52: Time it takes for fluid particle to go from bottom of plenum to injector plane relative to (a) detonation period and (b) time for OS_1 to travel from injector to sensor in plenum. Fluid particle would see multiple shocks prior to entering the detonation channel.

2.52(a) and Figure 2.52(b), respectively. From these figures, it is seen that the residence time is nearly an order of magnitude larger than both the detonation period and the time it takes for the OS_1 to travel into the plenum. Because of this, a fluid element entering the plenum would experience multiple oblique shocks prior to arriving at the injector plane. However, at each oblique shock, the fluid particle should also encounter an upstream propagating expansion fan that turns the flow again to remove some of the azimuthal velocity that was imparted from the oblique shock. Despite the expansion waves, after each subsequent oblique shock encountered by the fluid particle would transfer more of the kinetic energy into thermal energy. As these effects compound, the OS_1 would have additional curvature caused by these varying properties, which is not captured by the present model. Furthermore, this would result in multiple drops of stagnation pressure across the plenum and inlet which may not be well characterized when the pressure gain across the RDC is defined [23].

2.10.5 Quasi-1D Shock Tube Analogy

While $\langle\Delta t\rangle$ could be used to calculate an average upstream propagation speed of OS_1 perceived by a fixed observer in the plenum, this average speed neglects the finer details of the propagation along the variable flow speed field imposed by the

area change of the inlet throat. To account for the change in Mach number and corresponding pressure change through the converging section of the inlet, a more refined model describing the propagation of OS_1 in the air inlet is considered and developed next. This model will also allow for the evaluation of the response of and flow losses across the inlet throat.

Following the basic idea outlined initially, the refined model describes the axial propagation of OS_1 as perceived by a fixed observer in the plenum (see Figure 2.48(c)). We can leverage again the analogy that the rotating OS_1 (azimuthal motion) is perceived by a fixed observer in the plenum as a shock wave approaching the fixed observer at a speed $u_{\vec{S}}$ along $\vec{S}$. Then, the approach speed $u_{\vec{S}}$ is solely related by geometric consideration to the rotational speed D and the angle α of OS_1. This suggests that the problem can be described in a simplified manner by considering the analogous problem of a shock wave propagating in a tube with a variable area (because of the inlet). The shock wave is supported by the pressure rise across the detonation wave moving at D. Therefore, we essentially treat the problem as a quasi-1D shock tube problem that includes the effect of area change in the propagation of the shock wave. This problem is similar to the problem considered by Chester [24], Chisnell [25], and Whitham [26]. The model is based on the following assumptions and simplifications to allow the use of the formulations proposed by Chester, Chisnell, and Whitham:

1. We consider only the component of the OS_1 propagation velocity along streamline $\vec{S}$ and neglect the azimuthal component.

2. The azimuthal component is unaffected by the axial area change and it is always equal to detonation wave speed D so that OS_1 remains attached to the bottom of the detonation wave.

3. The wave is planar and has no variation normal to the streamline $\vec{S}$.

4. Viscous losses along the wall are neglected.

5. The pressure downstream of the detonation wave in the channel remains constant; i.e., the pressure decrease and the recovery of the injector is not considered at this time.

6. Downstream propagating disturbances caused by reflections of upstream propagating waves due to area changes are neglected.

7. The shock propagates into a homogeneous fluid with constant pressure and density.

8. The shock propagates into quiescent flow (i.e., the motion of the air in the variable area inlet is neglected.) This assumption will later be relaxed by introducing a correction to account for the flow in the inlet.

The description of a shock propagating through an area change was formulated by Chester [24], Chisnell [25], and later Whitham [26] independently through different methods. Chester approached the problem by applying small perturbation theory for the flow behind a propagating shock wave caused by area change and linearized the equations of motion based upon a small area change assumption. Chisnell, on the other hand, produced a first-order relationship between area change and Mach number by decomposing the problem into many sequential shock tubes with small area changes. Though the derivation was different, the resulting relationship were functionally similar. Finally, Whitham presented a simplified derivation based on the integration of the compatibility equations along characteristic directions while imposing the Rankine-Hugoniot relations across the shock front to derive the same results of Chester and Chisnell. The end result is Eq. 2.23 which is an ODE that relates the change in shock propagation Mach number to change in cross-sectional area:

$$\frac{\mathrm{d}A}{A(S)} = -\left[\frac{2M_{\vec{S}}}{K(M_{\vec{S}})(M_{\vec{S}}^2-1)}\right]\mathrm{d}M_{\vec{S}} \tag{2.23}$$

where

$$K(M_{\vec{S}}) = 2\left[\left(1+\frac{2}{\gamma+1}\frac{1-\mu(M_{\vec{S}})^2}{\mu(M_{\vec{S}})}\right)\left(2\mu(M_{\vec{S}})+1+M_{\vec{S}}^{-2}\right)\right]^{-1} \tag{2.24}$$

and

$$\mu(M_{\vec{S}})^2 = \frac{(\gamma-1)M_{\vec{S}}^2+2}{2\gamma M_{\vec{S}}^2-\gamma+1} \tag{2.25}$$

Here we use $M_{\vec{S}}$ to denote the Mach number of the OS_1 propagation velocity parallel to $\vec{S}$ and it is assumed that this quantity is uniform on a surface normal to $\vec{S}$ at any given location. Based on the geometry of the variable area inlet and plenum, this Mach number could have a radial component in addition to the axial one at certain points in the flow.

When compared to experimental shock tube data, Chisnell [25] and Whitham [26] both found good agreement for a range of initial Mach numbers and for small instantaneous area changes. Large instantaneous area changes resulted in disturbance reflections becoming non-negligible [25]. To better match experimental shock tube data from Smith (which had a data-set with larger instantaneous area changes) [27], Milton expanded Eq. 2.23 by deriving a higher-order correction term to account for the Mach reflections that occur in the area change [28]. This results in Eq. 2.26:

$$\frac{\mathrm{d}A}{A(S)} = -\left[\frac{2M_{\vec{S}}}{K(M_{\vec{S}})(M_{\vec{S}}^2-1)} + \frac{\eta(M_{\vec{S}}, A(S))}{M_{\vec{S}}}\right]\mathrm{d}M_{\vec{S}} \tag{2.26}$$

where $\eta(M_{\vec{S}}, A(S))$ in Eq. 2.26 is defined as:

$$\eta(M_{\vec{S}}, A(S)) = \frac{1}{2\gamma}\left[\left(\frac{\gamma(\gamma-1)}{2}\right)^{1/2}+1\right]\left(1-\frac{M_{\vec{S},0}^2}{M_{\vec{S}}^2}\right)+\frac{1}{2}\ln\left(\frac{A_0}{A(S)}\right) \tag{2.27}$$

and it is the additional term (compare to Eq. 2.23) that arises when changes along the characteristic lines due to wave reflection at points of variable area are included. The subscript "0" denotes the conditions of the main shock wave; i.e., the initial conditions.

With a known area distribution along the streamline ($A(S)$) and γ along with an assumed initial area (A_0), the numerical integration of Eq. 2.26 can be iteratively solved for using different inital Mach numbers ($M_{\vec{S},0}$) values until the modeled time of flight estimated matches the one measured experimentally. This gives the sought estimate of the propagation axial Mach number through the inlet and plenum.

Sample results from this analysis is shown in Figure 2.53 for $\dot{m}/A_{th} = 399$ kg s^{-1} m^{-2}, $\phi = 0.65$, and $A_{ch}/A_{th} = 4$. In Figure 2.53(a) the Mach number is evaluated in the fixed observer frame of reference, while in Figure 2.53(b) it is expressed in the frame of reference where the fluid particle is at rest. The difference between these two distributions then is the velocity distribution of the downstream propagating oxidizer. Here the fuel injector plane is set to be at the origin of the x-axis, and the plenum pressure transducer is at the end of the shown curves. In the fluid particle reference frame, the wave accelerates through the area contraction in the inlet before slowing down once the larger plenum is reached. These results are expected from the negative sign in Eq. 2.26. Due to the high speeds of the oxidizer in the inlet, to the fixed observer, the OS_1 actually appears to slow to subsonic speeds while traveling

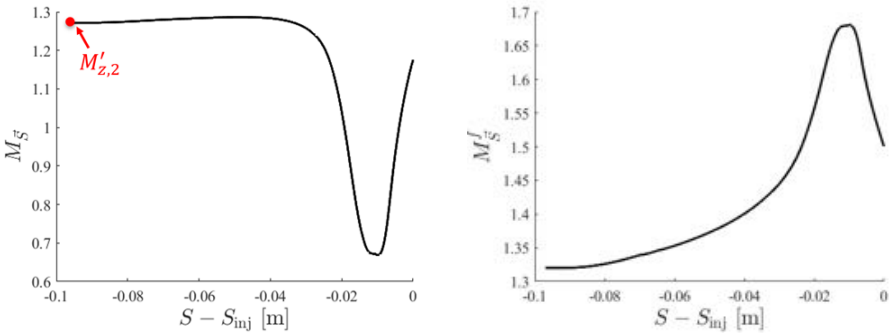

(a) (b)

Figure 2.53: Variation of Mach number along streamline in (a) fixed observer and (b) fluid particle frame of reference. Difference between curves is fluid particle velocity. Fluid particle experiences different shocks depending on position in plenum/inlet.

through the inlet before becoming supersonic in the plenum. It might appear that it is subsonic, but in reality, the wave is supersonic as viewed by the fluid.

This model was run for all of the detonative conditions in this work. The endpoint of the distribution in Figure 2.53(a) is labeled as $M'_{z,2}$ to draw comparison to the experimental estimates of the axial Mach number in the plenum discussed in a previous section since the streamline is purely axial at the sensor location. Again the $\prime$ is used to differentiate the model results from the experimental estimates. The modeled plenum Mach numbers in the plenum for all the considered cases are shown in Figure 2.54(a). Effectively there is a constant value of $M'_{z,2}$ (of about 1.25) across all the operating conditions considered. Similarly, differences in throat area do not have a definitive impact on $M'_{z,2}$ since both area ratios resulted in the nearly constant $M'_{z,2}$ value.

Figure 2.54(b) compares the modeled Mach numbers to those computed using the measured pressure ratio in the plenum – see Section 2.10.2. – and reveals a discrepancy between the two values since all the data points are above the 1:1 dashed line. This indicates that the model predicts in the plenum a faster-moving wave than what is estimated from the pressure ratios; thus, it also overpredicts the pressure raise that would be observed in the plenum. A possible explanation for this large discrepancy is the assumption imposed that the pressure downstream of the shock in the quasi-1D shock tube is constant. This assumption ignores the pressure relief caused

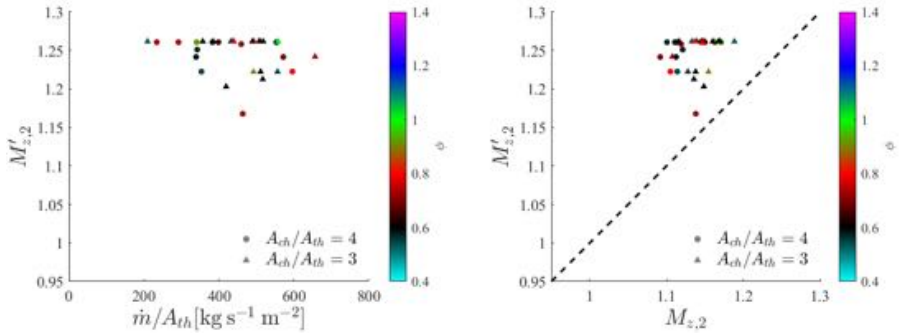

(a) (b)

Figure 2.54: (a) Modeled streamline Mach number of OS_1 in plenum ($M'_{Z,2}$) as viewed in the laboratory reference frame; and (b) $M'_{Z,2}$ agrees favorably with computed Mach number based upon measured pressure ratio ($M_{Z,2}$).

by the upstream propagation expansion wave. With a decrease in the downstream pressure, the upstream propagating wave would travel at lower speeds. If described in the fixed observer frame, this effect results from the interaction of an upstream propagating expansion wave that slows the shock wave, while in the detonation wave frame this effect results from the upstream propagation wave curving the OS_1. Further improvements to this model could try to capture these additional phenomena and interactions, which may result in a better prediction of the speed and strength of the upstream propagating shock in the plenum. Nevertheless, both methods suggest that the wave is approaching acoustic speeds in the plenum.

2.10.6 Thermodynamic State Considerations

One of the implications of having an oblique shock traveling upstream into the plenum is the changes of the thermodynamic state of the flow entering into the combustor that the oblique shock may cause. In addition, the presence of an upstream propagating oblique shock contributes to the losses (e.g., stagnation pressure losses) experienced at the inlet. As we have seen from the model results, relative to the incoming fluid particles, that the oblique shock appears stronger at different locations along the streamline (Figure 2.53(b)). For example, a fluid particle at the throat of the inlet, where it is nearly at sonic speed, experiences a stronger incoming shock wave than

a fluid particle in the plenum, which is moving at a much slower speed. Hence, (stagnation pressure) losses experienced by fluid particles at the inlet throat are larger than those experienced by fluid particles further upstream from the inlet throat. Additionally, because the fluid transit time through the inlet is much larger than the rotational time of the detonation wave, a fluid element emerging from the inlet experiences several passages of OS_1, hence it undergoes multiple loss events.

2.11 Up-Conversion Imaging of CO_2

2.11.1 Introduction

In this work we discuss the application of mid-IR pulsed UpConversion Imaging (UCI) to combustion systems, where UCI is used to narrow the spectral response of the imaging system to target selected chemical species. Extending the spectral selectivity into the mid-IR wavelength range allows a variety of important combustion species to be targeted.

UCI is an approach based on Sum-Frequency Generation (SFG) in nonlinear optical materials that causes the incident light to be converted into light at a shorter wavelength. This effect can be used in single-point mode or in imaging configurations where the resulting image is captured by an imaging detector. By shifting light to shorter wavelengths, UCI can be applied to image mid-IR scenes using traditional cameras that are sensitive only to visible and near-IR wavelengths. In practice, this is achieved by directing mid-IR light carrying the scene of interest into a medium (typically a bulk crystal) exhibiting second-order optical nonlinearity and combining with a "pump" light beam (typically produced by a laser). Nonlinear optical effects cause photons from the mid-IR image and the pump beam to be annihilated in pairs that each produce a signal photon that has an energy equal to the sum of the energies of the annihilated photons. In this work a 1.064 µm pump beam is used to upconvert mid-IR light in the range of 1.9 µm-4.4 µm to the near-IR range of 700 nm-860 nm that can be efficiently detected by a silicon CCD sensor. Selection of the pump laser wavelength and the properties of the nonlinear crystal allow particular mid-IR spectral bands to be converted while others are not, effectively providing spectral filtering.

We have designed and characterized a UCI system for mid-IR imaging of emission/absorption by species of interest in combustion systems, as well as we have evaluated its use in an RDE. Initially the system has been tested by conducting UCI measurements on simple configurations, such as imaging of mid-IR blackbody radia-

tion to evaluate spatial resolution, Signal-to-Noise Ratio (SNR) considerations, and responsivity; and thermal radiation from CO_2 and H_2O in methane-air flat flames. As a demonstration, UCI is applied to the RDE to make species-specific imaging measurements of CO_2 thermal radiation emission in an optically-accessible RDC.

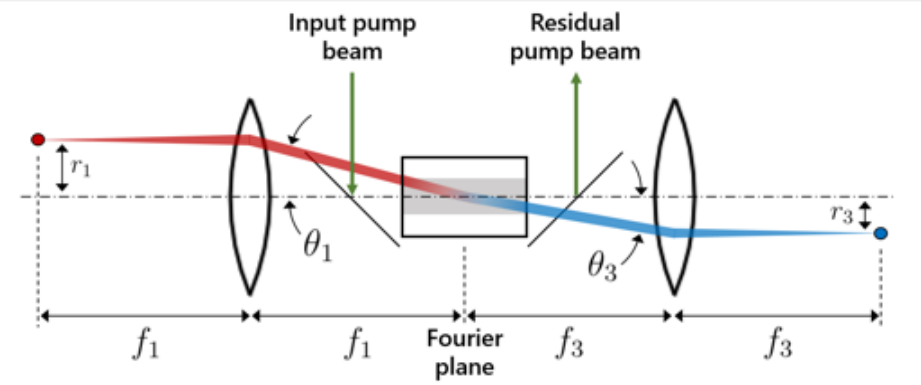

Figure 2.55: A notional schematic of a 4f UCI imaging system that converts a mid-IR image coming from the left into a shorter wavelength signal image that is detected on the right.

2.11.2 Experimental setup

This work adopts the 4f optical arrangement for UCI of incoherent mid-IR light that was described by Pedersen et al. [29] and shown in the notional schematic in Figure 2.55. This configuration includes two lens: an objective lens placed its focal length away from the object plane and a collection lens placed behind the objective lens at a distance equal to the sum of the two focal lengths. The pump beam is injected into the optics train with a beamcombiner placed between the objective lens and the Fourier plane located at the focal distance from each lens. By placing the nonlinear crystal at the Fourier plane it acts as an aperture that produces a filtering of spatial frequencies in the image [30].

The pump beam was formed by the fundamental wavelength (1.064 µm) output of an Nd:YAG laser system (Spectra-Physics Q-Ray Lab 250). For the preliminary measurements in this section all images were captured using the laser in long-pulse mode to achieve sufficient Signal-to-Noise Ratios (SNRs) for the desired application.

Long-pulse mode results in a temporal train of many low energy pulses occurring over a window of approximately 125 µs that produces an effective exposure time of between 100 ns and 300 ns. The 4f optical arrangement in these measurements used an objective lens focal length of 100 mm and a collection lens focal length of 150 mm. A mid-IR AR-coated 50 mm diameter Germanium window was placed in front of the objective lens to remove any contributions from wavelengths below 1.6 µm. The nonlinear crystal chip was placed at the Fourier plane and has dimensions of 10 mm × 10 mm × 1 mm with five differently poled gratings inserted side-by-side within the chip. Those gratings are each 1 mm wide. Images were detected using a back-illuminated CCD (Andor Technology Newton 940-BU2) that is sensitive between 200 nm and 1100 nm. The back-illuminated architecture causes fringing patterns to appear in the upconverted images due to spatial coherence induced by the SFG process. By stabilizing the temperature of the sensor with its built-in TE cooler and taking white-field images with a uniform blackbody emitter, these fringe patterns can be removed in post-processing.

2.11.3 Examples of upconversion of radiation from blackbody emitter

To demonstrate and verify the upconversion capability of our system we have designed and developed, we image the uniform output of a 1 inch aperture blackbody source. This provides a spatially uniform imaging target for the system to be conveniently tested. The blackbody spectral intensity from the source at a particular temperature T_B setting can be predicted with the Planck relation. When the pump laser is operated in long-pulse mode the pump intensity will remain low enough such that the SFG efficiency and overall signal strength will be proportional to pump pulse energy.

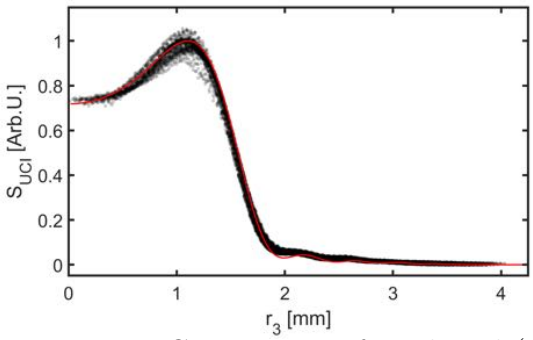

Figure 2.56: Comparison of predicted (solid line) and measured (symbols) blackbody emission images.

Figure 2.56 shows a comparison between the measured and predicted blackbody radiation image for a case where the blackbody source was maintained at a blackbody

temperature of 900 K. Because blackbody source is uniform, and the UCI system generates an axisymmetric image for a uniform source, the image is converted into a one dimensional plot showing the variation of the detected signal as a function of radial distance from the center of the optical axis. Prediction and measurements compare very favorable, demonstrating the ability to finely control these processes.

2.11.4 Examples of upconversion of emission from H_2O and CO_2 from a flat flame burner

To test the capability of the UCI system to perform single-shot measurements of thermally excited mid-IR radiation in combustion environments, images were captured within a methane/air flat flame stabilized on a McKenna burner. The burner was operated with an equivalence ratio of 1.07 and a reactant velocity at the burner surface of 38 cm/s.

Examples of single-shot pulsed UCI measurements of radiative emissions from the McKenna burner flame are shown in Fig. 2.57(a) for the H_2O bands and (b) for the CO_2 bands. The location of the surface of the burner is shown by the green line at $y = 0$. It should be noted that the field of view limitations in each of the two examples occur by different mechanisms. The H_2O signal is limited by the clear aperture of the imaging optics. The field of view of the CO_2 measurements is not limited by a physical aperture, but instead by the maximum angle that can achieve QPM at IR wavelengths and is a manifestation of the spatial-spectral coupling effect that characterizes our UCI system, as for example shown in Fig. 2.56. Some signal is observed below the surface of the burner, as determined by calibration images taken by back-illuminating the burner prior to igniting the flame. This is due to mid-IR reflections off of the polished stainless steel angled surface around the edge of the burner.

The primary reason for the disparity between the signal strengths of the CO_2 and H_2O emissions measurements is the difference in spectral bandwidths at the two wavelengths. The UCI spectral bandwidth is larger by a factor of 45 at 4.2 µm compared to the value at 2.55 µm. This difference in spectral response, combined with the stronger CO_2 radiative emissions, generate approximately 25 times the signal for passive imaging of CO_2 compared to H_2O. The SNRs of these single shot

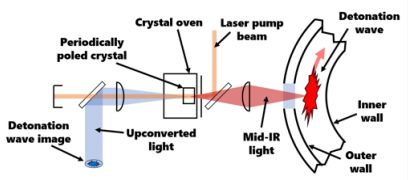

Figure 2.58: Diagram of the UCI system on the RDE.

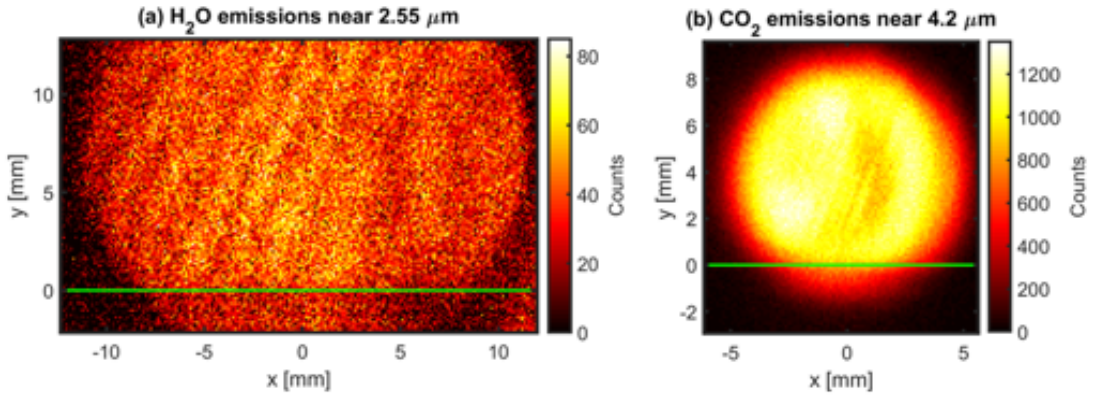

Figure 2.57: Images of (a) H_2O and (b) CO_2 on a methane/air flat flame burner at an equivalence ratio of 1.07.

images were approximately 35 for CO_2 imaging and 3.5 for H_2O imaging.

It is important to note that the measurement shown in Fig. 2.57 exhibit spectral fringing, as seen from the striations that are observable in the H_2O emission image (but not as clear for CO_2 emission; the wider bandwidth for CO_2 effectively washes out the fringing effect). Fringing results for an interference effect of detected narrowband light on the camera sensor itself, and it is not due to the UCI process or system. Although correction is possible, effective correction of this fringing pattern with flat-fielding is a bit difficult in practice because the flat-field light must exhibit the same spectral content as that of the intended target field. In measurements taken later in an RDE flat-field correction for removing fringe patterns is indeed conducted successfully to realize the structure of the detonation wave as rendered by CO_2 thermal emission.

2.11.5 Measurements in a rotating detonation combustor

To demonstrate the capabilities of the pulsed mid-IR UCI system in this work to capture spatiotemporally resolved mid-IR images in unsteady combustion environments, experiments were performed to image thermal IR radiation from within the combustion channel of an RDC. These experiments were conducted in a laboratory scale 6 inch diameter RDC that has previously been characterized [31]. A 25 mm diameter sapphire window was installed into the outer wall of the combustion channel about 50 mm downstream of the inlet (which correspond to about half of the total length of the combustor where the detonation wave sits) to image mid-IR radiation from

within the combustor. A schematic diagram of the UCI system integrated with the RDE is shown in Fig. 2.58.

Since the effective exposure of the image is controlled by the temporal properties of the pump beam, to achieve sufficiently fast gating to freeze the detonation wave front (typically moving between 1 km/s to 1.5 km/s) to within less than 1 mm, while obtaining sufficiently high signal strengths and acceptable SNRs, the temporal profile of the pulse beam was suitably shaped. Through a numerical analysis and experimental validation, it was found that operation with a pump laser with a pulse width of 240 ns and energy level around 8 mJ/pulse was optimal to achieve adequate conversion efficiency, signal strengths and SNR. This is what was used to acquire the results shown next, and it has been guiding us in the selection of the pulse burst laser requested here.

The RDC was operated with non-premixed hydrogen/air mixture, both seeded with 5% or 10% of CO_2 by volume. The UCI system was tuned to access the asymmetric C–O stretch bands of CO_2 near 4.2 µm. The addition of CO_2 in equal amount in both the fuel and oxidizer streams while using hydrogen fuel allow us to isolate the effects of mixing and combustion (of an hydrocarbon fuel), and remain (primarily) sensitive to the high temperature and pressure regions across the detonation wave. This scheme was in fact implemented to specifically detect the high temperature and high pressure regions of the detonation wave. What shown here refers to an operation of the RDC with an air flow rate of 0.2 kg/s and equivalence ratio between 0.6 and 1.2. The UCI system was pumped by a 10 Hz pulsed Nd:YAG laser and it was operated independently of the operation of the RDE (i.e., asynchronous to the propagation of the detonation wave). Thus, for each run of the RDE a series of uncorrelated images of the thermal emission of CO_2 was acquired. The RDE is instrumented with several high speed pressure transducers, a high-speed OH* chemiluminescence emission sensor nearly co-located with the UCI system, and a high speed camera to acquire chemiluminescence emission of OH* aft the engine. This instrumentation, synchronized with the acquisition of the UCI images, was sufficient to establish the time of acquisition of each UCI relative to the azimuthal location of the detonation wave front in the annulus. By repeating measurements multiple times, the evolution of the thermal emission of CO_2 across the detonation wave cycle was then reconstructed.

Examples of UCI measurements of detonation wave fronts after correction of fringe patters and accounting for the spatial variation of signal due to the spatial-spectral response coupling, is shown in Fig. 2.59. The UCI frame in Fig. 2.59(a) was captured with the combustor doped at 5% CO_2 by volume and a global equivalence ratio of

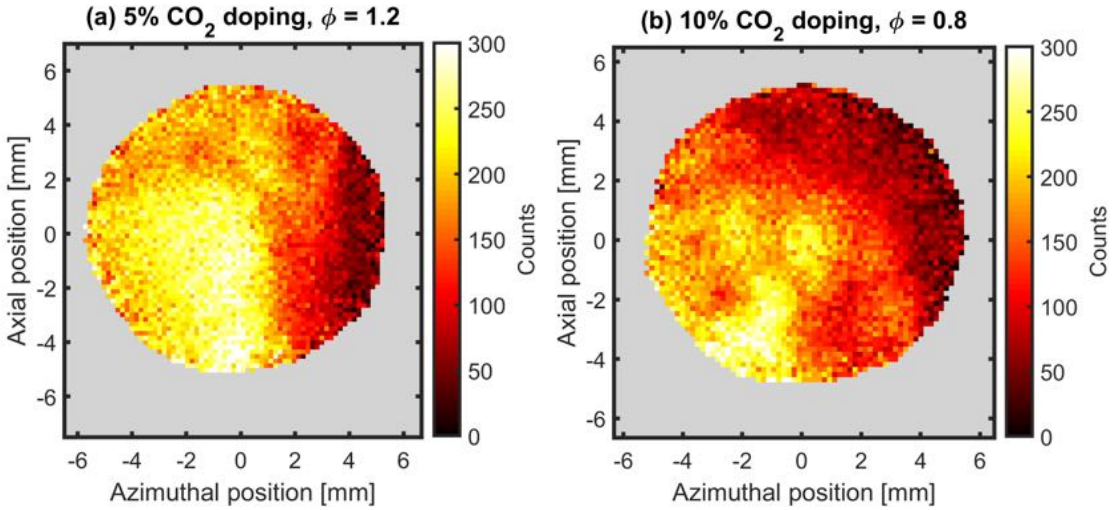

Figure 2.59: Example of CO_2 thermal emission at the detonation wave for different operation of the RDC: (a) $\phi = 1.2$, and (b) $\phi = 0.8$. In both cases, the air flow rate was 0.2 kg/s. Operation in hydrogen/air with seeded CO_2 in both fuel and oxidizer streams. Images were flat field corrected.

$\phi = 1.2$ while the example in Fig. 2.59(b) was for operating parameters of 10% CO_2 and $\phi = 0.8$. In both cases, the frames show a case where the detonation wave was within or near the collection window. The wave is moving from left to right of the frame, with the inlet to the bottom and the exit nozzle to the top. In these examples, the dim regions near the right of the frames are regions of low temperature, unburnt gas that the detonation wave front is propagation into, and the bright regions near the left of the frame are high-temperature, high-pressure combustion products.

One consequence of the spatial-spectral coupling effect is the limited field of view for UCI measurements at this wavelength. This was previously observed in the characterization measurements of Fig. 2.56. In this case, the system only responds to mid-IR signals within an approximately 1 cm diameter circular region in the object plane. Regions outside the area where at least 25% of the conversion efficiency is achieved were masked out due to excessive noise. Overall, these measurements demonstrate the capability of the UCI system to resolve the millimeter-scale structures and spatial gradients associated with RDC detonation waves, in spite of the somewhat limited overall field of view.

By acquiring multiple uncorrelated images, and correlating them to the phase

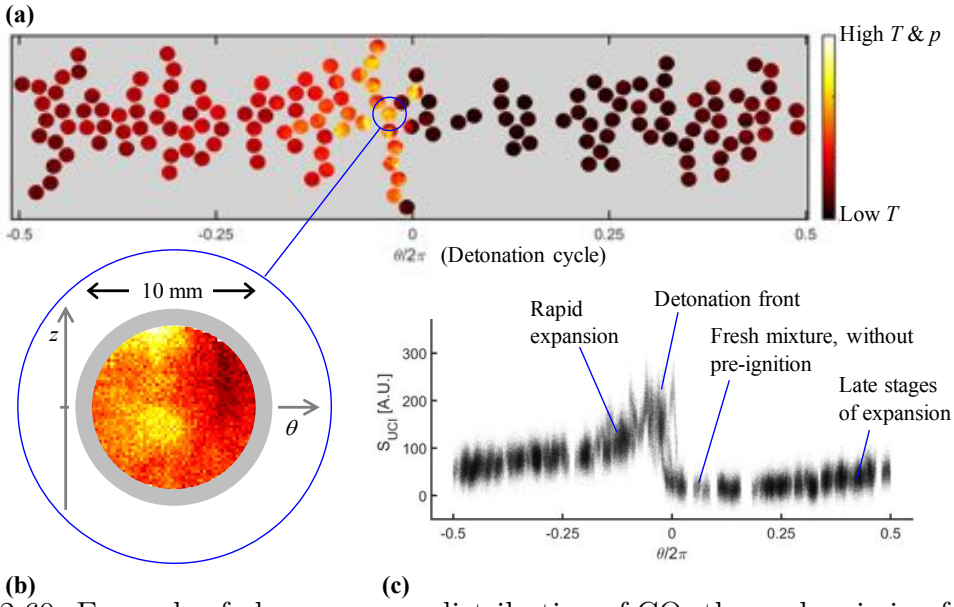

Figure 2.60: Example of phase-average distribution of CO_2 thermal emission for RDC operation at $\phi = 1$, air flow rate of 0.2 kg/s and 5% of CO_2 seeding in both fuel and oxidizer streams. (a) phase-synchronized ensemble of CO_2 thermal emission images near 4.3 μm showing the evolution of high-pressure/high-temperature regions across the cycle; (b) example of instantaneous structure of detonation front; (c) phase-average distribution of CO_2 thermal emission showing the most salient phases of the cycle.

of the detonation wave as briefly introduced above, phase-synchronous or phase-average representations of the CO_2 emission across the detonation wave cycle was constructed. Figure 2.60 shows an organized collection of single shot frames, properly synchronized to the detonation wave. In this case the wave is moving from left to right, with the inlet below the wave and the exit nozzle above. Figure 2.60a is a visual representation of the spatial distribution across the cycle of the detonation wave, where each uncorrelated image has been placed on the $(0, 2\pi)$ phase plane of the cycle, relative to the detonation front. Since all images where taken at the same fixed position in the RDC (relative to the lab) and the wave rotates in the azimuthal direction, the vertical spreading of the images does not indicate the axial variation of the wave, but rather, it was introduced solely to conveniently organize the single-shot images in ways that would not overlap while rendering a sense of the cycle-

to-cycle variation of the local structure of the detonation wave. Figure 2.60b shows an instantaneous case where wave was captured within the field of view. Finally, Figure 2.60c shows the distribution of CO_2 thermal emission across the average detonation cycle collected from all instantaneous measurements after synchronization with the wave.

Chapter 3

Computational Activities

3.1 Overview

Rotating detonation engines (RDEs) are considered a viable approach to increasing the efficiency of combustion-based propulsion applications [32], such as rocket engines [33, 34], augmentors [35, 36] and aircraft and stationary gas turbines [37, 38, 39, 40, 41, 42]. In order to practically realize such detonation-based devices, it's necessary to gain an understanding of the detonation physics in non-ideal mixtures, and the performance of a practical RDE geometry - standard Axial Air Inlet (AAI-1) - due to varying injector dynamics and operating conditions. The canonical study involves the effect of mixture preburning on the detonation strength and shock-reaction coupling through an arbitrary mixture of hydrogen/air through a channel configuration. The full-scale AAI-1 system is employed to study the effect of mass flow rate on a rotating detonation combustor, specifically with regard to RDE mixing, operation, and performance in the presence of non-idealities (such as deflagration). In order to study these large-scale systems with detailed chemical kinetics, a GPU-accelerated compressible flow solver was developed to perform these calculations under the requirement of large-scale meshes and complex chemical mechanisms. These aspects of the research are discussed in the current section.

3.2 Mixture Preburning Effects on Detonation Wave Propagation

3.2.1 Introduction

In RDEs, the aerodynamically-driven turbulent mixing is always imperfect, leading to a stratified fuel-air mixture that is processed by the detonation wave. In practical systems, this variability in the level of mixing can critically affect the detonation wave. For instance, typical wave velocities are considerably lower than the Chapman-Jouguet (CJ) speed [43, 32, 44], which is partially caused by reduced heat release behind the shock wave. While different mechanisms for this reduction have been postulated [45, 46, 47], one main cause is so-called parasitic combustion [48, 46, 49]. In this regime, in addition to incomplete mixing, interaction with product gases from the previous cycle can lead to premature deflagration and heat release. For instance, Chacon et al. [50] found two distinct regions of deflagration: 1) recirculation of product gases trapped near the inlet due to injector design, and 2) a contact burning

region caused by mixing between product gases and incoming fresh gases (preburning effect). The former flameholding feature is not universal, but depends on the injector configuration used [51]. The latter preburning mechanism is the focus of the present study.

Numerical studies of full-scale RDE systems have suggested that up to 35-50% preburning of the fuel-oxidizer mixture is prevalent within the combustor [49, 52]. Detonation waves in RDEs are structurally different from ideal premixed waves [53]. Due to incomplete mixing, flow property variations can lead to a weaker shock wave, which in turn lengthens the induction zone. A delayed heat release profile moves the thermal choke further behind the wave front, leading to reduced wave speeds. In discrete injection systems, such wave structure may occupy the entire inter-injector distance [47] with multiple compression-expansion waves present in the induction zone. If deflagrated products are present ahead of the wave, this further weakens the shock and may even cause the reaction layer to detach. For instance, Fig. 3.1 shows an instantaneous image from a full system calculation for a hydrogen-air system [38]. Here, it is seen that although the detonation wave is followed by a temperature change, there are regions ahead of the wave (especially near the bottom of the domain) where temperature is rising despite not yet being processed by the shock wave. In practical RDEs, this weakening results in higher fraction of heat release in the deflagration mode (lower pressure, volumetrically distributed) rather than the detonation mode (higher pressure, compact region). Since detonation combustors are not optimized for deflagrative heat release, even with complete fuel consumption, the net efficiency may become lower than conventional deflagrative combustors.

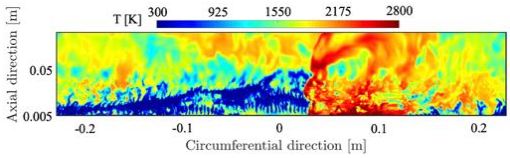

Figure 3.1: Snapshot of temperature profile from a three-dimensional full-system simulation shown as an unwrapped image at the mid-channel location. Reproduced from [38].

In the past, numerical and experimental studies have been conducted to understand the impact of stratification on detonation propagation [54, 55, 56, 57]. The mixture inhomogeneity results in a skewed detonation wave front, with irregular detonation cell structures [54] and diminished wave propagation velocities [57]. Spatial

inhomogeneity has been previously studied through one- and two-dimensional numerical simulations with single-step Arrhenius chemical kinetics by introducing a detonation wave to discrete reactive layers and squares, respectively [58]. With sufficiently inhomogeneous mixtures, where the spacing between successive reactive zones is greater than the reaction zone length, a "super-CJ" wave behavior is observed, with propagation speeds 15% higher than the CJ speed of a homogeneous mixture [59]. Discretely placed fuel sources thus act as concentrated pockets of energy release, and enforce a nonequilibrium state for the detonation wave.

With this background, the focus of this study is to isolate the effect of preburning on detonation propagation. For this purpose, a canonical flow configuration with quiescent initial flow but stratification of fuel-air mixture is considered. Based on prior work that considers only the role of stratification [60], the current work introduces the effect of preburning by imposing deflagration ahead of the wave. Detailed multi-step kinetics are used to study the evolution of the shock-driven combustion process. Specific operating parameters are obtained from full-scale RDE calculations [38, 49].

3.2.2 Simulation configuration and numerical approach

To replicate the wave structure in a practical RDE geometry, a canonical channel geometry of length 14 cm, width 7.6 mm, and height 6.25 cm is modeled as shown in Fig. 3.2. The height of the channel corresponds to the characteristic large length scale, L_{char}, within the domain. As an extension of past studies of Prakash et al. [53], the operating pressure of half the atmospheric condition with background air is used. The channel is confined with walls in the stream normal and spanwise direction, and the right boundary is set as an outflow. The inflow boundary condition is prescribed by a sampled right-running, well-developed, three-dimensional detonation wave. The grid for the three-dimensional geometry consists of 1) a uniform resolution core region and 2) a near-wall region. A near-wall region in the stream normal and spanwise directions contain clustered cells to properly resolve the boundary layer. Note that the near-wall regions are not included in the analysis, but the higher resolution is maintained to ensure that non-physical flow is not developed. This results in a total of 303 million cells, with $2800 \times 858 \times 126$ points in the x, y and z directions, respectively. Within the uniform core region, $\Delta y = \Delta z = 75$ μm, and $\Delta x = 50$ μm. The near-wall region is characterized by $\Delta y = \Delta z = 3.2$-$74.7$ μm. The clustered grid near the wall extends up to 435 y^+, or 0.261 mm, from the wall, where one y^+ is 0.6 μm. The length scale of interest is the induction length ℓ, which, for stoichiometric hydrogen-air detonation

at these operating conditions, is analytically given by 398 μm. Thus, approximately 6-8 grid points are used to resolve the induction length.

The range of equivalence ratios is set to be between 0.75 and 1.5, which is based on full-system RDE calculations [49]. Fuel-air stratification is introduced in the form of patches of varying equivalence ratios sampled from a model energy spectrum as per the methods of Ref. [61, 62]. An integral length scale is used as an input to create a corresponding homogeneous isotropic distribution with no mean gradient present. In this sense, this study is different from prior detonation studies with concentration gradients [63, 57]. In the selection of conditions for this study, a study of a full-scale hydrogen-air RDE with axial air inlet is utilized [38]. An integral length scale of 4.3 mm, extracted from the full-scale RDE data, is applied to the scalar energy spectrum function. Note that this length scale is roughly 10 times the induction length of an ideal detonation under these conditions. The resulting fuel-air distribution in terms of equivalence ratio is shown in Fig. 3.2.

From the three-dimensional RDE data, a one-dimensional profile along an azimuthal path at the mid-channel location and 2 cm height from the injectors is obtained. The profile is temporally-averaged about the wave front location. Data was collected at a height identified from mixing analysis performed by Sato et al. [38] as a location strongly affected by parasitic combustion due to recirculation zones and injector dynamics. Thus, the region was characterized by reduced detonation strength due to mixture inhomogeneity and preburning. Figure 3.3 shows this nominal profile along the azimuthal or circumferential direction. It is seen that the peak in pressure is reached close to $\bar{x} = 0$, which defines the location of the detonation wave. The temperature profile progressively decreases, which indicates that fresh gases at a lower temperature are entering this region. However, at $\overline{x} > 0.7$, temperature begins to increase even though the pressure profile observes either nearly constant or slightly decaying behavior. This is the region of deflagration, where autoignition of pockets of fuel and air mixed with product gases from previous cycle has initiated. The parameters for the current study are extracted from the region $\bar{x} = 0.7 - 1$.

To introduce the preburning effect, the following procedure is used. Based on the local equivalence ratio shown in Fig. 3.2, a corresponding equilibrium solution based on deflagration at constant pressure is obtained. The species composition at each point in the computational domain is then updated towards this equilibrium:

$$Y_{pb}(\boldsymbol{x}, 0) = Y(\boldsymbol{x}, 0) + f\left(Y_{eq}(\boldsymbol{x}) - Y(\boldsymbol{x}, 0)\right), \tag{3.1}$$

where Y_{eq} and Y_{pb} denotes the equilibrium and partially-burnt compositions, respec-

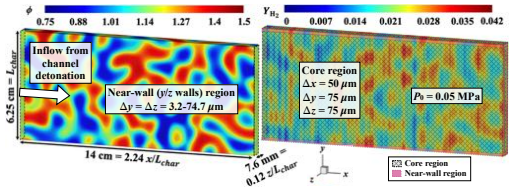

Figure 3.2: (Left) Contour of local equivalence ratio and (right) H_2 mass fraction along with description of the three-dimensional channel domain for a preburnt mixture with integral length scale of 4.3 mm. The uniform core and near-wall (y/z walls) grid regions are denoted in the right image.

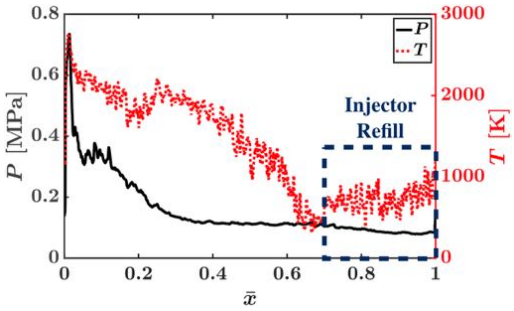

Figure 3.3: Temporally-averaged (about the wave front location) pressure and temperature profiles from the axial air inlet full-scale RDE simulations unwrapped into a one-dimensional profile as a function of normalized azimuthal distance, reproduced from [38].

tively, corresponding to the initial fuel mass fractions $Y(\boldsymbol{x}, 0)$ at a particular spatial location. Here. f is the preburning ratio, a fractional measure of deflagration.

In order to associate f to the local composition, the preburning ratio is defined using a progress variable $c = Y_{H_2O} + Y_{OH}$. Thus, it follows that f can be defined as a ratio of the local progress variable to its value at equilibrium as:

$$f = \frac{Y_{H_2O} + Y_{OH}}{\left[Y_{H_2O} + Y_{OH}\right]_{eq}} = \frac{c}{c_{eq}} \tag{3.2}$$

From the full-scale RDE data described in Fig. 3.3, the distribution of f is shown in Fig.3.4. It is seen that f has a high degree of linear correlation with the normalized temperature. This linear relation shows that data in this region is dominated by constant pressure deflagration. From the RDE data of a small number of detonation

cycles, a short-time averaged profile of f along the direction of wave propagation is obtained. The short time average is used to ensure that significant fluctuations in equivalence ratio is not present, in order to preserve the homogeneous initial conditions. The region from $\bar{x} = 0.7 - 1$ from the full-scale RDE (Fig. 3.3) represents a length equal to 0.14 cm.

This directional profile of f from $\bar{x} = 0.7 - 1$ is flipped then imposed in the streamwise direction on the initial condition given in Fig. 3.2, along with Eq. 3.1, to obtain the preburning-based initial condition that is also shown in Fig. 3.2. As a result, the profile of f at $\bar{x} = 1.0$ is applied at the entrance to the channel and the profile at $\bar{x} = 0.7$ location is at the exit of the channel. The preburning ratio varies in the streamwise direction, and is homogeneous in the stream normal directions. Note that the wall confinement and three-dimensionality of the flow is necessary to ensure propagation of triple points along the detonation front. Furthermore, the mixture within the channel geometry is allowed to burn as the detonation wave inflow travels through the domain. Consequently, the mixture near the exit of the channel (with a preburning ratio corresponding to $\bar{x} = 0.7$) continues to burn until the detonation wave arrives at this location in the channel, thereby increasing the local level of burning with time. Because the detonation wave travels at a finite speed similar to the RDE system, time for deflagration is roughly constant at each streamwise location. No diffusion-based flames are established during the burning process as the time-scale of their development will be much longer than the time taken for the shock to pass through the domain.

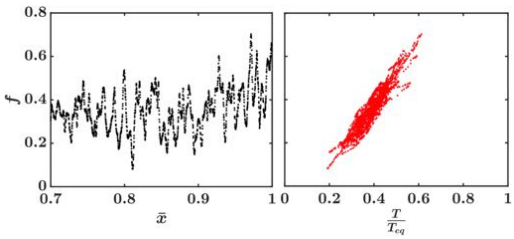

Figure 3.4: (Left) Preburning ratio f from the injector refill region and (right) correlation of preburning ratio with local temperature to equilibrium temperature for the local composition.

A direct numerical simulation (DNS) approach is applied to study the detonation wave structure in canonical systems. The governing equations of fluid flow consist of mass, momentum, and energy conservation equations supplemented by species

conservation equations that incorporate chemical reactions. The system of equations is closed using the ideal gas equation of state.

These governing equations are implemented in an in-house compressible flow solver, UTCOMP. This solver has been extensively validated in the past for a variety of shock-containing flows including scramjet isolators [64, 65], scramjet combustors [66], nonequilibrium flows [67] and detonating flows [53]. The solver utilizes a structured grid configuration with a cell-centered, collocated variable arrangement. A 5^{th} order weighted essentially non-oscillatory (WENO) scheme is used for computing the non-linear convective fluxes [68] and the non-linear scalar terms are calculated using a quadratic upstream interpolation for convective kinematics (QUICK) scheme [69]. A 4^{th} order central scheme is used to calculate the diffusion terms, used to capture the large-scale turbulent structures in the post-detonation region. Explicit time-stepping is performed using a 4^{th} order Runge-Kutta scheme for the temporal discretization. Molecular transport is not included within these simulations as the primary scope of this work is detonaton propagation through an inhomogeneous mixture. The composition and distribution of the inhomogeneous mixture is postulated from RDE data [38] and used as the initial condition.

The solver is parallelized using MPI-based domain decomposition and linear scalability has been demonstrated up to 65,000 cores for similar problems. The detailed chemistry is modeled for hydrogen-oxygen combustion with a nitrogen diluter using a 9-species 19-reaction chemical mechanism derived from Mueller et al. [70] using CHEMKIN-based subroutines [71]. The solver has been previously validated for hydrogen-air and hydrogen-oxygen detonation using one-, two- and three-dimensional canonical cases [53].

In a confined channel of equivalent cross-section filled with a homogeneous stoichiometric hydrogen-air mixture, a fully-developed detonation wave is created and sampled as a three-dimensional time-varying field to be used as the inflow.

3.2.3 Results and discussion

3.2.3.1 General behavior

As the detonation wave travels through the stratified mixture from left to right, it exhibits a nearly steady behavior shown in Fig. 3.5. The wave front is marked by a thin shock region with a trailing reaction zone. Behind this reaction layer, the expansion waves originating from the triple points lead to the creation of both vortical structures

and a mixing region. The mixing region is sustained over significant length, and is finally dissipated by viscous forces. Ahead of the wave, density variations caused by the imposed f profile is seen manifesting as striations due to the streamwise-only variation of this quantity. Prior studies [60] have shown that the size of these vortices is related to the stratification length scale. Further, the generation of vortices is consistent with the complex shock structure seen in detonation waves passing over discrete injectors [53, 72].

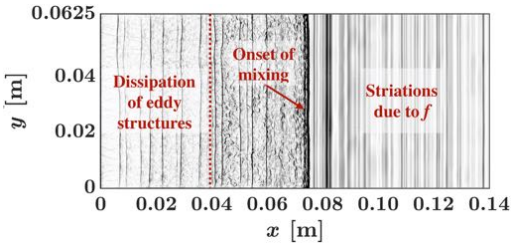

Figure 3.5: Contour of density gradient at the depth-wise mid-channel plane as the wave is midway through the channel, highlighting the reaction zone and turbulent mixing imposed by the detonation wave.

Figure 3.6 shows the pressure contour at an intermediate time, with an inset view of the triple points along the wave front. The peak pressure observed is roughly 0.8 MPa, which is less than half the ideal peak pressure of 1.7 MPa for an average equivalence ratio of 1.12 at the ambient conditions of 0.05 MPa and 300 K. More importantly, these peak pressures are observed only at triple points, with much lower values across the detonation front. Note that even after the detonation wave has passed through the region, the pressure variations still persist. This is due to the fact that the wave is traveling at supersonic speeds, while the pressure waves are relaxing at acoustic speed in the post-detonation gases. It is also seen that small amounts of hydrogen remains behind the wave, denoting some reduction in combustion efficiency even for this canonical case. In practical RDEs, this residual fuel-air mixture is found to deflagrate as it convects downstream.

A key quantitative measure of shock strength is its propagation velocity. Figure 3.7 illustrates the variation in wave speed measured locally across the entire simulation. The simulation domain is set up such that the strong homogeneous detonation wave enters from the left and progresses through the stratified mixture. It is seen that the wave velocity exhibits very large fluctuations with variations of up to nearly 500 m/s about the average over short segments of the domain. The instantaneous oscillations

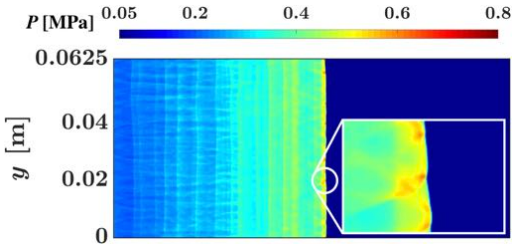

Figure 3.6: Contour of pressure at the depth-wise mid-channel plane as the wave is midway through the channel. A microscopic view of the triple point structure along the wave front is provided.

in wave velocity are due to changes in local composition and density. This "galloping" feature has been observed in most practical RDEs [32, 50]. The pressure profiles show that the shock front is nearly normal to the propagation direction, and is not as corrugated as seen in practical RDEs [43] given the lack of large scale turbulence found in full scale systems.

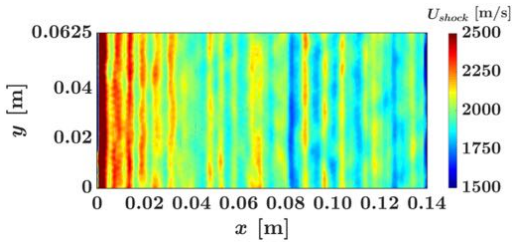

Figure 3.7: Contour of wave velocity at the depthwise mid-channel plane.

Figure 3.8 shows the streamnormal-averaged wave velocity as a function of axial position and the PDF of wave velocity within different regions of the domain. As seen in Fig. 3.7, there is a slow decay in propagation speed with streamwise distance. Regardless, the full computational domain PDF of wave velocity shows a large spread, with the most probable velocity close the CJ speed of 1960 m/s for this operating condition. The PDFs of velocity sampled in 2 cm wide sub-domains within the full domain highlights that the spread of velocities remain approximately unchanged over the different sub-domains at locations downstream. While there is considerable statistical variation, there is no clear trend in the peak of the PDF moving towards lower velocity values. Thus, the wave velocity exhibits sustained fluctuations but

constant wave propagation on an average in the latter part of the domain ($x > 0.08$ m). Note that while stratification can lead to slight increase in speeds due discrete energy source effects as noted by [58], the high observed wave speeds for the available reduced energy may be a consequence of the finite domain length. In other words, a quasi-steady state might not have been reached by the end of the computational domain. However, these results indicate that even in the absence of turbulence-induced wrinkling of detonation front, the wave behavior in this canonical system is similar to that of practical RDEs.

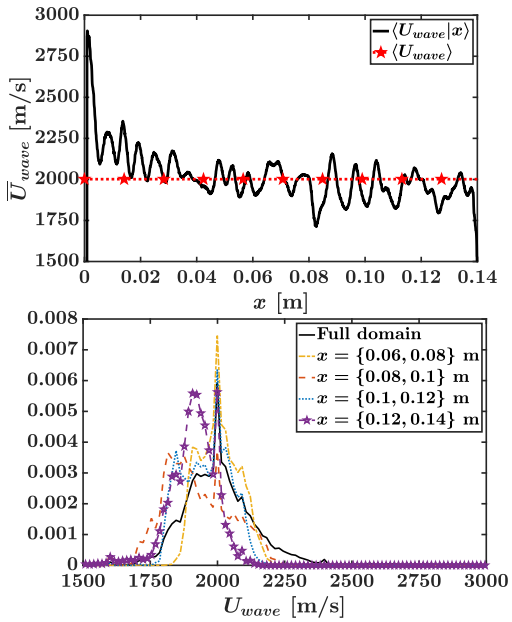

Figure 3.8: (Top) Wave velocity averaged in stream normal direction and (bottom) PDF of wave velocity within 2 cm sectors of the latter half of the domain compared to the PDF sampled from the entire domain.

3.2.3.2 Detonation structure

In order to gain insight into the detonation process across the wave, spatially and temporally-averaged one-dimensional profiles of properties across the wave front are provided in Fig. 3.9. The wave front location is tracked and a normal vector at every $\{y, z\}$ location on the wave front surface is determined. Thus, the shock front location

is assumed to be the same for each surface-normal vector. The one-dimensional profile extracted along this vector at each location across the front surface is then temporally-averaged to obtain a representative one-dimensional profile of properties across the detonation wave. The pressure profile shows interesting features. First, the pressure jump across the wave is much smaller than the theoretical expectation of ∼34x (from 0.05 MPa to 1.7 MPa), with an observed pressure jump of only ∼8x to 0.5 MPa. The initial shock wave is roughly 200 μm in thickness, which provides compression to raise the fluid temperature by nearly 1000 K. Denoted by position A, the increase in temperature occurs simultaneously with shock compression. However, the subsequent heat release increases the temperature only by 600-700 K, indicating reduced heat release due to preburning. This effect is seen in the heat release plot, with a small positive heat release in the pre-shock region and a large negative heat release in the induction region followed by the combustion process leading to high energy release. Further, the heat release process, highlighted by position B, continues further away from the compression wave, with slow expansion of the gases, with the release rate still higher than the pre-shock preburning values. This delayed heat release is another source of efficiency loss, resulting in so-called commensal combustion or leakage process [50], whereby the energy release does not directly support the wave propagation process.

The statistical properties of the detonation front show a complex process (Fig. 3.10). First, it is seen that the normalized pressure and temperature fluctuations peak in the compression region associated with the shock. This indicates that as the wave propagates through the domain, there are large variations in the structure of the shock wave. This fluctuation is caused by the transverse motion of the triple points (Fig. 3.6) as well as the variations in the preburning ratio. The fluctuations for hydrogen mass fraction appear downstream of this region, in the post-combustion zone. This variation is merely caused by the changes in post-shock temperature and pressure that leads to reduced consumption of fuel. As seen in the average species mass fraction plot (Fig. 3.9), hydrogen is depleted near the induction zone, but appreciable fraction is still present far downstream. For comparison, the equilibrium mass fraction at stoichiometric condition for H_2 and 1000 K preburning temperature is approximately 0.0033, while nearly 3 times this mass fraction is found at distances of up to 1 cm behind the wave.

Finally, heat release rate per unit volume conditioned on pressure is shown in Fig. 3.11. The first notable feature is that high heat release rate is directly associated with higher pressure. Although lower heat release rate is possible at all pressures, the

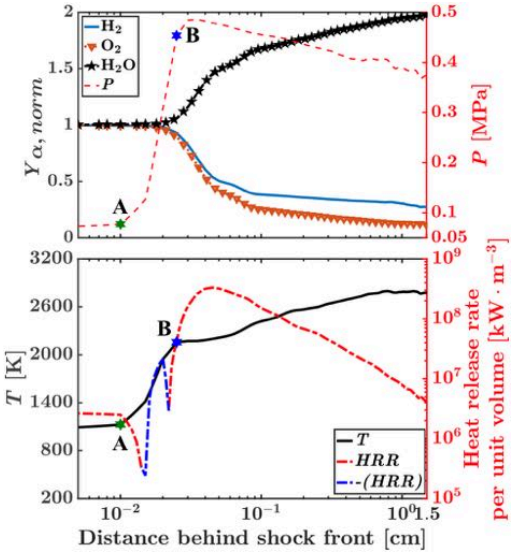

Figure 3.9: Spatially and temporally averaged one-dimensional profiles of properties across the detonation wave front. Similar positions behind the shock front between both profiles are marked by positions A and B.

shock-based compression is necessary to increase the compactness of the combustion process. However, the peak heat release does not occur at the highest pressure, which is also seen from Fig. 3.9. Furthermore, appreciable heat release continues to occur at a distance of 1 cm behind the wave (as noted above).

3.2.4 Conclusions

Practical RDEs exhibit combustion inefficiencies due to a number of factors including turbulence-induced wave front wrinkling, incomplete mixing, and premature deflagration or preburning. In this study, the preburning process is isolated by using a canonical system, where a prescribed preburning profile is used. A near-ideal detonation wave formed in a homogeneous and stoichiometric mixture is introduced into the domain with this stratified mixture and fixed preburning profile. Analysis of the wave propagation and detonation structure was conducted.

The detonation wave was found to propagate with a spread of speeds, indicating that the preburning of the mixture significantly affects the strength of the leading shock. The most probable speed was close to the CJ speed, but the standard deviation

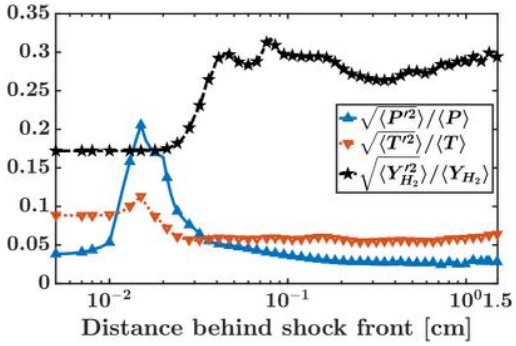

Figure 3.10: Normalized standard deviation of temperature, pressure, and hydrogen mass fraction across the detonation wave front.

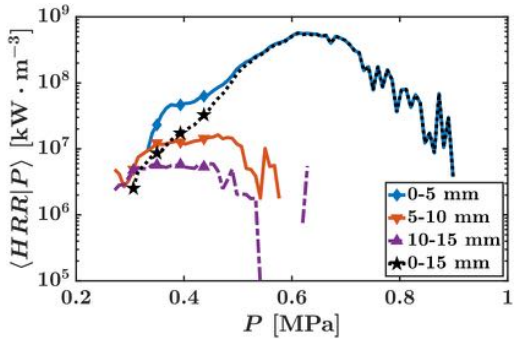

Figure 3.11: Conditional average of heat release rate per unit volume conditioned on pressure at different distance ranges behind the detonation wave front.

was ±15%, even for equivalence ratios variations that are small compared to practical RDEs. The detonation wave exhibited a complex structure, with a mixing region behind the propagating front where vortical structures of length scales comparable to the stratification length scale were created. Overall, the detonation structure was weaker, with even the triple points exhibiting lower peak pressures compared to expected theoretical values.

The shock weakening was directly related to the preburning of the fuel-air mixture. The initial compression was smaller than theoretical values, with average pressure increase of approximately 8 times the pre-shock pressure. As a result, the induction zone was much longer, leading to slower heat release extending far behind the shock front, where vortex-driven mixing enforced homogenization of fuel-air mixtures.

These results indicate an important connection between pre-shock deflagration and loss of efficiency. In general, to have a compact heat release zone, it is necessary to have a strong compression wave. Any reduction in peak pressure can adversely affect the heat release profile. The premature deflagration process directly weakens this shock front, leading to a slow and distributed heat release. There is considerable unburnt fuel downstream of the shock front. In other words, so-called parasitic combustion (deflagration ahead of wave) directly leads to commensal combustion (heat release far downstream of the wave), indicating that parasitic combustion is the root cause of loss of combustion efficiency. The fact that these features could be reproduced without significant turbulence in the system indicates that turbulence is more critical to the fuel-air mixing ahead of the shock rather than shock propagation itself.

3.3 GPU-based Implementation of OpenFOAM for Compressible, Shock-containing Flows

3.3.1 Introduction

Computational modeling has become essential in the design of complex reacting flow systems for a variety of applications [73, ?]. Combustion problems are multi-scale and multi-physics in nature, and the range of physics and experimental configurations that can be studied are often limited by the available computational resources. In this regard, the rapid increase in the processing power of high performance computing (HPC) machines has increased the complexity of multi-physics problems that are computationally feasible to solve. In order to further increase processing capacity, while maintaining a manageable energy footprint, there has been a shift towards heterogeneous architectures [74, 75]. Such HPC systems have specialized computing units (SCUs) in addition to conventional CPUs, but the vast majority of the computing capability resides in the SCU [76, 77]. The pre-Exascale leadership class machine, Summit, uses GPUs, a form of SCUs, to provide 95+% of the peak floating point operations (FLOPs), while Exascale machines are designed to be even more GPU-dominated. This trend of the largest supercomputers getting the majority of FLOPs from SCUs, and GPUs in particular, is expected to continue [78, 79, 80]. Thus to be able to benefit from the continual increase in computing power, which has steadily expanded the range of problems that can be studied computationally, academic codes need to utilize GPUs. Utilizing GPUs presents a new challenge, compared to conven-

tional MPI programming, and necessitates developing a new set CFD software that are capable of utilizing the new architecture. GPU computing is sufficiently different from traditional MPI programming, often making it necessary to completely write a new CFD software as opposed to adding GPU accelerated functions to an existing CFD framework.

The new GPU computing paradigm necessitates the use of a shift from MPI-based SIMD programming to MPI+X where X in the new additional programming model. This has spurred the adoption of GPU acceleration to a wide range of research codes [81, 82, 83, 84, 85, 86, 87] to allow for the utilization of the GPU resources. In the context of compressible flows, several GPU-accelerated algorithms have been developed for structured grids [88, 86, 89, 90, 91]. The challenges with GPU memory access [92] and branching logic is a factor limiting the adoption to GPUs to structured applications. This has greatly limited the ability to perform high-fidelity studies of complex geometries found in the laboratory scale as well as full scale systems. The study of complex geometries generally necessitates the need for handling unstructured meshes which poses an increased challenge on GPUs. GPU performance can be heavily impacted by how the data arranged in the GPU memory. For unstructured grids, and even more so for arbitrary order polynomials, there is difficulty in knowing the data layout *a priori*.

This limitation to structured meshes greatly limits the complexity of the geometries that can be studied. For shock containing and flows with turbulent boundary layers there is a need for both tetrahedral and hexahederal cells to both capture complex surfaces and improved numerical accuracy [93]. For this reason the current GPU implementation allows for polyhedral cells with an arbitrary number of faces. The complex curved geometries would prove difficult impossible to mesh effectively using only hexahederal cells. To the authors knowledge there are no GPU accelerated unstructured compressible finite volume codes developed to date and this code fills that capability gap, which is of particular importance due to the increasing demand to numerically study complex propulsion devices.

3.3.2 Governing Equations

The solved discussed herein is an extension of the solver UMdetFOAM which is design to study shock-containing reacting flows with complex geometries. UMdetFOAM was developed in-house by the advanced propulsion laboratory [94, 95, 96, 97] and utilizes openFoam to handle the generation of basic mesh information: area, centroid, cell

to face connectivity to name a few. The UMdetFOAM solver and OpenFOAM have been tested and validated against a wide range of problems [94, 95, 96, 97] including detonation engine and hypersonic applications. The governing equations used within UMdetFOAM will be outlined below.

The compressible reacting NSE is described by the following set of, mass, momentum, energy and species equations:

$$\frac{\partial \rho}{\partial t} + \frac{\partial \rho u_i}{\partial x_i} = 0, \tag{3.3}$$

$$\frac{\partial \rho u_j}{\partial t} + \frac{\partial u_i u_j \rho}{\partial x_i} = -\frac{\partial p}{\partial x_j} + \frac{\partial \tau_{ij}}{\partial x_j} \tag{3.4}$$

$$\frac{\partial \rho E}{\partial t} + \frac{\partial u_i \rho H}{\partial x_i} = \frac{\partial}{\partial x_j} \alpha \frac{\partial T}{\partial x_j} + \frac{\partial \tau_{ij} u_i}{\partial x_j}, \tag{3.5}$$

$$\frac{\partial \rho Y_j}{\partial t} + \frac{\partial u_i \rho Y_j}{\partial x_i} = \frac{\partial}{\partial x_i} \rho D \frac{\partial Y_j}{\partial x_i} + \dot{\omega}_j M_j, \tag{3.6}$$

$$\tau_{ij} = \frac{-2}{3} \mu \frac{\partial u_k}{x_k} \delta_{ij} + \mu \left(\frac{\partial u_j}{\partial x_i} + \frac{\partial u_i}{\partial x_j} \right), \tag{3.7}$$

$$E = \int_{T_0}^{T} C_p dT - \frac{p}{\rho} + \sum_{k=1}^{N} \Delta h^0_{f,k} Y_k + \frac{1}{2} u_i u_i, \tag{3.8}$$

where ρ, p T, u_i, Y_j are the density, pressure, temperature velocity in the $i-$th direction, and mass fraction of the $j-$th species. The gas properties Cp, μ and $\Delta h^0_{f,j}$ are the specific heat, dynamic viscosity, and enthalpy of formation for the $j-$th species. The reaction rate $\dot{\omega}_j$ term is give by,

$$\dot{\omega}_i = \sum_{k=1}^{N} \left(v''_{i,k} - v'_{i,k} \right) \left(\Pi_{f,k} - \Pi_{r,k} \right) \tag{3.9}$$

Details on discretization and numerical schemes will be presented in the following section.

The specific heat, enthalpy and specific heat ratio are all computed using NASA polynomials with the specific heat and specific heat ratio held constant below 298K.

The gas is treated as an ideal gases. The viscosity and thermal conductivity for each species is fit as a function of temperature and pressure to reduce computational cost.

To compute the species reaction rate, $\dot{\omega}_j$, operator splitting it employed. The chemical time scale is assumed to be sufficiently smaller than the flow time scales and so the flow can be considered frozen during the computation of the chemical kinetics. The change in species due to reactions is governed by,

$$\dot{\omega}_i = \sum_{k=1}^{N} \left(v_{i,k}^{''} - v_{i,k}^{'} \right) \left(\Pi_{f,k} - \Pi_{r,k} \right) \tag{3.10}$$

where the forward and reverse stoichiometric coefficients are given by $v_{i,k}^{''}$, $v_{i,k}^{'}$ and the forward and reverse molar production rate are given by $\Pi_{f,k}$, $\Pi_{f,k}$. The forward rate constant is computed by the Arrhenius expression and the reverse rate constant is computed by the forward and equilibrium rate constant. The forward and reverse rate constants as well as computation of net molar production rate are computed in matrix form, the details of this reformulation are presented by Barwey and Raman [98]. The importance of this reformulation will be discussed in detail in section ***, in brief GPUs are more efficient if the computation can be cast as a matrix multiplication.

3.3.3 Numerical Methods

The numerical discretization of the governing equations will be discussed in detail herein. The focus will be on discretization of the viscous terms, inviscid terms and time integration. Second order accuracy is achieved in each of the three components to result in an overall accuracy of second order. The viscous terms utilize a Kurganov, Noelle, and Petrova (KNP) [99] formulation, while the inviscid terms utilize limited linear interpolation and an approximate Riemann solver and an explicit Runge-Kutta time integration scheme.

The evaluation of inviscid flux will be discussed first as it is of particular concerns for shock and detonation dominated flows as representation of the shock is key to an accurate representation of the flow. Approximate Riemann solvers provide the capability to handle discontinuities with near minimal dissipation without the prohibitive computational cost of exact Riemann solvers. There are a range of different approximate Riemann solvers within the literature. The Harten-Lax-van Leer-Contact (HLLC) approximate Riemann solver [100] is utilized for it's low computational cost

and ability to model both Riemann waves as well as the contact wave. The form of the invsicid flux, F, as well as the HLLC flux are given below,

$$U = \begin{bmatrix} \rho \\ U \\ e \\ Y_i \end{bmatrix}, Q = \begin{bmatrix} \rho \\ \rho U \\ \rho E \\ \rho Y_i \end{bmatrix}, F = \begin{bmatrix} \rho U \\ \rho U^2 \\ \rho U e + U p \\ \rho U Y_i \end{bmatrix} \tag{3.11}$$

$$F_{i+\frac{1}{2}} = \begin{bmatrix} F(U_L) & : S_L < 0 \\ F(U_L) + S_L^*(Q_L^* - Q_L) & : S_L > 0 \ \& \ S^* > 0 \\ F(U_R) + S_R^*(Q_R^* - Q_R) & : S^* < 0 \ \& \ S_R > 0 \\ F(U_L) & : S_R > 0 \end{bmatrix} \tag{3.12}$$

where F, U and Q are the inviscid Flux, primitive variable set and conservative variable set. The intermediate conservative state, Q^* is given by:

$$Q_k^* = \rho \frac{S_k - u_k}{S_k - S^*} \begin{bmatrix} \rho 1 \\ \rho S^* \\ \rho \frac{E_k}{\rho} + (S^* - u_k)\left(S^* + \frac{\rho}{\rho(S_k - u_k)}\right) \\ \rho Y_i \end{bmatrix} \tag{3.13}$$

where, S is the left or right Riemann wave speed and S^* is the contact wave speed. The contact wave speed S is computed using the Einfeldt [101] approximation for the wave speeds

$$\begin{aligned} \tilde{u} &= \frac{\sqrt{\rho_L} u_R + \sqrt{\rho_R} u_R}{\sqrt{\rho_L} + \sqrt{\rho_R}} \\ \tilde{a} &= \sqrt{(\gamma - 1)(\tilde{H} - \frac{1}{2}\tilde{u}^2)} \\ \tilde{H} &= \frac{\sqrt{\rho_L} H_R + \sqrt{\rho_R} H_R}{\sqrt{\rho_L} + \sqrt{\rho_R}} \\ S_L &= \tilde{u} - \tilde{a} \\ S_R &= \tilde{u} + \tilde{a} \end{aligned} \tag{3.14}$$

The left L and right R values are obtained using a limited linear interpolation of face values. Within openFoam each face has an owner and neighbour cell referenced to as the positive, P and negative, N, cell respectively. This makes no assumption about the order of polygon or cell ordering. The three-dimensional representation and equivalent one-dimensional projection are presented in Figure 3.12. It is worth noting that the one-dimensional projection is not guaranteed to pass through the center of the face and represents a source of numerical errors for highly skewed cells [102, 103].

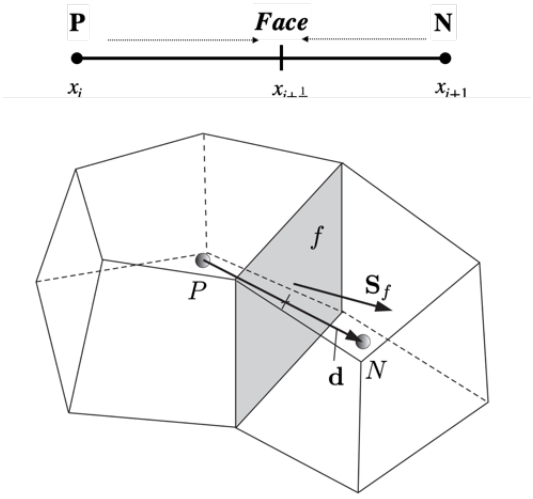

Figure 3.12: Schematic of the stencil for the flux evaluation across a face between two arbitrary closed polygons in three-dimensions as well as the equivalent one-dimensional projection. Where **P** and **N** refer to the positive and negative side of the face respectively.

$$q_{pos} = \phi_{i+\frac{1}{2}} \nabla q \cdot \vec{n} + q_{owner} \tag{3.15}$$

$$q_{neg} = \phi_{i+\frac{1}{2}} \nabla q \cdot -\vec{n} + q_{neighbour} \tag{3.16}$$

where, q is the variable being interpolated, ϕ is the limiter and $\vec{n}$ is the normal vector going from owner to neighbour cell. A minMmod limiter utilized in the presence of shocks and discontinuities to maintain a non-oscillatory solution. A non-oscillatory solution is of increased importance for problems containing detonations or premixed

flame fronts as both represent discontinuities that are impacted by artificial increase in mixing due to oscillations. The minMod limiter is given by,

$$\begin{aligned} \phi_{i+\frac{1}{2}} &= max\left(0, min\left(r\right)\right) \\ r &= \frac{q_i - q_{i-1}}{q_{i+1} - q_i} \end{aligned} \tag{3.17}$$

The variables, q, can take the form of the primitive, U or conservative, U variable set are appropriate for a second order accurate code. Special care must be taken when applying limiting to the passive scalars if conservative interpolation is used. This is of particular importance when solving the reacting Navier Stokes equations as there are an additional N passive scalar transport equations, species mass fraction. The issue of utilizing conservative variables and passive scalars is discussed by Toro [104] and can result in the sum of mass fractions diverging from unity. This occurs as the limiter may be difference between the passive scalars and density resulting in a different effective contact speed between the passive scalars. It is worth noting that species concentration can vary rapidly both in burning regions and in mixing regions resulting in application of the limiting not just in the presence of shock waves. The significance of these errors for reacting flow problems well be discussed. Utilizing primitive interpolation ensures that all the passive scalars are transported at the same speed, resolving the mass fraction issue. The use of primitive is used for all problems presented herein. The use of primitive variables does come with the limitation that the maximum order that can be achieved is second for unsteady problems.

The impact of limiting conservative and primitive variables is demonstrated by using examining a high speed region of O_2 within a box of quiescent N_2. The percent error in mass fraction for both the use of primitive and conservative interpolation are shown in Figure3.13. The primitive interpolation shows no errors the conservative interpolation shows up to 5% error in some regions. This deviation in total mass fraction is non-physical and adds complexity and in determining the mixture composition which is critical for reacting flows as reaction rates may be sensitive to species concentration.

Gradients are approximated by,

$$\frac{\partial q}{\partial x_i} \approx \frac{1}{V} \sum_j S_f q_f \tag{3.18}$$

where S_f and q_f are the face area and linearly interpolated face value. The

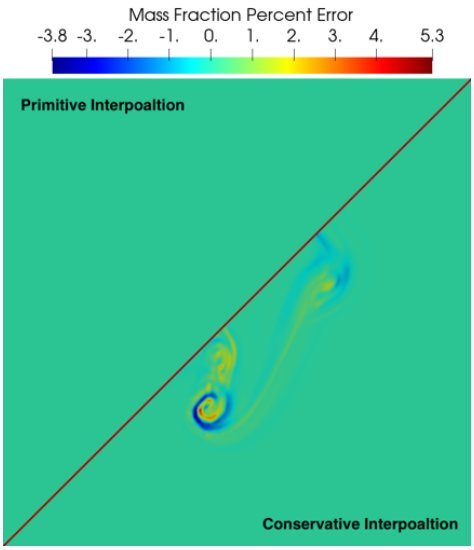

Figure 3.13: Multi-species advection with primitive interpolation(left) and conservative interpolation (right). Conservative interpolation show errors in excess of 5% in the sum of the mass fraction. Initial condition is a square region of N2 travelling at (??, ??) in a background of quiescent O2.

accuracy of the divergence theorem on a range of different grids is addressed by Syrakos et. al. [105] and found that order of accuracy second so long as the skewness diminishes with refinement.

The viscous terms are given as,

$$\frac{\partial}{\partial x_j}\begin{bmatrix} 0 \\ \tau_{ij} \\ \alpha\frac{\partial T}{\partial x_j} + \tau_{ij}u_i \\ \rho D_l \frac{\partial Y_l}{\partial x_j} \end{bmatrix} \tag{3.19}$$

a central, second order accurate, approximation of the gradient is used for the evaluation of τ_{ij}, $\frac{\partial T}{\partial x_j}$ and $D_l\rho\frac{\partial Y_l}{\partial x_j}$. The evaluation of $\frac{\partial \tau_{ij}u_i}{\partial x_j}$ utilizes the Kuganov-Noelle-Petrova (KNP) formulation [99].

The governing equations utilizes a Runge-Kutta scheme for explicit time integration of the fluid system.

$$
\begin{aligned}
Q(t^{\frac{1}{2}}) &= Q(t^0) + \frac{1}{2}\Delta t F(Q(t^0)) \\
Q(t^1) &= Q(t^0) + \Delta t F(Q(t^{\frac{1}{2}}))
\end{aligned}
\tag{3.20}
$$

3.3.4 GPU Acceleration

As previously discussed GPUs show improvements in dollars per FLOP as well Watts per FLOP compared to CPUs making them a key part of exa-scale computing as well an increasing prevalence in new super-computers. While GPUs have the potential to outperform CPUs algorithmic choices can completely negate any benefit the GPUs would provide over CPUs. To realize the performance potential of GPUs the computationally intensive kernels must have a high arithmetic intensity or be designed such as to have optimal data access patterns. For Navier-Stokes equation the reconstruction and flux evaluation represent some of most computationally expensive kernels however these operations have low arithmetic intensity, i.e. how many operations do they perform per memory access (or is it byte of data check). If the mesh is unstructured the data access pattern is likely to be non-sequential. These two factors make extracting performance from GPUs for unstructured meshes and Navier-Stokes computation. One possible way to deal with this is to utilize a structured grid which allows for algorithmic changes to improve memory access patterns. For many engineering applications utilizing a structured grid is not possible. For Reacting Multi-Species Navier-Stokes the computation of chemistry, temperature and other mixture properties becomes expensive. These operations are all local to a single cell and thus the memory access does not depend on if the grid is structured on un-structured. This shift in the kernels that represent the computational expensive allows for the effective utilization of GPUs for solving the reacting Navier-Stokes.

A diagram of the code is presented in Figure 3.14. The code is broken into two major components, the flux computation and chemistry computation. The chemistry computation is completely local, needing only cell average data, and so performed entirely on the GPU. The Flux computation is split between both the CPU and GPU, the CPU is only responsible for handling MPI communication between processors and evaluation of external boundary conditions.

Unlike with CPUs computations a discussion of the layout of the data is a key component when discussing GPU computations as the movement and access of data can be the limiting factor for GPUs. The data layout within UMdetFoam is dominated

by the need to allow for arbitrary polynomials to accommodate complex geometries. For this reason little can be assumed about the relationship in memory between adjacent cells. The data is instead stored as list of all faces allowing for at least half of data to be sequential when computing the approximate Riemann solver. As previously mentioned the evolution of the reaction rate ODE and as well as species property evaluation are purely local and so independent of the grid type. A detailed discussion of how reaction rates were formulated as a series of matrix operations is presented by Barwey and Ramann []. The reformulation of both the computation and data structure allows for the use of highly optimized matrix operation package, cuBLAS [], to be utilized for the most computationally expensive portion of the code.

The convective system was presented in sec. 2 as well as the method for discretization. The evaluation of any cell can be thought of as a series of sequential operators. The series of operations is, gradient, reconstruction, flux evaluation, surface integration and time advancement, evaluation of some thermodynamic properties is left out for brevity. Each of these steps is a separate GPU and completed for all cells/faces before going to the next operator.

This framework provides a set of GPU accelerated functions to replace the computationally demanding OpenFOAM and Cantera calls found within UMdetFoam which can be mapped directly to the computationally demanding calls in most compressible FVM solvers. While the most computationally expensive operations are reconstruction and flux evaluation porting only these functions to the GPU resulted in minimal acceleration. This is due to a combination of Amdahl's law as well as the added cost of copying data between the CPU and GPU. For this reason all possible operations are ported to the GPU to minimize the data transfer. Given that OpenFOAM and Cantera are distinct programs the operations associated with each are thought of as separate modules of the library however both modules are necessary even for non-reacting problems. A general schematic of the library layout is given in Figure 1 outlining the core components within each module as well as well as the operations that the library does not support. Currently the library does not perform MPI communication or the application of external boundary conditions both of which must still be handled by OpenFOAM.

The surface integration takes a weighted sum of all the face values of a cell to get an estimate of the cell averaged value. This summation can result in multiple faces accessing and modifying a cell value simultaneously and the contribution of some faces to be over written.

A computationally advantageous way to deal with this problem is an algorithmic

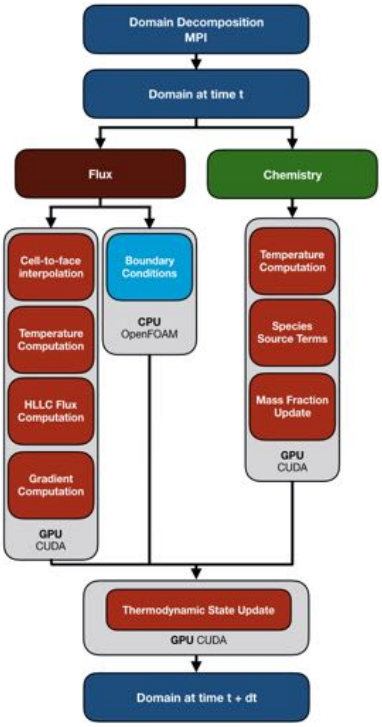

Figure 3.14: A schematic for UMdetFoam showing the main components of the convective and reactive system and what computing resource they utilize.

change that requires reorienting the data so it is structured as 2D array with cells in one dimensions and faces associated with each cell in the other dimension. This would allow for the reduction to integration to be performed as a reduction. However this puts very strict requirements on the data structure.

For this reason it was chosen to not force a given data layout and implementing a blocking operation. This was achieved by using an atomic addition operation, this is not as efficient as an algorithmic change and can lead to threads waiting.

3.3.5 Validation and Results

3.3.5.1 Validation

Several validations cases are presented below to check the implementation of the numerics within UMdetFoam. Two common inviscid test cases, SOD shock tube

problem and the curved shock problem will be presented below.

The UMdetFoam solution is compared to the Riemann solution for the equivalent jump condition with constant specific heat ratio. The results show good agreement with the analytical with only a slight discrepancy due to numerical diffusion at the jump condition smearing the jump over several cells. Not shown the error between the Riemann solution and the code shows second order convergence with increasing resolution.

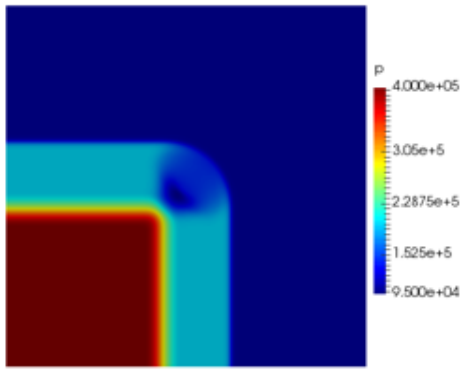

Figure 3.15: Expansion of a high pressure cube into a low pressure region, regions where the expansion have not interacted the problem is equivalent to a 1D SOD problem and is compared to the Riemann solution for the equivalent 1D problem.

3.3.5.2 Example Problems

High-speed propulsion devices, such as rotating detonation engines (RDEs) and scramjets, contain a complex, turbulent reacting multi-physics flows with a range of length and time scales. Limited accessibility for optical equipment and flow-field diagnostics constrain knowledge of the turbulence and anomalies inside these combustors and the phenomena which lend to their stability and optimal system performance. Numerical simulations are effective in gaining detailed insight into high-dimensional physics of reacting flows. Namely, they are well-suited for GPUs due to the complex chemistry mechanisms (hydrocarbons, syngas) and variable gas properties. Computational modeling and simulation for airborne and hypersonic applications is an active area of research, and ideal use case for this software.

The solver numerical scheme for the solver are presented above in detail. In brief, the solver utilizes an HLLC-MUSCL approximate Riemann solver with a KNP formulation for the viscous terms and second order Runge-Kutta time integration scheme. Gas properties were computed using NASA polynomial curve fits, which are some of the more arithmetically intense computations.

The rotating detonation rocket engine (RDRE) from Air Force Research Laboratory (AFRL) is numerically studied using the GPU-accelerated solver. Here, fuel and oxidizer enter from the bottom plenums through discrete injectors into a narrow annular combustion chamber. An azimuthally-traveling detonation wave releases chemical energy as it processes a fresh mixture of reactant gases, compressing and accelerating the post-reaction gases. A detonation wave is comprised of a leading shock wave and chemical reaction zone that leads to heat release and oxidation of fuel-oxidizer mixture to products. This chemical heat release sustains the shock wave. While the shock wave is nominally treated as a discontinuity, the chemical reaction is spatially-distributed and can extend over a few millimeters under practical operating conditions. The device is mixing-limited, and the mixing process and development of turbulence is not complete, leading to combustor operation with weak detonations, secondary combustion processes (deflagration), and flow dynamics that can be detrimental to the efficiency and stability of the system.

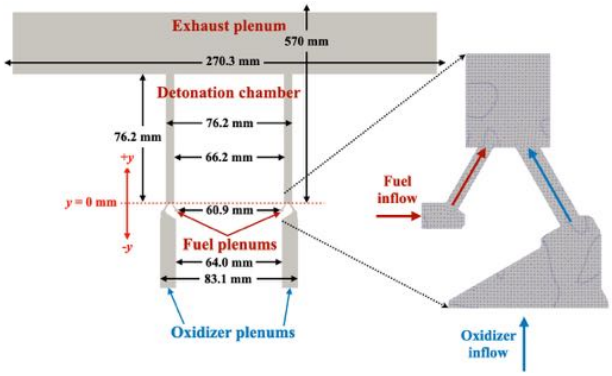

Figure 3.16: Schematic of numerical RDRE representation with primary dimensions.

In this geometry, the fuel and oxidizer injector have throat-to-channel area ratios of 0.031 and 0.078, respectively, with a 5 mm annular gap. The combustion chamber is square with a outer diameter and axial length of 76.2 mm. Methane and oxygen gas are fed through 72 pairs of fuel-oxidizer injectors. The 12 species, 38 reactions-based

FFCMy-12 mechanism (R. Xu and H. Wang, personal communication, January 2019) [106] is used to model the chemical reactions. The simulated flow path consists of the reactant plenums, the injectors and combustion chamber, and a large exhaust plenum. The geometry is numerically represented through primarily hexahedral cells radially aligned with the center of the annulus. This results in 118 million cells with a resolution of 100 microns near the injectors and combustion chamber. The mesh resolution is progressively relaxed to 200 microns in the reactant feed plenums and beyond 400 microns in the exhaust plenum. Figure 3.16 displays the computational domain of the RDRE geometry with key dimensions and components.

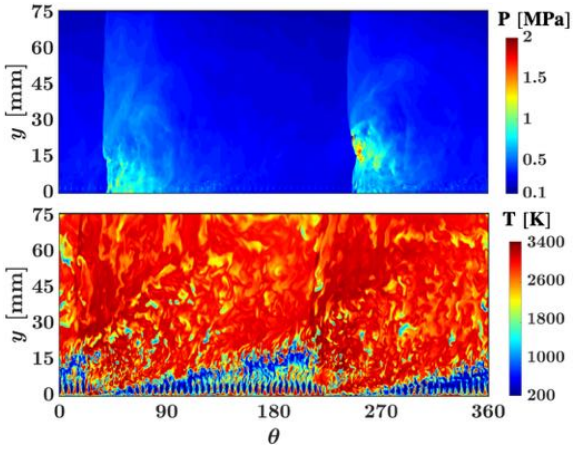

Figure 3.17: Projection of RDRE combustion chamber flow field pressure and temperature along the midchannel plane onto two dimensions, highlighting the two co-rotating detonation waves.

The flow field at the midchannel RDRE plane is displayed as a projection onto two dimensions in Fig. 3.17. The operating condition is the nominal total flow rate of 267 g/s at an equivalence ratio of 1.16. A mass flow rate boundary condition is enforced on the feed plenum inflows and the feed plenum pressures are initially matched with the experimental values and allowed to stabilize as the plenums pressurize. Under steady-state operation, two co-rotating detonation waves traveling at 1357 m/s are established. The detonation wave stands vertically, with a broad reaction zone and a triangular injector refresh profile. The flow chokes at the exit of the combustion chamber due to pressure rise of detonation. The injectors recover quickly after the detonation wave passage because of the high feed pressures and impinging

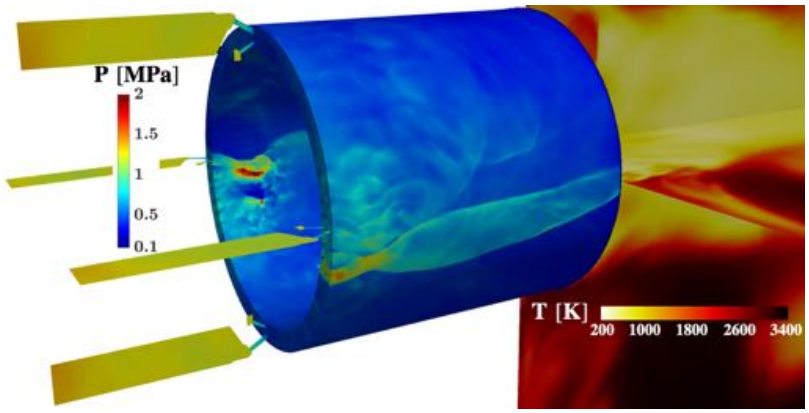

Figure 3.18: Composite view of the plenum and combustion chamber pressure profile and exit temperature profile of the RDRE under steady-state operation.

rocket-style micronozzle injectors. In between the detonation waves, the partially-burnt gases oxidize through a slow and distributed deflagrative process. A composite snapshot of pressure and temperature showing the detonation wave structure and exit temperature profile is illustrated in Fig. 3.18.

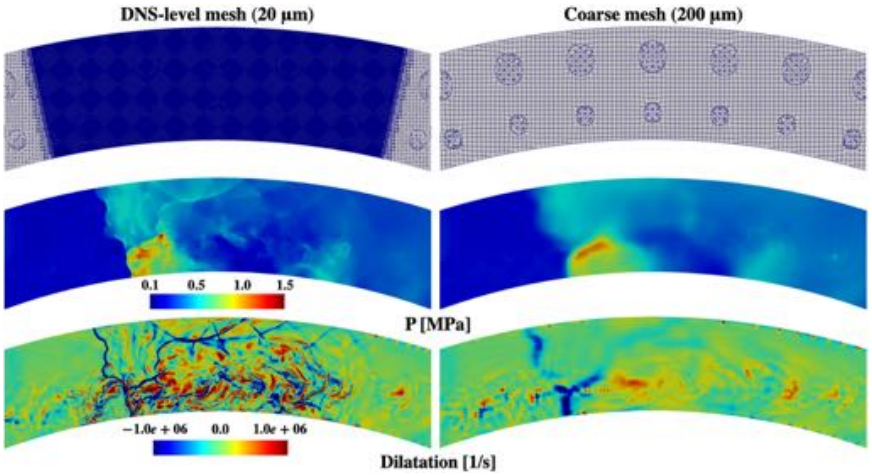

Figure 3.19: Comparison of the detonation wave structure within the RDRE channel with the (left) near-DNS level mesh and (right) coarse mesh in terms of (top row) mesh structure, (middle row) pressure profile, and (bottom row) dilatation rate.

Due to the GPU-accelerated scalability of the solver to large meshes and chemical mechanisms, additional studies were performed where a 25◦ sector of the RDRE geometry, spanning 5 pairs of injectors, was progressively resolved down to a 20 micron resolution from a 200-micron baseline mesh. This represents a near-DNS level resolution and provides an opportunity to study the detonation-turbulence interaction in a stratified mixture. The detonation wave solution in the DNS-level mesh is compared to a coarse mesh solution of 200 microns. Figure 3.19 shows a sector of the RDRE combustion chamber, along with pressure and dilatation profiles as the detonation wave passes through the near-DNS level region. Here, the wave triple points, reflected shock structures, and compressibility of the flow are evident.

The scramjet presented below is based on the axis-symmetric scramjet experimentally tested with the ACT-II facility [107]. The system utilizes ethylene-air with 16 discrete ethylene injectors. The chemical mechanism is a 41 species and 361 reactions that was extracted from FFCMy.9a (R. Xu and H. Wang, personal communication, June 2020). The operating condition is matched to a Mach 7 flight condition with the post inlet condition being Mach 4.5 with a total temperature of $2460K$ and a total pressure of 47.7 bar. The results for stoichiometric ethylene-air will be presented to demonstrate the capabilities of the solver.

The simulated flow path includes the isolator, combustor, and part of the exhaust nozzle. The mesh is dominated by hexahedral cells and the main flow path is a structured mesh with a small unstructured tetrahedral region near the injectors and to facilitate the change in mesh resolution. This ability to handle arbitrary order polynomials on the GPU is a strength of this framework. The mesh utilized 42 million cells with a resolution of 200 microns near the injectors and 400 microns in the cavity and flame stabilizing region with the resolution increasing to 800 and 1600 microns in the isolator and exit nozzle. The results for this case show ram mode operation within the scramjet with the combustor operating in a subsonic regime and the flow choking due to heat release at the end of the combustor. The temperature profile in Fig. 3.20 shows that the flame is anchored just prior to the step and shows the cavity is maintaining a reservoir of hot combusted gasses.

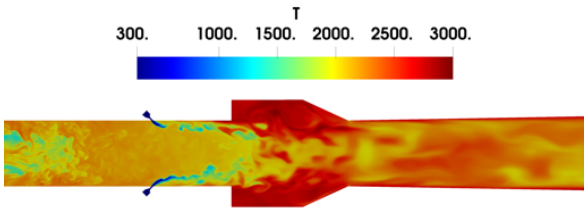

Figure 3.20: Instantaneous pressure contour along the cross-section for the scramjet operating in ram-mode, the pressure jump at the end of the cavity sue to thermal choking can be seen.

3.3.6 Performance

3.3.6.1 Weak Scaling

Weak scaling was conducted on Summit, with each node using 6 V100 GPUs and 2 IBM Power9 CPUs. Ideal strong scaling would should no increase in computational time with increasing number of MPI ranks, however in practice some increase does occur due to increased MPI communication time as well as some load imbalances. The solver UMdetFoam achieved less than a 20% increase in computational time when increasing from 6 GPUs (1 Node) to 3072 GPUs (512 Nodes). Past 3072 Nodes the increase in computational time begins to increase with almost a 50% increase in computational time for 6144 GPUs. Each GPU was partitioned $1,048,576$ cells with the largest case tested containing 6.4 billions cells. The heterogeneous exa-scale machines are tending towards very dense nodes with the computational effort being dominated, 99+%, in the GPUs. Given the computational power associated with each GPU being significantly greater than a comparable CPU processor there is no longer a need to scale to very large number of MPI ranks. This is demonstrated by 6144 GPUs being suitable for 6 Billion cells which is beyond the average problem size.

3.3.6.2 Strong Scaling

Strong scaling provides an estimate of the level of parallelism in combination of the point where the GPUs are no longer saturated. Strong scaling was performed by using 6 V100s GPUs and 2 IBM-Power9 CPUs per node and keeping the size of the problem constant. As the number of nodes increases there is a point where the computational time no longer shows significant decrease with increasing number of nodes. This can

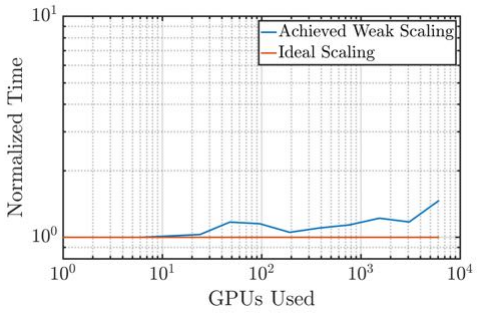

Figure 3.21: Weak Scaling

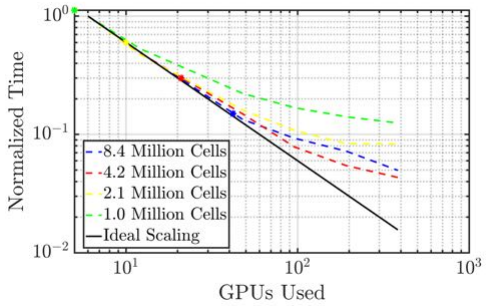

Figure 3.22: The time per iteration, normalized by the time when using 1 Node (6 GPUs) using varying number of GPUs. The trend shows a closer to ideal scaling with a larger problem size. The point representing 200,000 cells per GPU is marked on each curve with a '*'.

be understood by looking at the saturation point for a single GPUs, Fig. 3.23, it can be seen that around 200,000 cells per GPU the cell updates per second decreases rapidly. The domain is split into two regions a quasi-constant region and a linear region, the quasi-constant region is the point where adding more cells per GPU does not result in further speed-up as the GPUs are saturated. There is a linear region which is the point where the time per iteration is quasi-constant with decreasing number of cells per GPU, which occurs at $10,000$ cells per GPU for the test problem. The point at which this occurs depends upon the number of species being transported as with more species there is more work per cell. For the strong scaling analysis we can see that all cases begin to show significant deviation at 128 GPUs and this is to be expected as the largest case has less than $200,000$ cells per GPU at this point which

is outside of the quasi-constant region in the saturation plot. When comparing the the 1 node performance between the for four initial problem sizes we see the largest problem has iteration times that are 2.03, 4.06 and 8.66 times longer than than the 4.2, 2.1 and 1 million cell problems respectively; where the theoretical values are 2, 4 and 6 times longer. The saturation analysis would suggest that the minimum optimal problem size per GPU on summit is 1.2 million cells. This illustrates the challenge with strong scaling as the GPUs have limited memory, setting the maximum problem size per GPU to 2 million cells. The limited GPU memory combined with the higher number of cells required to saturate the GPUs creates this limitation on strong scaling. This problem can be alleviated by reducing the memory foot-print to allow for more cells per GPU or to decrease the saturation point.

For problems with large chemical mechanisms the computational cost to advance chemistry dominates over the cost to advance the fluid system. This allows for the weak and strong scaling to be closer to that of the chemical system and result in improved performance when operating with less than 200,000 cells per GPU. A major limiting factor on achieving a wider range of linear strong scaling is to be more restrictive on the allowable cells types to achieve more optimal memory access as well as algorithmic speed-ups.

3.3.7 Throughput Analysis

For CPU dominated codes the standard method for evaluating the efficacy of the code was through weak and strong scaling. These metrics don't directly provide how much of the computational resources are being used only how the utilization varies with number of MPI ranks and problem size. Therefore it is possible to have a code, through poor algorithmic design, that achieves near linear scaling but maintains low GPU utilization. GPUs have a fundamentally different design philosophy which necessitates looking at both the achieved utilization through throughput and saturation and that these metrics can be more important when analyzing performance than strong and weak scaling. This is demonstrated by the fact that some GPUs kernels have sub 1% FLOP utilization but may have excellent strong and weak scaling. Therefore it has been proposed both the achieved FLOPs and memory bandwidth for each kernel are used to analyze the performance of the code []. The throughput analysis shows that the majority of kernels are on the bandwidth limited line. This means that the limiting factor on performance is the rate at which data can be transferred to the processing units and not the rate at which computations can be completed. This

a known problem with traditional FVM calculations as the amount of operations performed on each variable is small for flux evaluations and interpolations. UMdetFoam overcomes this as the temperature calculations as well as chemistry calculations are significantly more computationally intensive.

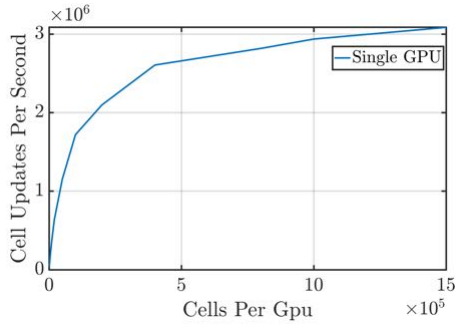

Figure 3.23: Representation of the average cell update per second achieved per GPU with varying problem size. The problem is split into a quasi-constant region and a linear region, as marked. The quasi-constant region represents the point where the GPU is saturated and adding more cells per GPU does not improve performance.

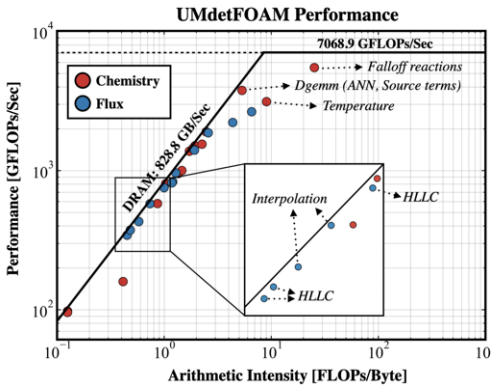

Figure 3.24: Roof Line Plot

The roofline plot displays the maximum achievable FLOPs for a kernel given the data required and computational intensity of said kernel. This is represented through arithmetic intensity (AI), the number of operations performed on a byte of data. This is compared to the rate at which data can be streamed to the GPU. To the

left of a device specific AI the kernel is limited by the rate it can transfer data from device RAM to the multi-processors. To the right of this point, where the black line is horizontal, the full computational resources can be utilized. For GPUs the goal is to be as close to maximum utilization as possible, this means formulating the krenels such that you achieve peak bandwidth and algorithmicly designing the kernels such that you achieve the highest AI possible and thus are decreasing the bandwidth limitations.

The nature of some types of calculations the AI is not sufficient to avoid being limited by the memory bandwidth. This can be seen as many of the kernels sit along the diagonal line representing the DRAM memory bandwidth. The bandwidth and the FLOPs achieved at this point are dependent upon the specific architecture.

3.4 Numerical Simulations of AAI-1 with Mass Flow Rate Effects

3.4.1 Introduction

Rotating detonation combustors (RDCs) utilize shock-based compression to increase the available work from the combustion device. Recently, RDCs have received renewed focus due to their applicability in a wide range of propulsion and energy conversion devices, including gas turbines [108, 43, 109, 110], rockets [111, 112], and scram and ramjets [111, 113]. Due to this broad applicability, ensuring robust operation of RDCs over a range of operating conditions is of immense interest for practical utilization. In many of the applications, the ability to control power output, quantified in the form of thrust or specific impulse, is an important requirement. In fixed geometry devices, fuel flow rate is the most direct control variable for modulating thrust. There exists a number of studies [114, 115, 116, 117, 109, 110, 118] which show that, for ideal and practical devices, increasing the mass flow rate of reactants increases thrust. However, due to the shock-driven nature of the detonation process, even when a direct relation between fuel flow rate and power output can be determined, the details of the energy conversion process might be quite complex. For instance, design of fuel injection schemes, non-ideal mixing, and interaction of products with fresh reactants can change the detonation characteristics [111, 117].

In an RDC, one or more detonation waves move azimuthally in an annular chamber, while fuel and oxidizer are injected as separate streams at the base of the chamber.

The injector design is critical in ensuring that the fuel-oxidizer streams are sufficiently mixed to ensure stable detonation. At the same time, the passing detonation wave may temporarily block the injector and may even cause backflow, which will affect the injection process as well as mixture preparation for future cycles. In many practical geometries, the detonation speed could be as low as 60-70% of the ideal Chapman–Jouguet (C-J) speed [43, 111, 117, 119, 120]. Recent simulations [121, 49] have shown that this speed reduction is due in part to stratification of the fuel-air mixture and large scale inhomogeneities in the mixing process caused by varying recovery of the injectors after the passage of a detonation wave. As a result, non-ideal mixing is an essential feature of the RDC, which will control the detonation process. While many different injection schemes have been studied [119, 122, 123, 111], a general heuristic that relates mixing efficiency to operability is still not available. While it may seem that better mixing will increase performance, ideal mixing will also increase shock strength. As a result, the injectors may remain blocked for longer times, which may cause poorer mixing, leading to unstable or galloping detonations [124].

Another critical yet incompletely understood process is the formation of multiple detonation waves within the combustor. While several factors can lead to multiple waves, it has been reliably observed that when the mass flow rate is increased while keeping other parameters such as equivalence ratio or geometric features the same, the number of waves observed within the domain increases [117, 125]. Prior analyses have shown that a minimal flow rate is needed to ensure that detonation is sustained [126], otherwise the reaction processes are driven by deflagrative combustion. However, beyond this minimal flow rate, the number of waves appears to be determined by so-called refill height (denoted by h). This parameter is essentially the maximum penetration distance of the fresh mixture in the axial direction before a detonation wave is encountered. Bykhovskii [111] concluded that single waves are observed for $h/\lambda \approx 12 \pm 5$, where λ is the cell size of detonation propagation through a homogeneous fuel-air mixture at the same global equivalence ratio. Several studies have since then explored the utility of this parameter [127, 128]. For instance, Frolov [127] shows that a 200 mm tall wave is sustained, which is at the higher limit of the condition proposed by Bykovskii [111]. However, this could be due to the fact the theoretical criterion does not take into account mixing effects. However, George et al. [128] conclude that h/λ alone cannot be used to determine wave transition, but they suggest a normalized perimeter, p/λ as a possible metric.

In order to further understand the physical interactions driving multiple wave formation, it is useful to consider the approach to wave splitting rather than the

operating conditions that produce different wave multiplicities. In this regard, there appears to be a useful trend: Given a starting condition with a particular number of waves, as the mass flow is increased while keeping other parameters a constant, the wave velocity monotonically increases until wave splitting is observed. This trend is seen, for instance, by Bykovksii et al. [111], where they demonstrate that for a single and multi-wave H_2/air system, the wave velocity increases with mass flow rate (Figure 12 in ref. [111]). This feature has been observed in other studies as well. For instance, the extensive set of experiments conducted by Cho et al. [129] show that for constant air flow slot width and equivalence ratio, the wave speed increases as mass flow rate is increased for a variety of operating conditions. This observation is also consistent with the transition from the deflagrative to detonative mode observed by Hayashi et al. [126], in that an increase in mass flow rates promotes a stronger detonation behavior. However, Zhou and Wang [130] show that as inlet stagnation pressure is increased, numerical results show constant detonation height. However, this simulation used premixed fuel-air as the feed stream and did not include the effect of non-ideal mixing.

Based on this discussion, the goal of this work is to determine the role of fuel-air mixing on the detonation characteristics when mass flow rate is increased. Such detailed calculations require high performance computing and massively parallel algorithms [49, 131, 52]. Prior numerical studies have typically used premixed fuel-air mixtures [116, 126, 132], focusing on the resulting hydrodynamic features of the RDC. Cocks and Holley [52] conducted a detailed numerical simulation, where the mixing process was resolved and multi-step chemical kinetics was used to capture the detonation process. More recently, Prakash et al. [121, 60] used high resolution simulations to demonstrate that in non-premixed fuel-air injection-based detonations, the shock and reaction structures are complex, with multiple compression and expansion waves present in the reaction zone. Moreover, the structure of the detonations was impacted by the level of fuel stratification. Additionally, Sato et al. [49, 133] conducted detailed simulations of practical RDCs. These simulations demonstrated that fuel-air mixing as well as the presence of large-scale recirculation zones near the base of the channel led to fuel oxidation prior to arrival of detonation wave. Overall, these non-idealities significantly reduced wave speed. Hence, understanding the changes to the mixing profiles due to variations changes in mass inflow would help in determining the conditions leading toward wave splitting.

The RDC configuration studied here is based on the experimental design of Chacon et al. [119], which uses an axial air injector and an angled fuel injector. This

system has been the subject of a number of studies [119, 46, 134, 38] including studies regarding the role of secondary combustion on detonation behavior [119]. Recently, Sato et al. [38] numerically simulated this configuration with an inflow air mass flow rate of 400 g/s, which exhibited decreased wave speed in comparison to the ideal C-J velocity. Analysis of the three-dimensional flow field suggested that two different deflagration regions are formed, one near the base of the channel due to a recirculation zone, and the other at the interface between fresh reactants and burnt products. Moreover, the detonation was weakened by this partial oxidation, leading to reduced wave velocity. In the current work, two other flow rates - 300 and 700 g/s - will be used to understand the role of mixing on detonation modification. In the experiments, the 700 g/s case exhibited two detonation waves, but this flow condition was reached in the experiments through an unconventional strategy (explained in Sec. 3.4.3.1). In the simulations, it will be shown that both cases show only a single wave, but the wave structure is modified completely. It will be demonstrated that shear-induced mixing strengthens the wave, leading to propagation that explains the trends observed in the prior studies described above.

3.4.2 Simulation configuration, experimental configuration, and computational details

The experimental setup used in the study is the same as was presented by Chacon et al. [119]. The RDC test facility is composed of a modular 154 mm outer diameter RDC, air and fuel supply systems, an enclosed exhaust system, and data acquisition and control systems. For this study hydrogen/air operation is considered.

The RDC used in the study is modular and can house different air and fuel handling configurations (Fig. 3.25). However, in this study we consider only the axial air inlet configuration that has been extensively studied in previous work [119, 46, 50]. This configuration is characterized by an axial air inlet where air flows axially over a smooth symmetric, one-sided contoured surface extending from the central body of the RDC. Fuel is injected from the rear of the contour through 120 discrete evenly spaced injection portholes of diameter 0.89 mm arranged around the circumference of the contour. The air throat gap is 1.52 mm, providing a throat-to-channel area ratio of $A_t/A_c = 0.2$. The RDC has an outer detonation channel diameter of 154 mm and inner channel diameter of 138.8 mm resulting in a channel gap width of 7.6 mm. The length of the channel, defined as the distance between the axial mid-plane of the air inlet throat and the exit plane, is 104 mm. Past the air inlet constriction,

the detonation channel has a constant cross section and directly discharges into an exhaust plenum connected to the exhaust system without any exit constriction.

The main challenge in simulating practical RDC configurations is the complex flow path, combined with the multiscale physics introduced by turbulence interacting with shock waves and chemical reactions. As a result, computational simulations over a large range of operational conditions or for long physical times are prohibitively expensive. Recently, Sato et al. [38] have demonstrated a robust computational solver for modeling such complex RDCs. In order to capture some behaviors of interest, two operating conditions were studied computationally, having mass flow rates of $\dot{m} = \{300, 700\}$ g/s (see Tab. 3.1). Companion experiments for this study were instead swept across a range of mass flow rates at nearly constant equivalence ratio for extended durations so as to capture a greater range of information than through single operational point tests. This approach has the benefit of being very time efficient compared to individual experimental runs. However it does pose the question of how significant the ramping effect is on the properties of the detonation wave we are trying to investigate. Here we consider the transient taken (approximately 3.5 seconds) to be of a sufficiently long timescale compared to the detonation cycle time (approximately 300 microseconds) such that it had minimal impact on detonation velocity and correspondingly fast processes/measurements. In the experiment discussed here, operation of the device was initiated at an air mass flow rate of approximately 200 g/s of air at an equivalence ratio of 0.6. Following a half second stabilization, the fuel and air flow rates were transitioned over a 3.5 second transient to a final operational condition of approximately 1,000 g/s of air with an equivalence ratio of approximately 0.8. Figure 3.28 shows the mass flow rate and equivalence ratio trajectory taken as a function of time.

This particular $(\dot{m}, \phi)$ trajectory was designed to minimize the variation of equivalence ratio ϕ for the majority of the mass flow rate sweep. In particular, between a mass flow rates of 400 and 1,000 g/s the equivalence ratio remains approximately constant. The relatively small variation in equivalence ratio makes this case a good approach to investigate how the wave speed varies with mass flow rate and the wave splitting process.

The two experimental runs (cases 1 and 3 in Tab. 3.1) operate at different equivalence ratios. In the experiment of case 1, a single wave is observed. In order to ensure that the effect of the equivalence ratio is taken into account, a third simulation (case 2) at an equivalence ratio of 0.75, which is equal to that of the higher mass flow rate case, is also conducted.

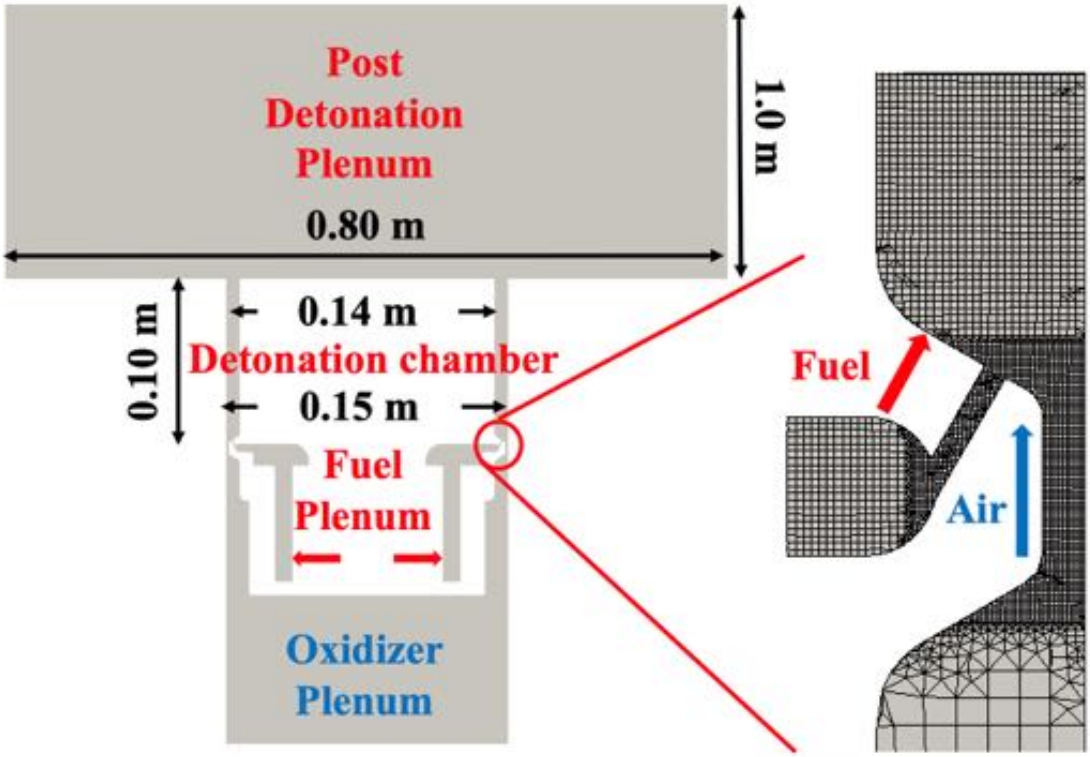

Figure 3.25: Schematic of the simulated the geometry with the detailed grids structure around the discrete fuel injector and the air inlet.

The simulations are carried out at constant mass flow rates. As a result, there are operational differences from the experimental runs. In this study, governing equations for fluid flow including viscous terms, species transport with diffusion terms, and the energy equation are solved. In conservative form, these equations are:

$$\frac{\partial \rho}{\partial t} + \frac{\partial \rho u_i}{\partial x_i} = 0, \tag{3.21}$$

$$\frac{\partial \rho u_i}{\partial t} + \frac{\partial \rho u_i u_j}{\partial x_j} = -\frac{\partial p}{\partial x_i} + \frac{\partial \tau_{ij}}{\partial x_j}, \tag{3.22}$$

$$\frac{\partial \rho E}{\partial t} + \frac{\partial \rho u_j H}{\partial x_j} = \frac{\partial}{\partial x_j} \alpha \frac{\partial T}{\partial x_j} + \frac{\partial \tau_{ij} u_i}{\partial x_j}, \tag{3.23}$$

	$\dot{m}_{\text{air}}$ [g/s]	ϕ	$P^{\text{air}}_{\text{plenum}}$ (cold flow) [kPa]	$P^{\text{fuel}}_{\text{plenum}}$ (cold flow) [kPa]	Fuel injection holes [m]	Air inlet slot [m]	$\bar{P}^{2.54\text{cm}}_{\text{Expt.}}$ [kPa]	$\bar{P}^{2.54\text{cm}}_{\text{Sim.}}$ [kPa]	$\frac{D_{\text{Expt.}}}{D_{\text{CJ}}}$	$\frac{D_{\text{Sim.}}}{D_{\text{CJ}}}$
Case1	300.88	1.02	187	246	8.9×10^{-4}	1.6×10^{-3}	137	130	0.8	0.9
Case2	300.88	0.75	187	200	8.9×10^{-4}	1.6×10^{-3}	–	124	–	0.87
Case3	700.36	0.75	388	434	8.9×10^{-4}	1.6×10^{-3}	–	226	0.7	0.92

Table 3.1: Details of the test cases as well as the key injector/inlet dimensions.

$$\frac{\partial \rho Y_i}{\partial t} + \frac{\partial \rho u_j Y_i}{\partial x_j} = \frac{\partial}{\partial x_j} \rho D \frac{\partial Y_i}{\partial x_j} + \dot{\omega} M_i, \tag{3.24}$$

where ρ is the mass density, u, v, w are x, y, and z velocity components, respectively, p is the pressure, E is the total energy, and H is the total enthalpy. To account for chemical reactions, mass fraction transport equations need to be solved. In the formulation here, detailed chemical kinetics are used, which involves solving N additional equations for a N-species chemistry mechanism. For each species $i = 1, \ldots, N$, where N is the number of species, Y_i is the mass fraction, $\dot{\omega}_i$ is the molar production rate, and M_i is the molecular mass. Note that each species has its own transport equation.

The above equations are solved using a modified unstructured grid solver termed UMdetFOAM, which was built based on the open source OpenFOAM framework [135]. The chemical source terms, transport, and thermochemical properties are obtained by coupling UMdetFOAM to the CANTERA software [136]. In this study, the hydrogen/air mechanism with 9 species with 19 steps is used [137]. In order to improve numerical accuracy, MUSCL-based HLLC scheme for spatial discretization is used for the convective terms. The time advancement is fully explicit, which vastly simplifies parallelization, and uses a second-order Runge-Kutta scheme [138]. The diffusion terms are discretized using the Kurganov, Noelle and Petrova (KNP) method [139]. The solver has been extensively verified in a series of studies [140, 49, 133, 134, 38]. Figure 3.25 shows the mesh used in this study. The lower part of the domain where fuel and air injectors are located is highly resolved in order to capture the shear layer. The minimum mesh size is 10^{-4} m, while the maximum mesh spacing is 2×10^{-4} m in the detonation chamber, which results in 45×10^6 control volumes. The res-

olution study in RDCs systems reveals that grid sizes that are twice or four times coarser than the current mesh produce at most 5% error in terms of the averaged axial pressure distribution, thrust, and mass flow rate at the injection exit for similar hydrogen-air systems [141]. Furthermore, the prior studies show that the distributed reaction region across the wave due to deflagrative combustion alleviates the need for resolving the very thin induction region that is typical of ideal detonation waves. As a result, a grid spacing of 2×10^{-4} m results in at least 10 to 20 cells across the induction length [133, 38, 141]. In order to smoothly remove the shocks that exit the combustion chamber, a sponge region is used, where a coarse region termed the afterburner is used to diffuse out the pressure waves. A no-slip, adiabatic wall and constant mass flow boundary conditions are applied in this study.

The simulations are carried out as follows. First, the jets are developed for 0.4 ms but no chemical reactions are computed. After the jet development process, a one-dimensional detonation profile is patched with a height of 1 cm in the detonation chamber to initiate a detonation wave. To ensure that the flow-field reaches steady state, the computations are run for at least 20 detonation cycles. The data for analysis, which will be discussed from the next section, are collected for 10 cycles after reaching a steady state, which results in at least 30 cycles for each case. All simulations are run on 4000 cores using MPI-based domain decomposition.

3.4.3 Results and discussion

3.4.3.1 Observations from experiments

By monitoring the flow rates through the air and fuel supply lines and by using the high-speed pressure measurements, we are able to correlate the mass flow rate through the RDC with the detonation wave speed and observe the wave splitting process. The relationship between the mass flow rate and wave speed is shown in Fig. 3.26. Between 200 and 400 g/s, both the mass flow rate and equivalence ratio vary significantly (see Fig. 3.27), while from 400 g/s to the end of the transient, the equivalence ratio remains nearly constant at 0.75. Initially the RDC operates in a single detonation wave mode, and the wave speed increases as both $\dot{m}$ and ϕ are increased. The wave speed continues to increase even once the constant equivalence ratio portion is reached, and then the wave splits at about 500 g/s, and the wave speed suddenly drops (from about 1.6 km/s to just over 1.3 km/s). By increasing the mass flow rate further the wave speed increases back up until the system transitions to

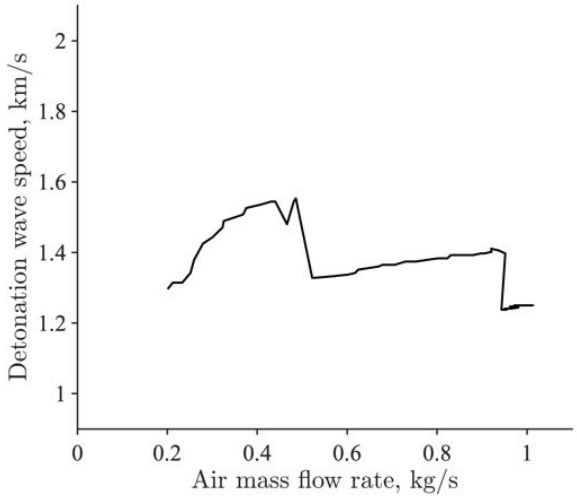

Figure 3.26: Detonation wave speed as a function of mass flow rate during the transient operation. Sudden change in speed indicates transition from 1 to 2 and from 2 to 3 waves.

a three wave operation mode at about 900 g/s. In this mode the wave speed reduces further to about 1.25 km/s. Although the mass flow rate slowly increases in the latter portion of the transient (from 3 to 5 seconds), the wave speed remains nearly constant at about 1.25 km/s for the remainder of the transient. The evolution of the wave system through the transient, including the presence of secondary waves, can also be seen from the waterfall spectrum shown in Fig. 3.28 computed from the high-speed pressure measurement taken at the combustor outer wall at an axial location of $z/H = 0.3$. The behavior observed in this transient run is similar to observations made by Bykovskii et al. [111], where after every wave splitting event, the speed of the wave decreased.

3.4.3.2 Instantaneous flow structure

Figures 3.29 – 3.31 show the instantaneous pressure and temperature profiles for the three cases. In all simulations, a single detonation wave is found to propagate azimuthally in a clockwise direction without any change in the direction of motion. From the side view, it can be seen that the detonation wave is taller for the higher mass flow rate case, as expected due to the increased fill height. Moreover, the shock

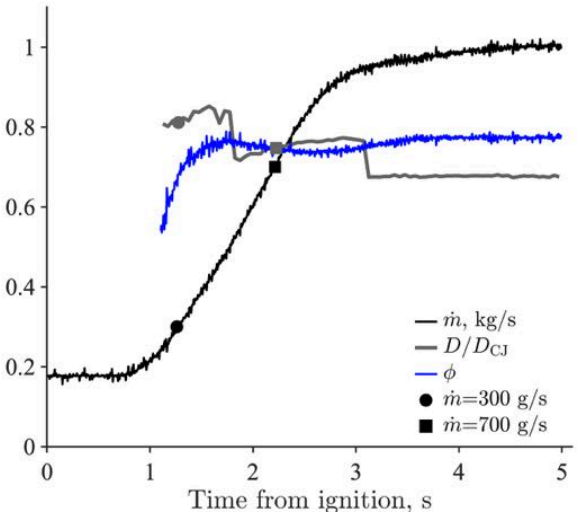

Figure 3.27: Time-history of air mass flow rate, equivalence ratio and wave speed across the duration of the full transient operation.

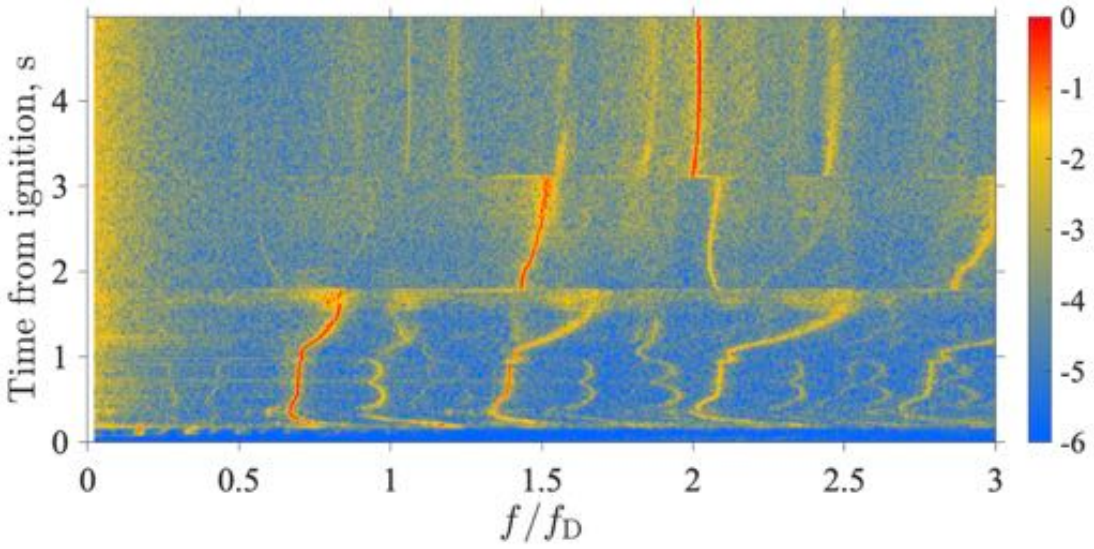

Figure 3.28: Waterfall spectrum from high-speed pressure measurement at $z/H = 0.3$ during the transient operation shown in Fig. 3.27.

appears stronger but is also thicker in the shock-normal direction. For the $\dot{m} = 300$ g/s cases (1 & 2 in Tab. 3.1), the variation in equivalence ratio does not affect the detonation height significantly, suggesting that the detonation height is decided by the fill height, with the wave velocity sufficiently low to allow this fill height to be reached. The top view shows that, at least at this instant, the shock wave is stronger near the outer wall compared to the inner wall. In the $\dot{m} = 300$ g/s cases, the temperature profile is roughly homogeneous across the radial direction for $\phi = 1$, while there is strong variation present for $\phi = 0.75$. Similar radial variation can be also seen in the $\dot{m} = 700$ g/s case. Near the outer wall (shown in Fig. 3.31), striations in temperature are seen behind the shock wave, which result from the discrete air injectors.

To further understand the wave structure, an unwrapped slice of the three-dimensional flow is shown in Figs. 3.32 – 3.33 for cases 1 & 3 (case 2 shows similar structure to case 1 and is not discussed here). These plots are extracted along the middle of the channel, and show significant differences. Before discussing the variations, the flow structure is first characterized for the low mass flow case. The flow field prior to the detonation can be divided into three approximate zones: post-detonation products (from the previous cycle), a buffer region (BR) composed of nominally pure fuel or oxidizer depending on the injection response of the two reactant streams, and the fresh fill region. At the boundary between the products and the buffer region, it is possible to stabilize a contact burn (CB1), a localized flame supported by hot products and fresh reactant in the buffer region. Similarly it is possible to stabilize a contact burn between the buffer region and the fresh fill region (CB2). Lastly it is possible to see in temperature contours that there are significant regions in the fill region that are at elevated temperatures suggesting reaction and a phenomena termed parasitic combustion [46]. Currently we draw distinctions between these zones and features because the supporting mechanisms are not entirely known, may be different, and to some degree independent of one another, as evidenced by CB2 being more intermittent in Fig. 3.32 while being more continuous in Fig. 3.33. In prior two-dimensional numerical studies, contact burning has been identified as a possible source of inefficiency [142, 143] as it is an inherently deflagrative process. However, in most simulations, the detonation wave proceeds at nearly the ideal velocity, indicating that any deflagration in this region does not cause loss of detonation efficiency. However, in this three-dimensional study, deflagrative processes are widespread as evidenced by the increased temperature throughout the fill region. These regions of parasitic combustion are likely formed primarily due to the nature of the injector used, and the extended recirculation zone generated by the interaction of the fuel and

oxidizer jets. Meanwhile, the buffer region is created by the different recovery time scales of the air and fuel injectors. Because the fuel injector is nominally stiffer in this configuration, it recovers faster than the oxidizer injector. The detailed discussion for the injector dynamics can be found in Sec. 3.4.3.3. This unsteady injection process creates regions that contain fuel-air mixtures that are too rich to burn. As a result, the buffer region is marked by high equivalence ratios and low temperatures.

Based on our definitions above, the two mass flow rate cases show differences in the structure of the three pre-detonation zones. In particular, the $\dot{m} = 300$ g/s case shows a parabolic shape, with the low temperature region showing lower penetration immediately ahead of the detonation front compared to distances farther away. This indicates that contact burning has led to significant deflagrative heat release, which increases local temperature, but reduces the fuel available for detonative combustion. Due to the lower fill velocity, CB1 and CB2 are located at distances closer to the base of the channel compared to the $\dot{m} = 700$ g/s case. In the $\dot{m} = 700$ g/s case, BR is nearly a straight line, intersecting the detonation front at its full height. This structure is similar to the two-dimensional structure of RDCs [116, 142]. However, the parasitic combustion region shows increased penetration and higher temperature, indicating higher thermal losses. As a result, the detonation waves are, in some sense, the extreme cases studied by Hayashi et al. [126], with the lower mass flow rate case showing higher deflagrative combustion as compared to the higher mass flow rate case.

Further, consistent with prior studies [111], there is an increase in detonation velocity from 1715 m/s (for $\dot{m} = 300$ g/s) to 1817 m/s (for $\dot{m} = 700$ g/s) for $\phi = 0.75$ as mass flow rate is increased. For the richer condition at $\phi = 1.0$ (case 1), the wave speed is computed as 1786 m/s, which is higher than $\phi = 0.75$ case. The ratios between the measured wave velocity and the C-J speed are shown in Table 3.1. The simulations overpredict the wave speed by nearly 15% compared to the experimental value. Note that such discrepancies between experiments and simulations have been noted elsewhere as well [144, 52]. One of the possible reasons for this difference is that the experiment run time is over a few seconds, but the simulations are computed for around 10 ms only due to the severe computational cost. Due to this run time difference, the system may not have reached a thermal steady state in the simulations. However, this aspect needs to be explored further.

From the simulations, it is seen that this increase in speed and the averaged pressure in the chamber are also associated with a reduction of parasitic combustion (a known loss mechanism), but significant regions still persist. As a result, for every

case, the detonation speed is much lower than ideal C-J speed. However, the wave speed is faster for the $\dot{m} = 700$ g/s case despite the increase in parasitic combustion at the mid-channel as shown in Fig. 3.33. This is because the detonation wave propagates near the outer wall, where the mixing is less affected by parasitic combustion [38]. This detail will be discussed in Sec. 3.4.3.3. From these cases, it is seen that the progress towards wave-splitting is accompanied by an increase in detonation efficiency, possibly driven by a reduction of parasitic combustion that is associated with detonative combustion. In addition, the shock front is more well-defined for the $\dot{m} = 700$ g/s case (Fig. 3.33) as opposed to the $\dot{m} = 300$ g/s case (Fig. 3.32), where the high-pressure region is observed only at the top of the detonation wave and a small region of unburnt gases is present ahead of the detonation wave. In other words, at low mass flow rates, the pressure profile can be highly varying due to the competition between parasitic combustion and fuel-air mixing. The shock structure in the $\dot{m} = 700$ g/s case is similar to the thickened front found in linear model experiments [145] and simulations [121].

3.4.3.3 Statistical analysis

The above findings can be understood from a mixing standpoint by considering time-averaged statistics. Figure 3.34 shows azimuthally averaged mixture fraction (equivalent to equivalence ratio) and temperature across a radial section of the channel. Overall, average mixture fraction shows similar profiles, indicating that fuel distribution within the chamber is not significantly different. In particular, the fuel jet is deflected upwards (axial direction) by the oxidizer jet, with local fuel-to-air ratios exceeding stoichiometric condition. At the same air mass flow rate, the higher equivalence ratio case shows higher jet penetration, driven by the higher flow rates through the fuel ports. Further downstream, the equivalence ratio decreases with close to stoichiometric values found past 40 mm. However, the temperature profile is highly altered by the change in the equivalence ratio and mass flow rate. In the $\dot{m} = 300$ g/s cases, there exists a small region of high temperature in between the inner wall and the fuel inlet which becomes wider for $\phi = 0.75$. This region is responsible for the recirculation of product gases that results in the parasitic deflagration region bounded between CB2 and the air/fuel injectors (Fig. 3.32). In the $\dot{m} = 700$ g/s case, there is a much larger region of high temperature near the inner wall, which promotes the CB2 deflagration process. Further, the $\dot{m} = 300$ g/s cases show higher temperatures past the detonation height, which indicates continued deflagration and heat release,

while the $\dot{m} = 700$ g/s rate indicates lower temperatures at downstream locations.

Figures 3.35 and 3.36 show time-averaged velocity at the exit of the injectors for three cases. For both fuel and air inflows, the peak velocities are roughly the same for the two cases. The response of the fuel injector is not significantly altered by the mass flow rates. Given that the fuel holes are smaller, the injector is generally stiffer than the air injectors. As a result, the response to the detonation wave including the time taken to recover to the full injection velocity is nearly identical for three cases. However, the air injector shows considerable differences in the response to the detonation wave. In the $\dot{m} = 300$ g/s cases, the injectors remain blocked for a longer duration, with a shallow recovery to the fully unblocked state. When the mass flow rate is increased, the blockage time is considerably reduced, with the injector recovering quicker to the full velocity mode. It is seen that the $\dot{m} = 700$ g/s case causes a second weaker blockage following the first suppression, which implies a three dimensional pressure reflection in the chamber. Moreover, the lowest velocity observed is considerably higher for the $\dot{m} = 700$ g/s case. Considering that the detonation wave is much stronger, this lower blockage indicates two aspects: a) the higher plenum pressure makes the injector stiffer and reduces the impact of higher detonation pressure and b) stronger detonations lead to a confined region of pressure increase, which allows the injectors to recover faster.

The net effect of differences in the oxidizer and fuel injector response is to alter the axial distribution of oxidizer and fuel depending on operating conditions (i.e., mass flow rate). In the $\dot{m} = 300$ g/s case, there is a time difference between the recovery of the fuel and oxidizer injectors. As a result, even when operating at a globally stoichiometric condition, the fueling rate can be vastly different leading to regions of very high and low equivalence ratios. On the other hand, the faster recovery in the $\dot{m} = 700$ g/s case causes the air injection to be approximately equivalent to the fuel injection process, leading to more uniform fuel-air mixtures. Moreover, the faster recovery increases the oxidizer velocity and the shear-induced mixing of the fuel and air streams. This leads to fine-scale mixing and better mixture preparation for the passing detonation wave.

A final analysis regarding heat release location is presented next. Here, the time at which maximum heat release occurs at a particular point in the cross-sectional plane is obtained. For this purpose, consider the schematic shown in Fig. 3.37. Here, the location of detonation front is marked by time $\bar{t} = 0$. For every location on the cross-section, the time at which maximum heat release occurs as a delay with respect to when the detonation wave reaches that point is measured. Negative values

indicate that maximum heat release occurs before the wave arrives, while positive values indicate post-detonation maximum heat release. The time is normalized by the detonation cycle time. Figure 3.38 shows this maximum heat release time for the three cases. It is seen that in the $\dot{m} = 300$ g/s cases, the inner wall region of the lower part of the domain shows peak heat release before the arrival of the wave, while this pre-wave heat release region is pushed farther downstream in the $\dot{m} = 700$ g/s case. This region signifies deflagrative burning, due to recirculation of product gases and mixing with fresh gases. The faster recovery in the $\dot{m} = 700$ g/s case pushes this mixing-induced deflagration to downstream locations.

The time scale plot only shows the location of the peak value but does not indicate the amount of heat release in pre- and post-detonation regions. As such, it is useful to examine the distribution of the amount of heat release. The normalized and time-averaged heat release plot is also shown in Fig. 3.38. In the $\dot{m} = 300$ g/s cases, heat release is spread across the channel width, while in the $\dot{m} = 700$ g/s case, the presence of the strong detonation wave traversing along the outer wall skews the energy release distribution. It is also found the variation of the equivalence ratio (cases 1 & 2) did not affect the time-averaged heat release. Overall, most of the heat release occurs in the lower half of the domain.

3.4.4 Conclusions

In this study, an experimentally-studied realistic RDC configuration [119] was simulated using detailed computational tools. Two different flow rates were considered. For $\dot{m} = 300$ g/s, the equivalence ratio is varied between 0.75 and 1.0 to see its effect on the mixing and detonation structure. While all simulated cases produced a single wave, the $\dot{m} = 700$ g/s case was closer to the regime where wave splitting has been observed experimentally. Analyses of flow fields, heat release rates, and injector recovery were conducted.

One of the motivations for this work is the observed increase in wave speed with increase in mass flow rate. The experiments corroborated prior observations, indicating that the RDC exhibits similar flow physics. The numerical simulations showed that as mass flow rate is increased, the injector recovery is faster due to the higher plenum pressure. This results in more steady fuel and air injection and better mixing characteristics. The end effect is an increase in the strength of the detonation wave associated with a reduction in parasitic combustion in the fill region. The wave velocity thus increases, even as the detonation height also increases due to a larger

refill height. It is also observed that as wave height increases, autoignition tendency increases in the freshly injected reactants even with minimal mixing of product gases. It is our hypothesis that when such deflagrative burning becomes more dominant, additional weak waves, initially in the form of acoustic waves, could be generated that interact with the main wave to cause splitting of the detonation front. At this point, this process remains merely a hypothesis. Future work will explore the incipient wave splitting process.

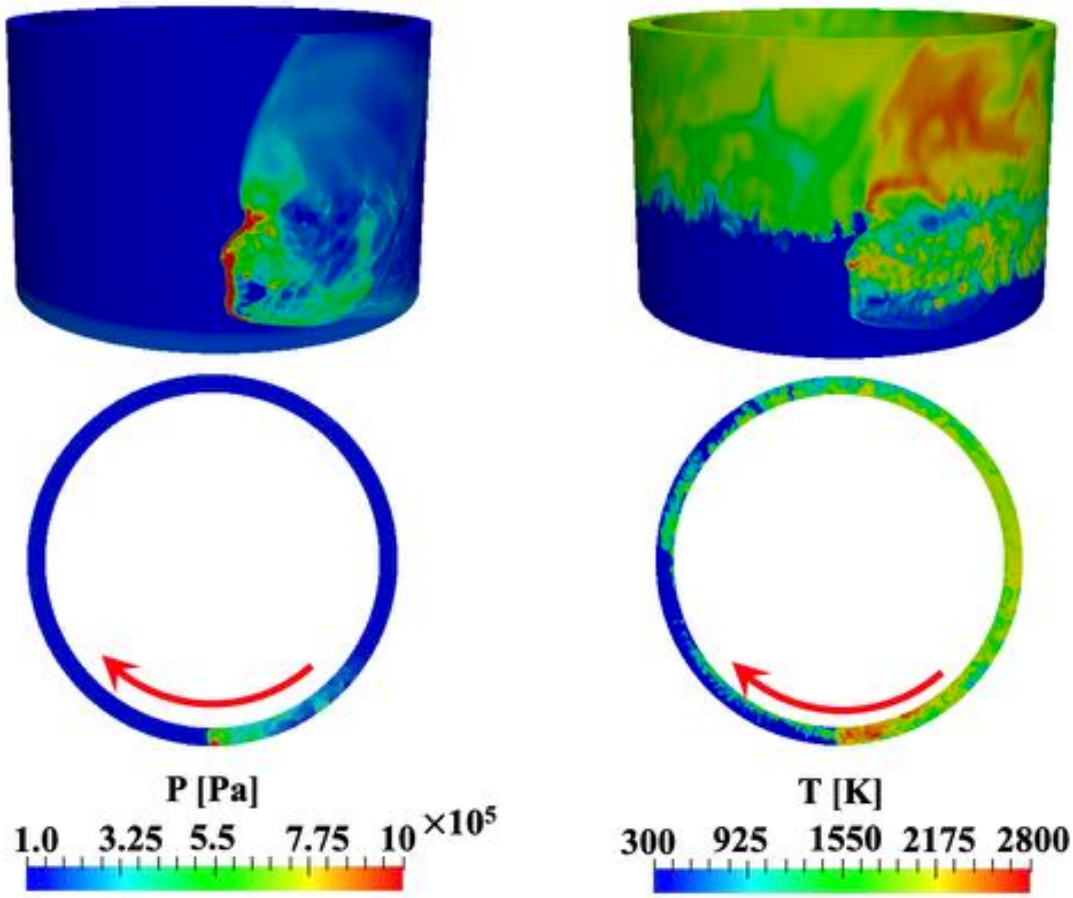

Figure 3.29: Three-dimensional (3D) view and the top view on the axial cutting plane of pressure and temperature for $\dot{m} = 300$ g/s at $\phi = 1.0$.

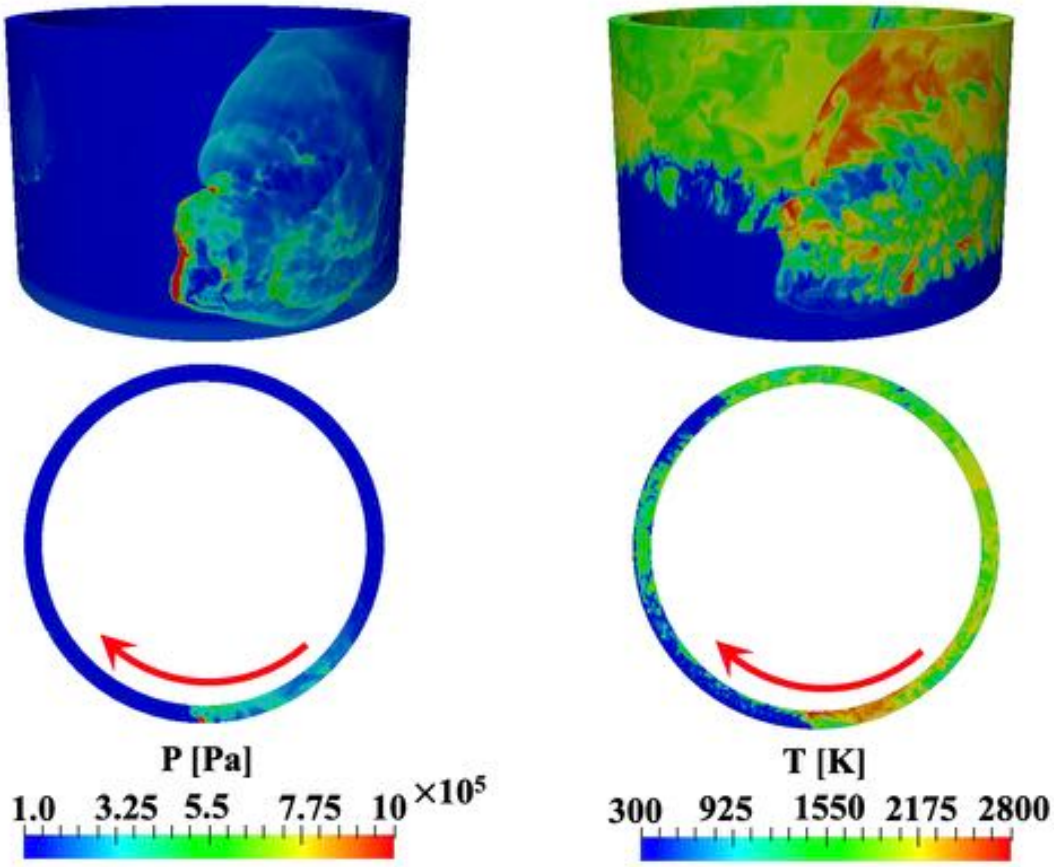

Figure 3.30: 3D view and the top view on the axial cutting plane of pressure and temperature for $\dot{m} = 300$ g/s at $\phi = 0.75$.

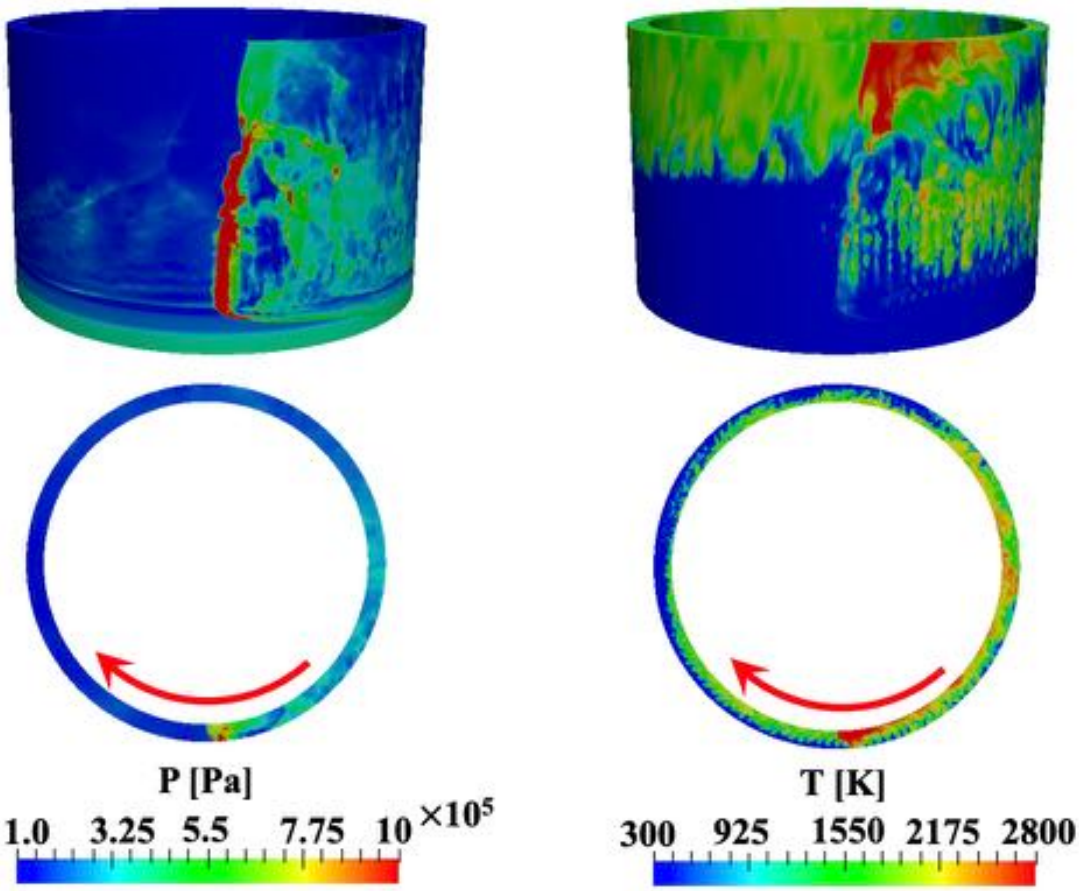

Figure 3.31: 3D view and the top view on the axial cutting plane of pressure and temperature for $\dot{m} = 700$ g/s at $\phi = 0.75$.

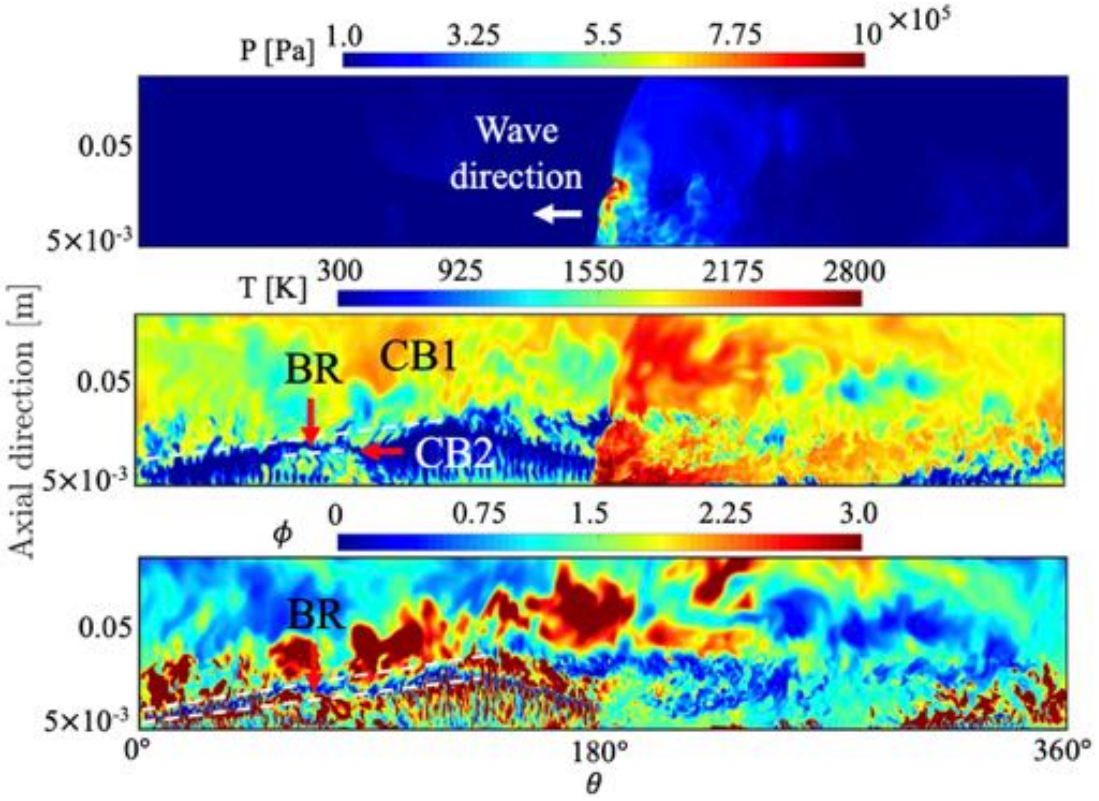

Figure 3.32: Pressure, temperature, and the equivalence ratio on the unwrapped plane at the mid-channel for $\dot{m} = 300$ g/s at $\phi = 1.0$.

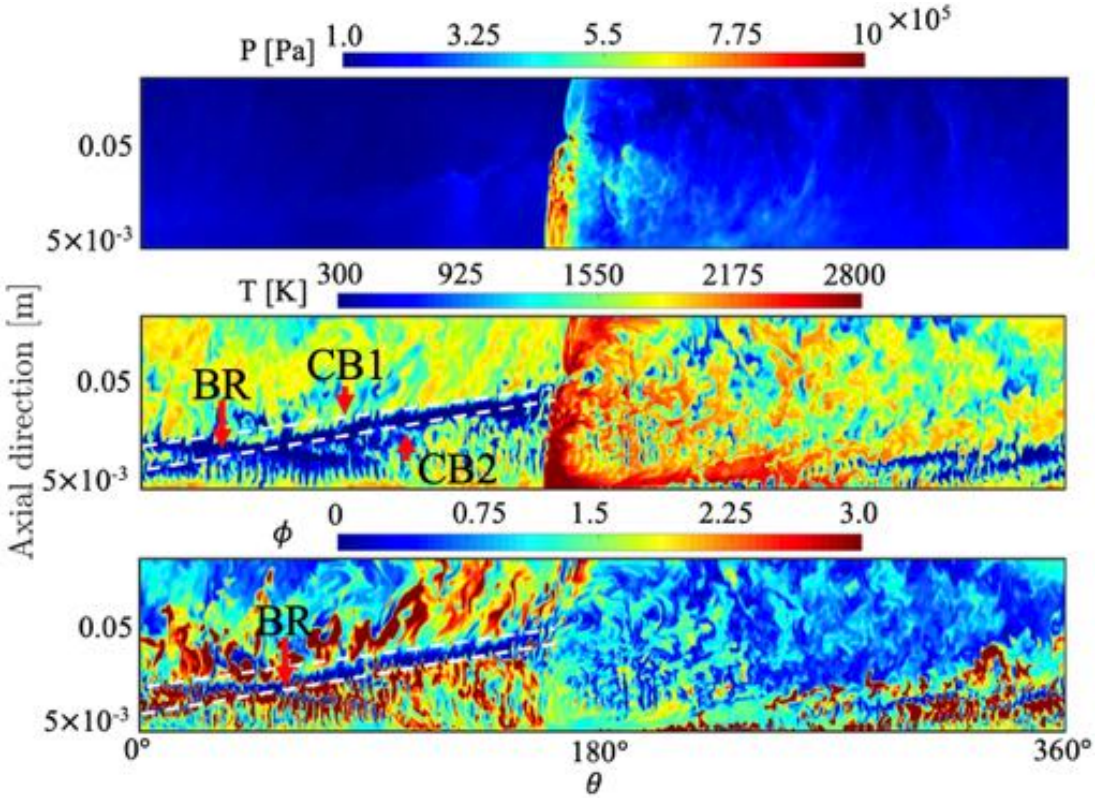

Figure 3.33: Pressure, temperature, and the equivalence ratio on the unwrapped plane at the mid-channel for $\dot{m} = 700$ g/s at $\phi = 0.75$.

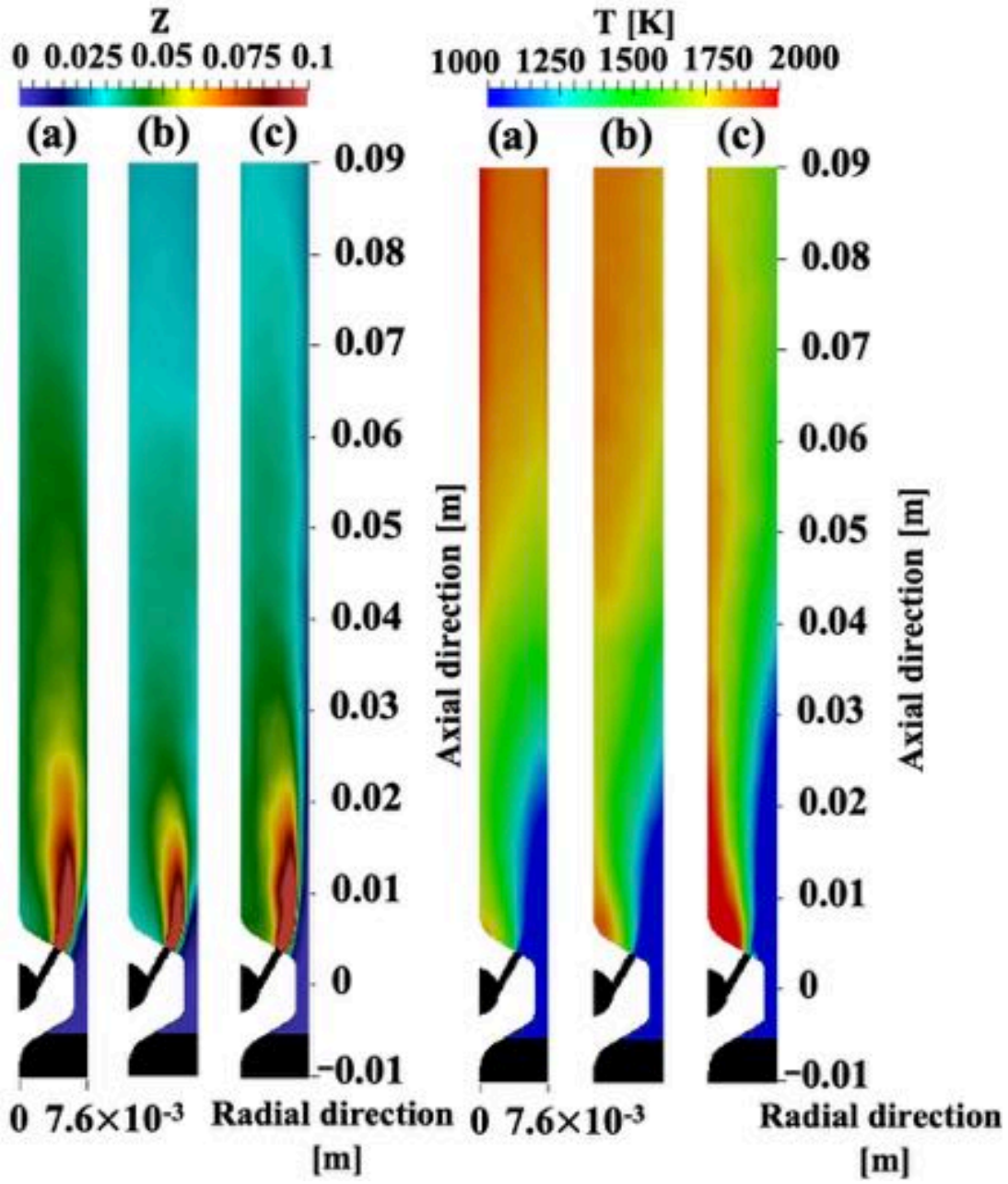

Figure 3.34: Azimuthal averaged mixture fraction and temperature for (a) $\dot{m} = 300$ g/s at $\phi = 1.0$, (b) $\dot{m} = 300$ g/s at $\phi = 0.75$, and (c) $\dot{m} = 700$ g/s at $\phi = 0.75$.

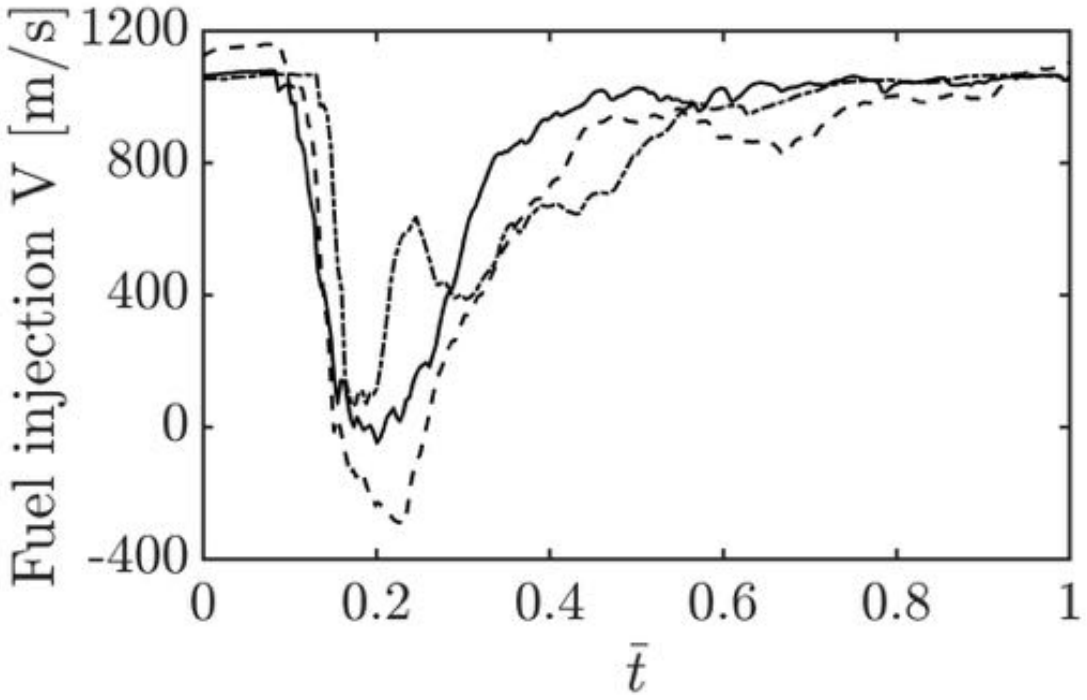

Figure 3.35: Axial fuel injection velocity history for the low and high mass flow rate cases obtained by averaging over multiple detonation cycles. (Solid line) $\dot{m} = 300$ g/s at $\phi = 1.0$, (dashed line) $\dot{m} = 300$ g/s at $\phi = 0.75$, and (dashed-dot line) $\dot{m} = 700$ g/s at $\phi = 0.75$.

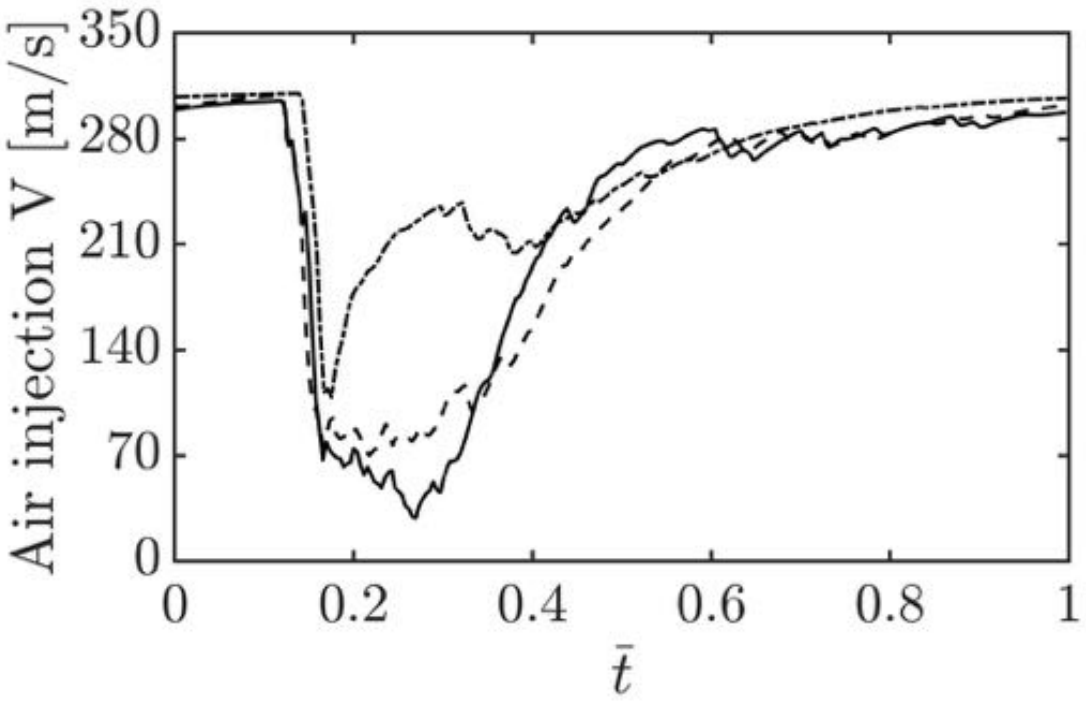

Figure 3.36: Axial air injection velocity history for the low and high mass flow rate cases obtained by averaging over multiple detonation cycles. (Solid line) $\dot{m} = 300$ g/s at $\phi = 1.0$, (dashed line) $\dot{m} = 300$ g/s at $\phi = 0.75$, and (dashed-dot line) $\dot{m} = 700$ g/s at $\phi = 0.75$.

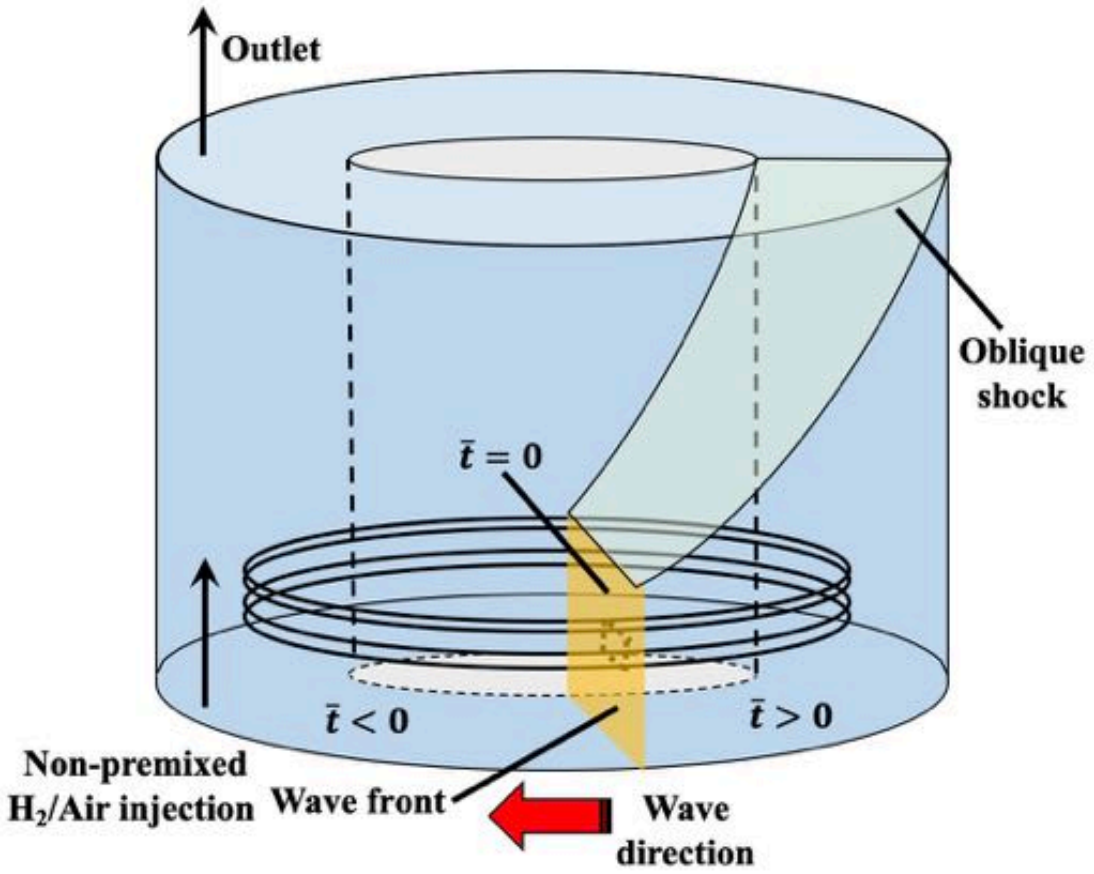

Figure 3.37: Schematic showing the averaging procedure used to obtain the time-delay plots.

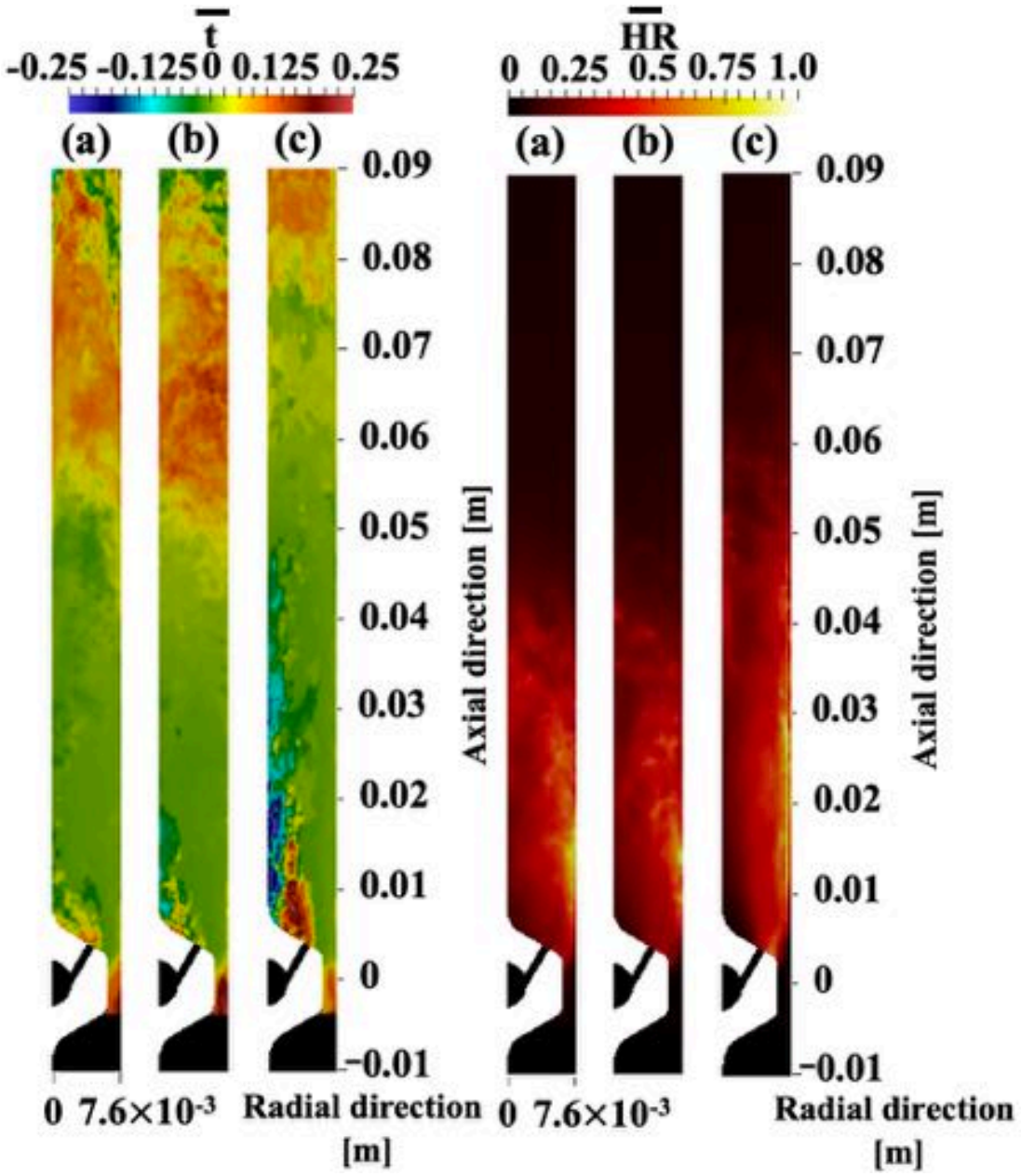

Figure 3.38: (Left) Time delay plot showing maximum heat release at a given cross section point with respect to the detonation wave, and (right) distribution of time-averaged heat release for (a) $\dot{m} = 300$ g/s at $\phi = 1.0$, (b) $\dot{m} = 300$ g/s at $\phi = 0.75$, and (c) $\dot{m} = 700$ g/s at $\phi = 0.75$. The time delay has been normalized by the cycle time of the detonation wave.

Bibliography

[1] Chacon, F., Duvall, J., and Gamba, M., "Evaluation of Pressure Rise and Oscillation in a Rotating Detonation Engine," *2018 AIAA Aerospace Sciences Meeting*, American Institute of Aeronautics and Astronautics, jan 2018.

[2] Chacon, F. and Gamba, M., "Detonation Wave Dynamics in a Rotating Detonation Engine," *AIAA Scitech 2019 Forum*, American Institute of Aeronautics and Astronautics, jan 2019.

[3] Feleo, A., Chacon, F., and Gamba, M., "Effects of Heat Release Distribution on Detonation Properties in a H_2/Air Rotating Detonation Combustor from OH* Chemiluminesence," *AIAA Propulsion and Energy 2019 Forum*, 2019.

[4] Feleo, A., France, J., White, L. W., and Gamba, M., "Evaluation of OH Emission for Determining Operation of a Rotating Detonation Engine," *AIAA Scitech 2019 Forum*, American Institute of Aeronautics and Astronautics, jan 2019.

[5] Chacon, F., Feleo, A., and Gamba, M., "Impact of Inlet Area Ratio on the Operation of an Axial Air Inlet Configuration Rotating Detonation Combustor," *AIAA Propulsion and Energy 2019 Forum*, 2019.

[6] Duvall, J., Chacon, F., Harvey, C., and Gamba, M., "Study of the Effects of Various Injection Geometries on the Operation of a Rotating Detonation Engine," *2018 AIAA Aerospace Sciences Meeting*, Jan. 2018.

[7] Feleo, A., Chacon, F., and Gamba, M., "Uncertainties in Thrust and EAP Measurements of a Rotating Detonation Combustor with Axial Air Inlet," *AIAA Propulsion and Energy 2020 Forum*, American Institute of Aeronautics and Astronautics, Aug. 2020.

[8] Garrott, Kristin, B., "Improved aerothermodynamic measurements of the T63-A-700 gas turbine engine," 2005.

[9] Shepard, J., Feleo, A., and Gamba, M., "Effects on Inlet Area Ratio on Operability of Axial Air Inlet Rotating Detonation Combustor," *AIAA Propulsion and Energy 2021 Forum*, 2021.

[10] Deng, L., Ma, H., Xu, C., Zhou, C., and Liu, X., "Investigation on the propagation process of rotating detonation wave," *Acta Astronautica*, Vol. 139, 2017, pp. 278–287.

[11] Anderson, J. D., *Modern compressible flow: with historical perspective*, McGraw-Hill New York, 1990.

[12] Bennewitz, J. W., Bigler, B. R., Hargus, W. A., Danczyk, S. A., and Smith, R. D., "Characterization of Detonation Wave Propagation in a Rotating Detonation Rocket Engine using Direct High-Speed Imaging," *2018 Joint Propulsion Conference*, American Institute of Aeronautics and Astronautics, jul 2018.

[13] Stamps, D. W. and Tieszen, S. R., "The influence of initial pressure and temperature on hydrogen-air-diluent detonations," *Combustion and Flame*, Vol. 83, No. 3-4, Feb. 1991, pp. 353–364.

[14] Guirao, C., Knystautas, R., and Lee, J., "A summary of hydrogen-air detonation experiments," Tech. rep., May 1989.

[15] Sato, T., Chacon, F., White, L., Raman, V., and Gamba, M., "Mixing and detonation structure in a rotating detonation engine with an axial air inlet," *Combustion Institute*, Vol. 38, No. 3, 2021, pp. 3769–3776.

[16] Lin, W., Zhou, J., Liu, S., Lin, Z., and Zhuang, F., "Experimental study on propagation mode of H_2 /Air continuously rotating detonation wave," *International Journal of Hydrogen Energy*, Vol. 40, No. 4, Jan. 2015, pp. 1980–1993.

[17] Fievisohn, R. T. and Yu, K. H., "Steady-State Analysis of Rotating Detonation Engine Flowfields with the Method of Characteristics," *Journal of Propulsion and Power*, Vol. 33, No. 1, Jan. 2017, pp. 89–99.

[18] Sommers, W. P. and Morrison, R. B., "Simulation of Condensed-Explosive Detonation Phenomena with Gases," *Physics of Fluids*, Vol. 5, No. 2, 1962, pp. 241.

[19] Sichel, M. and Foster, J., "The ground impulse generated by a plane fuel-air explosion with side relief," *Acta Astronautica*, Vol. 6, No. 3-4, March 1979, pp. 243–256.

[20] Fievisohn, R. T., Hoke, J., and Holley, A. T., "Equivalent Available Pressure Measurements on a Laboratory RDE," *AIAA Scitech 2020 Forum*, Jan 2020.

[21] Feleo, A., Shepard, J., and Gamba, M., "Prediction of Detonation-Induced Disturbances Propagating Upstream into Inlets of Rotating Detonation Combustors," *AIAA Propulsion and Energy 2021 Forum*, 2021, p. 3687.

[22] Schwer, D. and Kailasanath, K., "Feedback into Mixture Plenums in Rotating Detonation Engines," *50th AIAA Aerospace Sciences Meeting including the New Horizons Forum and Aerospace Exposition*, jan 2012.

[23] Kaemming, T. A. and Paxson, D. E., "Determining the Pressure Gain of Pressure Gain Combustion," *2018 Joint Propulsion Conference*, July 2018.

[24] Chester, W., "CXLV. The quasi-cylindrical shock tube," *The London, Edinburgh, and Dublin Philosophical Magazine and Journal of Science*, Vol. 45, No. 371, Dec. 1954, pp. 1293–1301.

[25] Chisnell, R. F., "The motion of a shock wave in a channel, with applications to cylindrical and spherical shock waves," *Journal of Fluid Mechanics*, Vol. 2, No. 3, May 1957, pp. 286–298.

[26] Whitham, G. B., "On the propagation of shock waves through regions of non-uniform area or flow," *Journal of Fluid Mechanics*, Vol. 4, No. 04, Aug. 1958, pp. 337.

[27] Smith, L., of Scientific Research, U. S. O., and 2, D. N. D. R. C. D., *Photographic Investigation of the Reflection of Plane Shocks in Air: Final Report*, OSRD report, Division 2, National Defense Research Committee of the Office of Scientific Research and Development, 1945.

[28] Milton, B. E., "Mach Reflection Using Ray-Shock Theory," *AIAA Journal*, Vol. 13, No. 11, Nov. 1975, pp. 1531–1533.

[29] Pedersen, C., Karamehmedović, E., Dam, J. S., and Tidemand-Lichtenberg, P., "Enhanced 2D-image upconversion using solid-state lasers," *Optics Express*, Vol. 17, No. 23, Oct. 2009, pp. 20885.

[30] Dam, J. S., Tidemand-Lichtenberg, P., and Pedersen, C., "Room-temperature mid-infrared single-photon spectral imaging," *Nature Photonics*, Vol. 6, No. 11, Sept. 2012, pp. 788–793.

[31] Duvall, J., Chacon, F., Harvey, C., and Gamba, M., "Study of the Effects of Various Injection Geometries on the Operation of a Rotating Detonation Engine," *2018 AIAA Aerospace Sciences Meeting*, American Institute of Aeronautics and Astronautics, jan 2018.

[32] Schadow, K. and Gutmark, E., "Combustion instability related to vortex shedding in dump combustors and their passive control," *Prog. in Energy and Combust. Sci.*, Vol. 18, No. 2, 1992, pp. 117 – 132.

[33] Prakash, S., Raman, V., Lietz, C. F., Hargus, W. A., and Schumaker, S. A., "Numerical simulation of a methane-oxygen rotating detonation rocket engine," *Proceedings of the Combustion Institute*, Vol. 38, No. 3, 2021, pp. 3777–3786.

[34] Batista, A., Ross, M., Lietz, C., and Hargus, W. A., "Descending Modal Transition Study in a Rotating Detonation Rocket Engine," *AIAA Scitech 2021 Forum*, AIAA Paper 2021-0191, 2021.

[35] Naples, A., Hoke, J., and Schauer, F., "Rotating Detonation Engine Interaction with an Annular Ejector," AIAA Paper 2014-0287, 2014.

[36] Hoke, J., Bradley, R., and Schauer, F., "Single-Ejector Augmentation of a Multi-Tube Pulsed Detonation Engine," AIAA Paper 2008-115, 2008.

[37] Roy, A., Ferguson, D. H., Sidwell, T., O'Meara, B., Strakey, P., Bedick, C., and Sisler, A., "Experimental study of rotating detonation combustor performance under preheat and back pressure operation," *55th AIAA aerospace sciences meeting*, 2017, pp. 1–16.

[38] Sato, T., Chacon, F., White, L., Raman, V., and Gamba, M., "Mixing and detonation structure in a rotating detonation engine with an axial air inlet," *Proceedings of the Combustion Institute*, 2020.

[39] Sato, T. and Raman, V., "Detonation Structure in Ethylene/Air-Based Non-Premixed Rotating Detonation Engine," *Journal of Propulsion and Power*, Vol. 36, No. 5, 2020, pp. 752–762.

[40] Rankin, B. A., Richardson, D. R., Caswell, A. W., Naples, A. G., Hoke, J. L., and Schauer, F. R., "Chemiluminescence imaging of an optically accessible non-premixed rotating detonation engine," *Combust. and Flame*, Vol. 176, 2017, pp. 12 – 22.

[41] Cocks, P. A., Holley, A. T., and Rankin, B. A., "High Fidelity Simulations of a Non-Premixed Rotating Detonation Engine," AIAA Paper 2016-0125, 2016.

[42] Cho, K. Y., Codoni, J. R., Rankin, B. A., Hoke, J., and Schauer, F., *High-Repetition-Rate Chemiluminescence Imaging of a Rotating Detonation Engine*.

[43] Rankin, B. A., Richardson, D. R., Caswell, A. W., Naples, A. G., Hoke, J. L., and Schauer, F. R., "Chemiluminescence Imaging of an Optically Accessible Non-premixed Rotating Detonation Engine," *Combustion and Flame*, Vol. 176, 2017, pp. 12–22.

[44] Wilhite, J., Driscoll, R. B., St. George, A. C., Anand, V., and Gutmark, E. J., "Investigation of a Rotating Detonation Engine Using Ethylene-air Mixtures," Investigation of a rotating detonation engine using ethylene-air mixtures, AIAA Paper 2016-1650, 2016, AIAA Paper 2016-1650, January 2016.

[45] Stechmann, D. P., Heister, S. D., and Harroun, A. J., "Rotating detonation engine performance model for rocket applications," *Journal of Spacecraft and Rockets*, Vol. 56, No. 3, 2018, pp. 887–898.

[46] Chacon, F. and Gamba, M., "Study of Parasitic Combustion in an Optically Accessible Continuous Wave Rotating Detonation Engine," Study of parasitic combustion in an optically accessible continuous wave rotating detonation engine, AIAA Paper, 2019-0473, 2019, 2019.

[47] Burr, J. R. and Yu, K., "Characterization of CH4-O2 Detonation in Unwrapped RDE Channel Combustor," Characterization of CH4-O2 detonation in unwrapped RDE channel combustor, AIAA Paper 2019-4215, 2019, AIAA Paper 2019-4215, Aug. 2019.

[48] Paxson, D. E., "Examination of wave speed in rotating detonation engines using simplified computational fluid dynamics," Examination of wave speed in rotating detonation engines using simplified computational fluid dynamics, AIAA Paper 2018-1883, 2018, AIAA Paper 2018-1883, 2018.

[49] Sato, T., Voelkel, S., and Raman, V., "Detailed Chemical Kinetics Based Simulation of Detonation-Containing Flows," Detailed chemical kinetics based simulation of detonation-containing flows, ASME Paper GT2018-75878, 2018, Paper GT2018-75878, June 2018.

[50] Chacon, F. and Gamba, M., "OH PLIF Visualization of an optically accessible rotating detonation combustor," OH PLIF visualization of an optically accessible rotating detonation combustor, AIAA Paper, 2019-4217, 2019, AIAA Paper, 2019-4217, 2019.

[51] Prakash, S., Raman, V., Lietz, C., Hargus, Jr., W., and Schumaker, S., "Numerical Simulation of a methane-oxygen rotating detonation rocket engine," Numerical Simulation of a methane-oxygen rotating detonation rocket engine, Submitted to Proc. Combust. Int., 2020.

[52] Cocks, P. A., Holley, A. T., and Rankin, B. A., "High Fidelity Simulations of a Non-premixed Rotating Detonation Engine," High Fidelity Simulations of a Non-premixed Rotating Detonation Engine, AIAA Paper 2016-0125, 2016, AIAA Paper 2016-0125, January 2016.

[53] Prakash, S., Fiévet, R., Raman, V., Burr, J., and Yu, K. H., "Analysis of the Detonation Wave Structure in a Linearized Rotating Detonation Engine," *AIAA J.*, 2019, pp. 1–15.

[54] Ishii, K. and Kojima, M., "Behavior of detonation propagation in mixtures with concentration gradients," *Shock Waves*, Vol. 17, No. 1, August 2007, pp. 95–102.

[55] Kessler, D., N Gamezo, V., and Oran, E., "Gas-phase detonation propagation in mixture composition gradients," *Philosophical transactions of the Royal Society. Series A, Mathematical, Physical, and Engineering Sciences*, Vol. 370, 02 2012, pp. 567–96.

[56] Santavicca, D., Yetter, R., and Peluso, S., "Effect of Mixture Concentration Inhomogeneity on Detonation Properties in Pressure Gain Combustors, University Turbine Systems Research (UTSR) 2015 Kick-off Meeting (Presentation)," University Turbine Systems Research (UTSR) 2015 Kick-off Meeting (Presentation).

[57] Boeck, L. R., Berger, F. M., Hasslberger, J., and Sattelmayer, T., "Detonation propagation in hydrogen–air mixtures with transverse concentration gradients," *Shock Waves*, Vol. 26, No. 2, Mar 2016, pp. 181–192.

[58] Mi, X., Higgins, A. J., Ng, H. D., Kiyanda, C. B., and Nikiforakis, N., "Propagation of gaseous detonation waves in a spatially inhomogeneous reactive medium," *Phys. Rev. Fluids*, Vol. 2, May 2017, pp. 053201.

[59] Mi, X., Timofeev, E. V., and Higgins, A. J., "Effect of spatial discretization of energy on detonation wave propagation," *Journal of Fluid Mechanics*, Vol. 817, 2017, pp. 306–338.

[60] Prakash, S., Fiévet, R., and Raman, V., "The Effect of Fuel Stratification on the Detonation Wave Structure," The effect of fuel stratification on the detonation wave structure, AIAA Paper 2019-1511, 2019, AIAA Paper 2019-1511, January 2019.

[61] Eswaran, V. and Pope, S. B., "Direct numerical simulations of the turbulent mixing of a passive scalar," *The Physics of Fluids*, Vol. 31, No. 3, 1988, pp. 506–520.

[62] Hassanaly, M., Raman, V., Koo, H., and Colket, M. B., *Influence of Fuel Stratification on Turbulent Flame Propagation*, AIAA Paper 2015-0426, 2015, Jan 2015.

[63] Boulal, S., Vidal, P., and Zitoun, R., "Experimental investigation of detonation quenching in non-uniform compositions," *Combustion and Flame*, Vol. 172, 2016, pp. 222 – 233.

[64] Koo, H. and Raman, V., "Large-Eddy Simulation of a Supersonic Inlet-Isolator," *AIAA Journal*, Vol. 50, No. 7, 2012, pp. 1596 – 1613.

[65] Fiévet, R. and Raman, V., "Effect of vibrational nonequilibrium on isolator shock structure," *J. of Prop. and Power*, Vol. 34, No. 5, 2018, pp. 1334–1344.

[66] Donde, P., Koo, H., and Raman, V., "A multivariate quadrature based moment method for LES based modeling of supersonic combustion," *Journal of Computational Physics*, Vol. 231, No. 17, 2012, pp. 5805 – 5821.

[67] Koo, H., Raman, V., and Varghese, P. L., "Direct numerical simulation of supersonic combustion with thermal nonequilibrium," *Proceedings of the Combustion Institute*, Vol. 35, No. 2, 2015, pp. 2145 – 2153.

[68] Jiang, G. and Peng, D., "Weighted ENO Schemes for Hamilton–Jacobi Equations," *SIAM Journal on Scientific Computing*, Vol. 21, No. 6, 2000, pp. 2126–2143.

[69] Herrmann, M., Blanquart, G., and Raman, V., "Flux corrected finite-volume scheme for preserving scalar boundedness in large-eddy simulations," Flux corrected finite-volume scheme for preserving scalar boundedness in large-eddy simulations, AIAA Paper 2005-1282, 2005, 2005.

[70] Mueller, M. A., Kim, T. J., Yetter, R. A., and Dryer, F. L., "Flow reactor studies and kinetic modeling of the H2/O2 reaction," *International Journal of Chemical Kinetics*, Vol. 31, No. 2, 1999, pp. 113–125.

[71] Kee, R. J., Rupley, F. M., and Miller, J. A., "Chemkin-II: A Fortran chemical kinetics package for the analysis of gas-phase chemical kinetics," Tech. rep., United States, 1989.

[72] Burr, J. R. and Yu, K., "Detonation Wave Propagation in Cross-Flow of Discretely Spaced Reactant Jets," Detonation wave propagation in cross-flow of discretely spaced reactant jets, AIAA Paper 2017-4908, 2017, AIAA Paper 2017-4908, July 2017.

[73] Raman, V. and Hassanaly, M., "Emerging trends in numerical simulations of combustion systems," *Proceedings of the Combustion Institute*, Vol. 37, No. 2, 2019, pp. 2073–2089.

[74] Khan, A., Sim, H., Vazhkudai, S. S., Butt, A. R., and Kim, Y., "An Analysis of System Balance and Architectural Trends Based on Top500 Supercomputers,"

The International Conference on High Performance Computing in Asia-Pacific Region, 2021, pp. 11–22.

[75] Strohmaier, E., Meuer, H. W., Dongarra, J., and Simon, H. D., "The top500 list and progress in high-performance computing," *Computer*, Vol. 48, No. 11, 2015, pp. 42–49.

[76] Bergman, K., Borkar, S., Campbell, D., Carlson, W., Dally, W., Denneau, M., Franzon, P., Harrod, W., Hill, K., Hiller, J., et al., "Exascale computing study: Technology challenges in achieving exascale systems," *Defense Advanced Research Projects Agency Information Processing Techniques Office (DARPA IPTO), Tech. Rep*, Vol. 15, 2008.

[77] O'Brien, K., Di Tucci, L., Durelli, G., and Blott, M., "Towards exascale computing with heterogeneous architectures," *Design, Automation & Test in Europe Conference & Exhibition (DATE), 2017*, IEEE, 2017, pp. 398–403.

[78] Fatahalian, K. and Houston, M., "A closer look at GPUs," *Communications of the ACM*, Vol. 51, No. 10, 2008, pp. 50–57.

[79] Vestias, M. and Neto, H., "Trends of CPU, GPU and FPGA for high-performance computing," *2014 24th International Conference on Field Programmable Logic and Applications (FPL)*, IEEE, 2014, pp. 1–6.

[80] Kindratenko, V. and Trancoso, P., "Trends in high-performance computing," *Computing in Science & Engineering*, Vol. 13, No. 3, 2011, pp. 92–95.

[81] Kulikov, I., "GPUPEGAS: a new GPU-accelerated hydrodynamic code for numerical simulations of interacting galaxies," *The Astrophysical Journal Supplement Series*, Vol. 214, No. 1, 2014, pp. 12.

[82] Malik, M., Grosheintz, L., Mendonça, J. M., Grimm, S. L., Lavie, B., Kitzmann, D., Tsai, S.-M., Burrows, A., Kreidberg, L., Bedell, M., et al., "HELIOS: an open-source, GPU-accelerated radiative transfer code for self-consistent exoplanetary atmospheres," *The astronomical journal*, Vol. 153, No. 2, 2017, pp. 56.

[83] Le Grand, S., Götz, A. W., and Walker, R. C., "SPFP: Speed without compromise—A mixed precision model for GPU accelerated molecular dynamics simulations," *Computer Physics Communications*, Vol. 184, No. 2, 2013, pp. 374–380.

[84] Zhao, Y., "Lattice Boltzmann based PDE solver on the GPU," *The visual computer*, Vol. 24, No. 5, 2008, pp. 323–333.

[85] Zhu, X., Phillips, E., Spandan, V., Donners, J., Ruetsch, G., Romero, J., Ostilla-Mónico, R., Yang, Y., Lohse, D., Verzicco, R., et al., "AFiD-GPU: a versatile Navier–Stokes solver for wall-bounded turbulent flows on GPU clusters," *Computer physics communications*, Vol. 229, 2018, pp. 199–210.

[86] Bonelli, F., Tuttafesta, M., Colonna, G., Cutrone, L., and Pascazio, G., "An MPI-CUDA approach for hypersonic flows with detailed state-to-state air kinetics using a GPU cluster," *Computer Physics Communications*, Vol. 219, 2017, pp. 178–195.

[87] Pérez, F. E. H., Mukhadiyev, N., Xu, X., Sow, A., Lee, B. J., Sankaran, R., and Im, H. G., "Direct numerical simulations of reacting flows with detailed chemistry using many-core/GPU acceleration," *Computers & Fluids*, Vol. 173, 2018, pp. 73–79.

[88] Bernardini, M., Modesti, D., Salvadore, F., and Pirozzoli, S., "STREAmS: a high-fidelity accelerated solver for direct numerical simulation of compressible turbulent flow," *arXiv preprint arXiv:2004.02276*, 2020.

[89] Elsen, E., LeGresley, P., and Darve, E., "Large calculation of the flow over a hypersonic vehicle using a GPU," *Journal of Computational Physics*, Vol. 227, No. 24, 2008, pp. 10148–10161.

[90] Lai, J., Li, H., Tian, Z., and Zhang, Y., "A multi-GPU parallel algorithm in hypersonic flow computations," *Mathematical Problems in Engineering*, Vol. 2019, 2019.

[91] Rossinelli, D., Hejazialhosseini, B., Spampinato, D. G., and Koumoutsakos, P., "Multicore/multi-gpu accelerated simulations of multiphase compressible flows using wavelet adapted grids," *SIAM Journal on Scientific Computing*, Vol. 33, No. 2, 2011, pp. 512–540.

[92] Xu, J., Fu, H., Luk, W., Gan, L., Shi, W., Xue, W., Yang, C., Jiang, Y., He, C., and Yang, G., "Optimizing finite volume method solvers on NVIDIA GPUS," *IEEE Transactions on Parallel and Distributed Systems*, Vol. 30, No. 12, 2019, pp. 2790–2805.

[93] Candler, G. V., Johnson, H. B., Nompelis, I., Gidzak, V. M., Subbareddy, P. K., and Barnhardt, M., "Development of the US3D code for advanced compressible and reacting flow simulations," *53rd AIAA Aerospace Sciences Meeting*, 2015, p. 1893.

[94] Sato, T. and Raman, V., "Detonation structure in ethylene/air-based non-premixed rotating detonation engine," *Journal of Propulsion and Power*, Vol. 36, No. 5, 2020, pp. 752–762.

[95] Sato, T., Voelkel, S., and Raman, V., "Analysis of detonation structures with hydrocarbon fuels for application towards rotating detonation engines," *2018 Joint Propulsion Conference*, 2018, p. 4965.

[96] Prakash, S., Raman, V., Lietz, C., Hargus, W. A., and Schumaker, S. A., "High Fidelity Simulations of a Methane-Oxygen Rotating Detonation Rocket Engine," *AIAA SciTech 2020 Forum*, 2020, p. 0689.

[97] Prakash, S. and Raman, V., "Wave Structure In Methane/oxygen Rotating Detonation Engine Systems," *Recent progress in detonation for propulsion*, 2019, pp. 22–24.

[98] Barwey, S. and Raman, V., "A Neural Network Inspired Formulation of Chemical Kinetics," *arXiv preprint arXiv:2008.08483*, 2020.

[99] Greenshields, C. J., Weller, H. G., Gasparini, L., and Reese, J. M., "Implementation of semi-discrete, non-staggered central schemes in a colocated, polyhedral, finite volume framework, for high-speed viscous flows," *International journal for numerical methods in fluids*, Vol. 63, No. 1, 2010, pp. 1–21.

[100] Toro, E. F., Spruce, M., and Speares, W., "Restoration of the contact surface in the HLL-Riemann solver," *Shock waves*, Vol. 4, No. 1, 1994, pp. 25–34.

[101] Einfeldt, B., "On Godunov-type methods for gas dynamics," *SIAM Journal on Numerical Analysis*, Vol. 25, No. 2, 1988, pp. 294–318.

[102] Weller, H. G., Tabor, G., Jasak, H., and Fureby, C., "A tensorial approach to computational continuum mechanics using object-oriented techniques," *Computers in Physics*, Vol. 12, No. 6, 1998, pp. 620–631.

[103] Jasak, H., "OpenFOAM: open source CFD in research and industry," *International Journal of Naval Architecture and Ocean Engineering*, Vol. 1, No. 2, 2009, pp. 89–94.

[104] Toro, E. F., *Riemann solvers and numerical methods for fluid dynamics: a practical introduction*, Springer Science & Business Media, 2013.

[105] Syrakos, A., Varchanis, S., Dimakopoulos, Y., Goulas, A., and Tsamopoulos, J., "A critical analysis of some popular methods for the discretisation of the gradient operator in finite volume methods," *Physics of Fluids*, Vol. 29, No. 12, 2017, pp. 127103.

[106] Smith, G., Tao, Y., and Wang, H., "Foundational Fuel Chemistry Model Version 1.0 (FFCM-1)," http://nanoenergy.stanford.edu/ffcm1, 2016.

[107] Liu, Q., Baccarella, D., McGann, B., and Lee, T., "Dual-Mode Operation and Transition in Axisymmetric Scramjets," *AIAA Journal*, Vol. 57, No. 11, 2019, pp. 4764–4777.

[108] Schwinn, K., Gejji, R., Kan, B., Sardeshmukh, S., Heister, S., and Slabaugh, C. D., "Self-sustained, high-frequency detonation wave generation in a semi-bounded channel," *Combustion and Flame*, Vol. 193, 2018, pp. 384–396.

[109] Wolański, P., "Application of the continuous rotating detonation to gas turbine," *Applied Mechanics and Materials*, Vol. 782, Trans Tech Publ, 2015, pp. 3–12.

[110] Wolański, P., Kalina, P., Balicki, W., Rowiński, A., Perkowski, W., Kawalec, M., and Łukasik, B., "Development of gasturbine with detonation chamber," *Detonation Control for Propulsion*, Springer, 2018, pp. 23–37.

[111] Bykovskii, F. A., Zhdan, S. A., and Vedernikov, E. F., "Continuous Spin Detonations," *J. of Prop. and Power*, Vol. 22, No. 6, 2006, pp. 1204.

[112] Stechmann, D. P., Heister, S. D., and Sardeshmukh, S. V., "High-pressure Rotating Detonation Engine Testing and Flameholding Analysis with Hydrogen and Natural Gas," AIAA Paper 2017-1931, (2017).

[113] Frolov, S., Dubrovskii, A., and Ivanov, V., "Three-dimensional numerical simulation of the operation of a rotating-detonation chamber with separate supply of fuel and oxidizer," *Russian Journal of Physical Chemistry B*, Vol. 7, No. 1, 2013, pp. 35–43.

[114] Shepherd, J. E. and Kasahara, J., "Analytical Models for the Thrust of a Rotating Detonation Engine," *California Institute of Technology, GALCIT Report FM2017.001*, 2017.

[115] Tsuboi, N., Watanabe, Y., Kojima, T., and Hayashi, A. K., "Numerical estimation of the thrust performance on a rotating detonation engine for a hydrogen–oxygen mixture," *Proceedings of the Combustion Institute*, Vol. 35, No. 2, 2015, pp. 2005–2013.

[116] Schwer, D. and Kailasanath, K., "Fluid Dynamics of Rotating Detonation Engines with Hydrogen and Hydrocarbon Fuels," *Proc. of the Combust. Inst.*, Vol. 34, No. 2, 2013, pp. 1991–1998.

[117] Wolański, P., "Detonative propulsion," *Proc. Combust. Inst.*, Vol. 34, No. 1, 2013, pp. 125–158.

[118] Xie, Q., Wen, H., Li, W., Ji, Z., Wang, B., and Wolanski, P., "Analysis of operating diagram for H2/Air rotating detonation combustors under lean fuel condition," *Energy*, Vol. 151, 2018, pp. 408–419.

[119] Chacon, F. and Gamba, M., "Detonation Wave Dynamics in a Rotating Detonation Engine," Detonation wave dynamics in a rotating detonation engine, AIAA Paper 2019-0198, 2019, AIAA Paper 2019-0198, 2019.

[120] Nakagami, S., Matsuoka, K., Kasahara, J., Matsuo, A., and Funaki, I., "Experimental study of the structure of forward-tilting rotating detonation waves and highly maintained combustion chamber pressure in a disk-shaped combustor," *Proc. Combust. Inst*, Vol. 36, No. 2, 2017, pp. 2673–2680.

[121] Prakash, S., Fiévet, R., Raman, V., Burr, J., and Yu, K. H., "Analysis of the Detonation Wave Structure in a Linearized Rotating Detonation Engine," *AIAA Journal*, 2019, pp. 1–15.

[122] Bellenoue, M., Boust, B., Vidal, P., Zitoun, R., Gaillard, T., Davidenko, D., Leyko, M., and Le Naour, B., "New combustion concepts to enhance the thermodynamic efficiency of propulsion engines," 2016.

[123] Kindracki, J., Wolański, P., and Gut, Z., "Experimental research on the rotating detonation in gaseous fuels–oxygen mixtures," *Shock waves*, Vol. 21, No. 2, 2011, pp. 75–84.

[124] Wolański, P., "Rotating detonation wave stability," 23rd 23rd International Colloquium on the Dynamics of Explosions and Reactive Systems, (2011).

[125] Anand, V. and Gutmark, E., "Rotating detonation combustors and their similarities to rocket instabilities," *Prog. Energy and Combust. Science*, Vol. 73, 2019, pp. 182–234.

[126] Hayashi, A. K., Kimura, Y., Yamada, T., Yamada, E., Kindracki, J., Dzieminska, E., Wolanski, P., Tsuboi, N., Tangirala, V., and Fujiwara, T., "Sensitivity analysis of rotating detonation engine with a detailed reaction model," AIAA Paper 2009-0633, 2009.

[127] Frolov, S., Aksenov, V., Ivanov, V., and Shamshin, I., "Large-scale hydrogen–air continuous detonation combustor," *International Journal of Hydrogen Energy*, Vol. 40, No. 3, jan 2015, pp. 1616–1623.

[128] Anand, V., George, A. S., Driscoll, R., and Gutmark, E., "Investigation of rotating detonation combustor operation with H2-Air mixtures," *international journal of hydrogen energy*, Vol. 41, No. 2, 2016, pp. 1281–1292.

[129] Cho, K. Y., Codoni, J. R., Rankin, B. A., Hoke, J., and Schauer, F., "High-Repetition-Rate Chemiluminescence Imaging of a Rotating Detonation Engine," AIAA Paper 2016-1648, January 2016.

[130] Zhou, R. and Wang, J.-P., "Numerical investigation of shock wave reflections near the head ends of rotating detonation engines," *Shock Waves*, Vol. 23, No. 5, 2013, pp. 461–472.

[131] Prakash, S., Venkat, R., Christopher, L., William Hargus, J., and Stephen, S., "Numerical Simulation of a Methane-Oxygen Rotating Detonation Rocket Engine," Submitted to Proc. Combust. Int., 2019.

[132] Araki, T., Yoshida, K., Morii, Y., Tsuboi, N., and Hayashi, A. K., "Numerical analyses on ethylene/oxygen detonation with multistep chemical reaction mechanisms: Grid resolution and chemical reaction model," *Combustion Science and Technology*, Vol. 188, No. 3, 2016, pp. 346–369.

[133] Sato, T. and Raman, V., "Hydrocarbon Fuel Effects on Non-premixed Rotating Detonation Engine Performance," AIAA Paper, 2019-2023, (2019).

[134] Sato, T., Fabian, C., James, D., Mirko, G., and Venkat, R., "Dynamics of rotating detonation engines with a pintle-type injector," Dynamics of rotating detonation engines with a pintle-type injector, 24th ISABE Conference, 2019, 2019.

[135] "The Open Source CFD Toolbox http://openfoam.org," 2016.

[136] Goodwin, D. G., Moffat, H. K., and Speth, R. L., "Cantera: An Object-oriented Software Toolkit for Chemical Kinetics, Thermodynamics, and Transport Processes," https://www.cantera.org, 2017. Version 2.3.0.

[137] Mueller, M., Kim, T., Yetter, R., and Dryer, F., "Flow reactor studies and kinetic modeling of the H2/O2 reaction," *International Journal of Chemical Kinetics*, Vol. 31, No. 2, 1999, pp. 113–125.

[138] Toro, E. F., Spruce, M., and Speares, W., "Restoration of the contact surface in the HLL-Riemann solver," *Shock Waves*, Vol. 4, No. 1, 1994, pp. 25–34.

[139] Greenshields, C. J., Weller, H. G., Gasparini, L., and Reese, J. M., "Implementation of Semi-discrete, Non-staggered Central Schemes in a Colocated, Polyhedral, Finite Volume Framework, for High-speed Viscous Flows," *Int. J. Num. Meth. in Fluids*, Vol. 63, No. 1, 2010, pp. 1–21.

[140] Masselot, D., Sato, T., Stephen, V., and Raman, V., "Development of Robust Computational Tools for Rotating Detonation Engines," Mediterranean Combustion Symposium, Sep. 2017.

[141] Sato, T. and Raman, V., "Effects of Injection Pressure on Performance of Non-premixed Rotating Detonation Engines," Submitted to Combustion and Flame., 2020.

[142] Schwer, D. and Kailasanath, K., "Numerical investigation of the physics of rotating-detonation-engines," *Proceedings of the Combustion Institute*, Vol. 33, No. 2, 2011, pp. 2195–2202.

[143] Zhou, R. and Wang, J.-P., "Numerical investigation of flow particle paths and thermodynamic performance of continuously rotating detonation engines," *Combustion and Flame*, Vol. 159, No. 12, 2012, pp. 3632–3645.

[144] Lietz, C., Desai, Y., Hargus, W. A., and Sankaran, V., "Parametric investigation of rotating detonation rocket engines using large eddy simulations," AIAA Paper, 2019-4129, (2019).

[145] Burr, J. and Yu, K., "Detonation Wave Propagation in an Open Channel with Transverse Jets," *53rd AIAA/SAE/ASEE Joint Propulsion Conference*, 2017, p. 4908.